

Alma Mater Studiorum – Università di Bologna

Dottorato di Ricerca in Ingegneria Energetica, Nucleare e del Controllo
Ambientale
Ciclo XXVIII

Settore concorsuale di afferenza: 09/C2

Settore scientifico disciplinare: ING-IND/11

**Theoretical and experimental investigation into stop-band
properties of sonic crystals**

Presentata da: **Federica Morandi**

COORDINATORE DEL DOTTORATO:

Chiar.mo Prof. Vincenzo Parenti Castelli

RELATORE:

Chiar.mo Prof. Massimo Garai

Esame finale anno 2016

“los árboles no nos dejan ver el bosque”
J. Ortega y Gasset

Abstract

The present work explores the theoretical basis of sound propagation through periodic media and provides experimental evidences of stop-band properties of *sonic crystals*, periodic arrays of scatterers immersed in air. In order to investigate the sound field generated by sonic crystals, three theoretical models are used. The band structures are analysed with the Plane Wave Expansion method, while the Multiple Scattering Theory is used to calculate the magnitude of the scattered sound field. The Finite Element analysis is used for both purposes and to provide a stronger bond between the calculations of the theoretical models and the experimental results. Experimental measurement campaigns are performed at the Open University, Milton Keynes (UK) and at the University of Bologna. The two laboratories offer different testing facilities, respectively an anechoic chamber and a large industrial hall. Three square unit cells are analysed, varying the lattice constant and/or the filling fraction in order to provide a correlation between the two experimental setups. Measurements are performed to assess the characteristics of the sound field transmitted and reflected from the arrays, posing a special attention to the contribution of side and top edge diffraction. The evanescent behaviour of modes inside the lattice has been investigated by carrying out Impulse Response measurements inside the crystal and testing, with an intensity probe, the components of the sound field that exit the crystal in the two main directions. Finally, standardised indices are calculated that allow to compare the screening performance of sonic crystals to those of common noise barriers. All measurements setups report coherent results among them and with respect to the theoretical calculations, representing a solid platform for further developments.

Sommario

Il presente lavoro esplora le basi teoriche della propagazione sonora all'interno di mezzi periodici e presenta prove sperimentali delle proprietà di isolamento selettivo in frequenza dei *crystalli sonici*, reticoli di elementi immersi in aria. Per studiare il campo sonoro generato dai cristalli sonici sono usati tre modelli teorici. Le strutture a banda dei reticoli sono analizzate con il metodo Plane Wave Expansion, mentre la Multiple Scattering Theory è utilizzata per valutare l'attenuazione generata puntualmente. L'analisi agli Elementi Finiti ha asservito entrambi gli scopi, permettendo di rafforzare il confronto fra i diversi modelli teorici e la rispondenza fra gli stessi modelli teorici e le misure sperimentali. Le campagne di misure sperimentali sono state condotte presso la Open University, Milton Keynes (UK) e l'Università di Bologna. I due laboratori forniscono strutture di prova profondamente differenti, rispettivamente una camera anecoica ed un grande edificio industriale. Sono state studiate tre celle unitarie, variando la costante di reticolo e/o il rapporto pieni/vuoi, al fine di permettere una correlazione fra le condizioni di prova. Le misure hanno permesso di definire le caratteristiche del campo sonoro trasmesso e riflesso dal reticolo, ponendo una particolare attenzione all'analisi del contributo della diffrazione superiore e laterale. Il comportamento evanescente dei modi dentro ai cristalli sonici è valutato attraverso l'analisi di misure di risposta all'impulso effettuate all'interno del reticolo ed attraverso misure intensimetriche che hanno identificato le componenti del campo sonoro in uscita dal reticolo. Infine sono stati calcolati indici standardizzati di isolamento e riflessione che permettono di confrontare le prestazioni acustiche dei cristalli sonici con quelle delle comuni barriere al rumore. Tutte le configurazioni e le tipologie di misura riportano risultati coerenti fra di loro e consistenti rispetto ai calcoli dei modelli teorici, rappresentando una solida base per ulteriori sviluppi della ricerca.

Acknowledgements

Some say that the aim of a travel is the travel itself and not the final end. At the conclusion of my PhD I therefore wish to thank all the people who made this work possible; but most of all, I wish to thank all the travellers that accompanied me in this extraordinary experience. First of all, I would like to thank my supervisor, Prof. M. Garai, for the patient guidance through the approach of a new topic and for the fruitful discussions that encouraged the search for a deepest insight of acoustics. I am extremely grateful to Prof. S. Taherzadeh and Prof. K. Attenborough who hosted me at the Open University and shared generously their knowledge and passion. I wish to thank all the people of the Applied Acoustic Group in Bologna for their support to this work and for their enthusiastic approach to the research, that stimulated my human and professional growth. In particular my thoughts go to my friend and colleague Eng. S. De Cesaris, who has always been a reference for discussing the outcomes of my research. My acknowledgements are extended to Eng. A. Marzani and Eng. M. Miniaci, with whom we moved the first steps of the experimental campaigns. And I finally wish to express my deepest gratitude to my family, to whom this thesis is dedicated.

Contents

Introduction	21
1 An introduction to sonic crystals	25
1.1 From the origins to the state of art	25
1.2 Fundamentals of periodic systems	27
1.2.1 Direct lattice and reciprocal lattice	27
1.2.2 Bragg scattering and Laue diffraction	31
1.2.3 The Bloch-Floquet theorem	33
1.2.4 Energy bands formation	35
1.2.5 Band gaps in sonic crystals	36
2 Theoretical models	41
2.1 Plane Wave Expansion method	42
2.1.1 The PWE method for two-dimensional periodicity	42
2.1.2 Band structures of sonic crystals	43
2.2 Multiple Scattering Theory	46
2.2.1 The self-consistent method	46
2.2.2 Incidence of a plane wave	47
2.2.3 Incidence of a cylindrical wave	49
2.2.4 Implementation of a MST-based algorithm	50
2.3 The Finite Element Method	53
2.3.1 The acoustic formulation	54
2.3.2 Extraction of dispersion curves using the FE analysis	56
2.3.3 FE modelling of sonic crystals	58
2.4 A comparison between the methods	61
3 Experimental results	63
3.1 The measurement facilities	63
3.1.1 The anechoic chamber at the Open University (UK)	63
3.1.2 The Acoustic Laboratory of the University of Bologna	69
3.2 Sound transmission and sound insulation measurements	71
3.2.1 Array I	73
3.2.2 Array II	75

3.2.3	Array III	77
3.2.4	Measurements vs FE and MST calculations	81
3.3	The sound field inside sonic crystals	81
3.3.1	Interpolation maps of the sound field	81
3.3.2	The evanescent modes	89
3.4	Sound intensity measurements	91
3.5	Standardised SI and RI measurements	95
3.5.1	Sound Insulation Index	97
3.5.2	Comparison with other noise barriers	99
3.5.3	Sound Reflection Index	100
4	Concluding remarks	103
	References	107
A	Publications	113
A.1	Journal papers	113
A.2	International Conference papers	113
A.3	National Conference papers	114

List of Tables

1.1	Wavelengths of the standing waves inside the sonic crystal reported as multiples or submultiples of the lattice constant a	39
2.1	Central frequencies of Bragg band gaps.	45
2.2	Properties of the materials used in the FE analyses.	57
3.1	Temperature and relative humidity measured inside the anechoic chamber at the Open University.	64
3.2	Temperature and relative humidity measured inside the Acoustic Laboratory at the University of Bologna.	70
3.3	Specifications of the three arrays investigated.	72
3.4	Exponential functions fitting the <i>rms</i> pressure values measured inside two sonic crystals in the transverse and longitudinal directions.	90

List of Figures

1.1	The five 2D Bravais lattices.	29
1.2	Construction steps of the 1 st Brillouin zone for a square lattice.	30
1.3	Bragg scattering.	31
1.4	Reduced zone scheme in a one-dimensional reciprocal lattice.	34
1.5	Energy vs wave vector for a free electron and for an electron in a mono-dimensional linear lattice of lattice constant a	35
1.6	Periodic potential and probability density for the standing waves ψ^+ and ψ^-	36
1.7	Extended and reduced zone schemes.	37
1.8	Dispersion curves extracted using the PWE method for three different arrays.	38
2.1	Dispersion curves extracted using the PWE method: variation of the lattice constant.	44
2.2	Dispersion curves extracted using the PWE method: variation of the filling fraction.	44
2.3	Dispersion curves extracted using the PWE method: variation of the density contrast.	45
2.4	Cartesian and polar coordinates of the cylinders in the (x,y) plane.	48
2.5	Convergence of the relative error.	51
2.6	Absolute values of the relative errors between MST predictions computed with two successive truncation orders.	52
2.7	The unit cells together with the boundary conditions.	57
2.8	Band structures for air-PVC bar unit cell and air-PVC hollow cylinder unit cell.	58
2.9	Computational domains and boundary conditions used for the FE modelling.	59
2.10	Sound insulation calculated with the FE method for spherical and plane wave propagation on an array of 15x3 cylinders.	60
2.11	Sound pressure field computed with Comsol Multiphysics [®]	60
2.12	Band structures calculated with the FE method and the PWE method.	61
2.13	Attenuation spectra computed with the MST and the FE method for plane wave propagation.	62

3.1	Panoramic view of the anechoic chamber of the Open University.	65
3.2	The different time windows applied to a IR: rectangular, asymmetric Blackman-Harris and modified Adrienne window.	66
3.3	Influence of the floor grille on the calculation of the Insertion Loss.	67
3.4	Comparison between time windows of different lengths and shapes.	68
3.5	IL measured behind the sonic crystal using a 6 ms and a 3 ms right-side Blackman-Harris window.	68
3.6	Measurement setup at the Acoustic Laboratory of the University of Bologna.	69
3.7	Time window used to cancel the ground reflection at the University of Bologna.	71
3.8	Insulation and reflection measurement positions.	72
3.9	Dispersion curves for a square array with $L_c = 0.135$ m and $r = 0.0275$ m evaluated using the PWE method.	73
3.10	Array I. Insertion Loss at positions 1, 2, 3 and A, B, C for insulation and reflection measurements.	74
3.11	Dispersion curves for a square array with $L_c = 0.069$ m and $r = 0.0275$ m evaluated using the PWE method.	75
3.12	Array II. Insertion Loss at positions 1, 2, 3 and A, B, C for insulation and reflection measurements.	76
3.13	Dispersion curves for a square array with $L_c = 0.200$ m and $r = 0.080$ m evaluated using the PWE method.	77
3.14	Insertion Loss at positions A, B, C for insulation and reflection measurements.	78
3.15	Sound insulation measured for array III with an increasing number of rows of cylinders.	79
3.16	Sound reflection measured for array III with an increasing number of rows of cylinders.	80
3.17	IL measurements vs FE and MST calculations.	82
3.18	Measurement points inside the sonic crystal along the transverse and longitudinal directions.	83
3.19	Array I. Insertion Loss inside the sonic crystal: measurements in the transverse and longitudinal directions.	84
3.20	Array I. Insertion Loss inside the sonic crystal: MST predictions in the transverse and longitudinal directions.	85
3.21	Array I. Insertion Loss measured inside the sonic crystal in the transverse and longitudinal directions.	86
3.22	Array II. Insertion Loss measured inside the sonic crystal in the transverse and longitudinal directions.	87
3.23	Array III. Insertion Loss measured inside the sonic crystal in the transverse and longitudinal directions.	88
3.24	Exponential fitting over the <i>rms</i> pressure values measured inside the arrays II and III in the transverse and longitudinal directions.	90

3.25	Measurement positions for sound intensity measurements at the University of Bologna. Side and back of the sample.	91
3.26	Pictures of the sound intensity measurement setup - side and back.	92
3.27	Sound intensity and sound pressure levels measured on one side of the sample.	93
3.28	Sound intensity and sound pressure levels measured behind the sample.	94
3.29	Measurement setup at the Acoustic Laboratory of the University of Bologna.	96
3.30	Sound Insulation index measured in settings <i>a</i> and <i>b</i>	98
3.31	Insertion Loss measured at different heights from the barrier.	99
3.32	Comparison between the Sound Insulation index measured for a 4-rows sonic crystal and standard noise barriers.	100
3.33	Reflection index measured in settings <i>a</i> and <i>b</i>	101

List of abbreviations

BC Boundary Condition

BG Band Gap

ESS Exponential Sine Swept

FE Finite Element

ff Filling Fraction

IL Insertion Loss

IR Impulse Response

Lc Lattice Constant

MLS Maximum Length Sequence

MST Multiple Scattering Theory

PML Perfectly Matched Layers

PWE Plane Wave Expansion

RI Sound Reflection Index

SC Sonic Crystal

SI Sound Insulation Index

Introduction

Wave propagation through periodic media is a research field that, starting from the solid state physics, drew the attention of the research in many areas; only in the last fifteen years also acoustics belongs to these sectors. The modern approach to sound propagation through periodic media derives from the merge of three fields, namely the study of band structures, the development of metamaterials and multiple scattering formulations. In order to point out the contact point between these three fields, a brief introduction to the development of each field is presented.

Band structures were firstly studied for electronic waves in solids¹. From the late 80's it became clear that also classical waves supported the phenomenon of band structures and pioneering works investigated the propagation of electromagnetic waves in media with periodically-modulated refractive indices², opening the research field of *photonic crystals*³. In the last 20 years, an increase in attention on elastic band gap materials produced a wide literature on the so-called *phononic crystals*, i.e. inhomogeneous elastic media composed of n-dimensional periodic arrays of inclusions embedded in a matrix⁴. Band structures analysis for elastic media have been investigated theoretically and numerically and in particular many works have been devoted to the extraction of acoustic band structures using methods spanning from the multiple scattering formulations to the plane wave expansion methods⁵⁻⁷.

The first theoretical reference to metamaterials dates back to 1968, when Veselago⁸ investigated theoretically the properties of materials where the real part of the electric permittivity and magnetic permeability are simultaneously negative, resulting thus in a negative refractive index. He anyway could not demonstrate experimentally the consequences he predicted as he could not get any material to assume a negative permeability. More than 30 years after, composite media displaying simultaneously negative permeability and permittivity brought the first experimental evidence of Veselago's intuitions^{9;10}. In recent years these materials are referred to as *metamaterials* or *left-handed* materials and many works investigated metamaterials for acoustic applications, the milestone being the work by Liu *et al*¹¹. The strong periodic modulation of density and/or sound velocity forbids wave propagation at certain frequencies in the long-wavelength limit, i.e., in the spectral regions corresponding to wavelengths much larger than the size of the inhomogeneities. Below the homogenisation limit, the medium can be considered as homogeneous and theories related to composite medium hold, i.e. properties such as density and bulk

modulus are correlated to the emerging properties of the composite material. This is the reason why negative densities and bulk modulus occur, which would not be conceivable for non-composite materials. One of the most interesting properties of such metamaterials is that they proved to be effective at low frequency as they break the mass density law and provide significant acoustic attenuation even in reduced thicknesses. The literature produced significant experimental proofs related to acoustic metamaterials displaying negative density, negative bulk modulus, or a combination of the two^{12–18}. The study of engineered composite materials also gave rise to a research field related to cloaking. The original idea is that since Maxwell equations are invariant for a coordinate change, it is possible to use singular transformations to achieve cloaking of the electromagnetic waves^{19;20}. In recent years Milton²¹ transposed this concept to the equations of motion for a general elastic medium but found out that, in general, they are not invariant to coordinate transformation. Cummer *et al.*²² showed that in two dimensions, where the equivalence between electromagnetics and elastodynamics holds, the coordinate transformation holds also for anisotropic media, opening a way to acoustic cloaking²³.

The third contribution comes from multiple scattering formulations and is closely related to *sonic crystals*, i.e. arrangement of solid inclusions in air which provide attenuation for wavelengths related to the lattice constant of the medium. When a wave impinges on a periodic structure, it will be scattered by each scatterer. The scattered wave will be in turn scattered by other scatterers. This process, called *multiple scattering*, leads to the formation of band structures: waves propagate according to certain dispersion relations in some frequency ranges and are inhibited in other frequency regions²⁴. The conditions that prelude to the formation of band gaps concern mainly the density and velocity contrast of the components of the composite, the filling fraction of one of the two components, the lattice structure and the topology. Within this definition of sonic crystal, a major interest has been focused on the study of the scattered field generated by cylinders. The first formulation of multiple scattering specifically tailored for cylinders arranged in air dates back to 1950, with the publication of the milestone work by Twersky²⁵ and has been followed by a huge amount of literature which will be described in the following.

This work locates at the crossroad among these three topics. It presents a theoretical, numerical and experimental investigation on sound propagation through *sonic crystals*, i.e. periodic arrangements of cylinders immersed in air. The phenomenon investigated thus deals with stop-band properties which occurs for waves impinging on a sonic crystal with a wavelength comparable to the lattice constant. The potential applications for these periodic arrangements are many and exploit the peculiarities of the phenomenon. The selectivity in frequency is often used to prevent the spread of highly tonal components, typical for instance of the machineries in industrial plants. The addition of resonators, of sound absorbing material or of lattice defects allows to extend the band gap in frequency and elect sonic crystals to candidates for the construction of urban barriers. Among the advantages, it is worth recalling the limited weight of the structures, which allows to reduce the foundation costs; the free air flow, which also reduces the loads acting on

the foundations by reducing the tilting moment; the continuity of the visibility and of the lightning; finally and not least, a certain aesthetic appeal. In the development of the work, both the construction of band structures and the implementation of multiple scattering algorithms followed the state of art in the literature, while an extensive measurement campaign provided interesting results related to the sound field inside the sonic crystal, on the pattern of the scattered field and on the use of standardised criteria to qualify sonic crystals, all of the measurements being supported by analytical and numerical predictions.

The research has been developed at the University of Bologna and at the Open University headquarters in Milton Keynes (UK), where I was hosted to carry out measurements on sonic crystals in an anechoic chamber and develop analytical tools to predict the performance of sonic crystals. This collaboration allowed to complement the theoretical basis and to compare measurement procedures and results and has been an essential feature of this research.

The text is organised as follows. Chapter 1 reports a brief review of the literature in order to focus on the state of art of the research in this field and to point out open issues and possible developments. The fundamentals of periodic systems are explained in detail, from the original concepts developed in the field of the solid state physics, to the transposition of the same principles to sonic crystals. Chapter 2 introduces two of the most important theoretical models for the computation of the sound field transmitted through sonic crystals: the Plane Wave Expansion method, which allows to compute the band structures of the periodic arrangements under analysis, the Multiple Scattering Theory, through which the scattered field can be computed point by point, and the Finite Element method, which was used to extract the band structures and to evaluate the magnitude of the sound attenuation through the crystal. Chapter 3 describes in detail the experimental campaign conducted at the Open University, Milton Keynes (UK) and at the University of Bologna. The two test facilities are described in detail and the results of the experimental campaigns are discussed. First, the sound pressure field transmitted and reflected by the sonic crystal is analysed point by point. Then the distribution of the sound pressure field inside the sonic crystal is investigated through a further set of measurements which included sound intensity measurements. The final section of this chapter is dedicated to the analysis of standardised sound insulation and reflection indices, which have been firstly measured in this work in order to test the effectiveness of sonic crystals versus other standard noise barriers. The concluding remarks discuss the main results achieved throughout this work with reference to the existing literature, highlight the innovative contributions that this work brought to the research field and suggests future steps for an evolution of the research on the topic.

Chapter 1

An introduction to sonic crystals

This first chapter is meant to provide an overview on sonic crystals (SCs), spanning from the analysis of the literature to the formulation of the principles of solid state physics from which Bragg scattering was first analysed about 100 years ago. The first section traces the evolution of the research field through a selection of papers which have been considered representative of the whole literature. A great importance is given to works which not only present theoretical formulations but which also provide experimental evidences, as the milestone works for theoretical derivations are exposed in detail in Chapter 2. The second section provides the fundamental tools for an insight into the origin of stop-band phenomena.

1.1 From the origins to the state of art

In the last two decades, many works have been devoted to the investigation of sound waves propagating through sonic crystals. The first experimental evidences of band gaps in sonic crystal dates back to 1995, when Martinez *et al.*²⁶ measured sound attenuation across a sculpture by Eusebio Sempere, exhibited outside the Juan March Foundation in Madrid. The sculpture basically consists of an arrangement of steel cylinders in air mounted on a circular platform. Measurements at different incidence angles provided the first evidences of the formation of acoustic band gaps in periodic elastic media⁵. After this pioneering work, several studies reported measurements and theoretical approaches to characterise sonic crystals. Tests involved the variation of the spatial arrangement of the cylinders and of the filling fraction, showing that simple lightweight sonic crystals are capable to reduce sound transmission up to 25 dB^{27;28;24;29}. Closely related to the sound attenuation provided by sonic crystals are the reflectance properties of such periodic arrangements. Sanchis *et al.*³⁰ investigated the sound pressure field reflected from the sonic crystal by means of multiple scattering formulations which were verified by measurements. They found out that the standing wave ratio is enhanced in the same frequency range in which stop-band phenomena occur. The reflectance properties were further investigated and related to the band structures of the sonic crystal³¹. Though the early theoreti-

cal formulations of multiple scattering phenomena refer to rigid circular cylinders, other kind of scatterers have been analysed in the literature. In particular, square scatterers rotated along the vertical plane have been investigated leading to a modelling of negative refraction³² and to the optimisation of tunable acoustic waveguides³³.

The most limiting property of sonic crystal is that stop-bands are constrained to a narrow band; thus an extensive literature focused on widening the frequency range of attenuation by associating separate attenuation mechanisms to Bragg scattering. The infinite possibilities of combination of these phenomena gave rise to several design optimised to provide a broadband attenuation. For instance, Romero *et al.*³⁴ designed an array of scatterers characterised by multiple resonances of different nature and material with different mechanical properties and geometries which provide attenuation effects in the long wavelength limit. Similarly, Elford *et al.*³⁵ proposed *matryoshka* resonant sonic crystals, i.e. concentric configurations of slotted cylinders that provide sound attenuation below Bragg frequency. Krynkin *et al.* proved that the periodic concentric arrangement of cylinders with slits and inner elastic shells provided attenuation below the first Bragg band gap³⁶. Another solution to render sonic crystals effective broadband is the application of sound absorbing materials to the scatterers. Umnova *et al.*³⁷ provided theoretical and experimental evidences about the benefits achievable by the adding porous materials to the cylinders. Sánchez-Dehesa *et al.*³⁸ tested sonic crystals consisting in cylinders arranged in three layers and filled with rubber crumb. Sound attenuation was tested in an anechoic chamber and compared to the attenuation provided by plain rigid cylinders. García-Chocano *et al.*³⁹ performed measurement on the same two configurations measured in transmission chambers, i.e. in a diffuse field.

The application of sonic crystals as noise barrier was further developed by studying the effect of the ground where the scatterers are fixed and its interfering behaviour with respect to the formation of band gaps. Kryinkin *et al.*⁴⁰ combined the effects of a two-dimensional (semi-infinite) periodic array of cylinders and a impedance ground where cylinders would be installed. The theoretical and experimental analysis showed that, while a rigid ground would mine the positive IL related to Bragg band gap, an impedance ground shifts the ground effect minima to lower frequencies, not interfering with the Bragg band gap. With a specific attention towards sustainable application as noise barriers, works have been devoted to quantify the attenuation produced by trees arranged in a periodic lattice⁴¹ and by bamboo rods⁴², plain and drilled in order to couple resonance phenomena.

The inclusion of defects into sonic crystals has also been investigated, where these anomalies were for instance due to vacancies or modification the dimensions of some scatterers^{43;44}. Evolutionary algorithms have been developed within the multiple scattering theory to allow a controlled manipulation of waves inside the sonic crystal by introducing vacancies in the lattice⁴⁵. The evanescent behaviour of modes in the band gap has been theoretically and experimentally demonstrated in the presence of lattice defects as well⁴⁶.

Some comprehensive works included many of the features exposed above, both in

terms of design of the scatterers and measurement setup. One amongst all, Castineira-Ibàñez *et al.*⁴⁷ characterised acoustic barriers based on fractal geometries to maximise the Bragg scattering and multi-phenomena scatterers with several noise control mechanisms, as resonances or absorption, by acoustic standardisation tests according to EN 1793-2⁴⁸, i.e. under diffuse field conditions.

1.2 Fundamentals of periodic systems

The present section deals with the fundamentals of periodic structures and the properties of wave propagation inside such media. First, from the concepts of direct and reciprocal lattice, Bragg's law and Laue diffraction conditions are derived. Second, the Bloch-Floquet theorem is presented, that emerges as the most significant property of wave propagation in periodic media. The formation of band structures is then analysed together with the analysis of band structures. Finally, the theory of wave propagation in periodic media is applied to the acoustic waves, pointing out the analogies and differences between the two physical systems. The 2D periodicity is analysed in greater detail, the 1st Brillouin zone is derived for the square array and the existence of band gaps is derived also for acoustic waves. The notation used in the following recalls Refs.^{1,49}.

1.2.1 Direct lattice and reciprocal lattice

A direct lattice, or Bravais lattice, \vec{R} is an infinite set of points generated by the translation of a set of vectors \vec{a}_i , called *primitive vectors*, which are linearly independent. Its most important property is that the atomic structure remains invariant under translation through any vector which is the sum of integral multiples of these vectors. The general definition in n dimensions is:

$$\vec{R} = \left\{ \sum_{i=1}^n \nu_i \vec{a}_i \right\} \quad (1.1)$$

where $\nu_i \in Z$ and \vec{a}_i are the primitive vectors lying in different directions. Each point reached by the translations is a *lattice site*. The physical arrangement of the whole crystal can be defined by specifying the contents of a single *unit cell*, whose repetition following the \vec{a}_i vectors generates the crystal structure. The unit cell is said to be *primitive* if it is determined by the primitive vectors. Considering a 3D lattice, \vec{R} can be expressed as a linear combination of three primitive vectors $\{a_1, a_2, a_3\}$ in the direct space that constitute a base:

$$\vec{R} = \nu_1 \vec{a}_1 + \nu_2 \vec{a}_2 + \nu_3 \vec{a}_3 \quad (1.2)$$

where $\nu_i \in Z$.

The reciprocal lattice is defined together with the direct lattice. Consider a direct lattice \vec{R} and a plane wave $e^{i\vec{G}\vec{r}}$ impinging on it; for some G values, this wave has the same periodicity of the direct lattice. The reciprocal lattice of a given direct lattice is defined as the set of vectors \vec{G} that give plane waves with the same periodicity of the

direct lattice. In mathematical terms one has:

$$e^{i\vec{G}(\vec{R}+\vec{r})} = e^{i\vec{G}\vec{r}} \Leftrightarrow e^{i\vec{G}\vec{R}} = 1 \quad (1.3)$$

This implies that

$$\vec{G} \cdot \vec{R} = 2\pi n \quad (1.4)$$

where $n \in \mathbb{Z}$. Given N the number of cells that build the crystal, N is also the number of vectors of the direct lattice \vec{R} and the number of vectors \vec{G} of the reciprocal lattice. The reciprocal lattice is still a Bravais lattice. So, similarly to the direct lattice, vectors \vec{G} can be expressed as a linear combination of three fundamental vectors $\{b_1, b_2, b_3\}$ of the reciprocal space:

$$\vec{G} = \mu_1 \vec{b}_1 + \mu_2 \vec{b}_2 + \mu_3 \vec{b}_3 \quad (1.5)$$

where $\mu_i \in \mathbb{Z}$. The condition in Eq. 1.4 is satisfied if and only if

$$\vec{a}_i \cdot \vec{b}_j = 2\pi \delta_{ij} \quad (1.6)$$

In three dimensions it hence becomes:

$$\begin{aligned} \vec{b}_1 \cdot \vec{a}_1 &= 2\pi, & \vec{b}_2 \cdot \vec{a}_1 &= 0, & \vec{b}_3 \cdot \vec{a}_1 &= 0 \\ \vec{b}_1 \cdot \vec{a}_2 &= 0, & \vec{b}_2 \cdot \vec{a}_2 &= 2\pi, & \vec{b}_3 \cdot \vec{a}_2 &= 0 \\ \vec{b}_1 \cdot \vec{a}_3 &= 0, & \vec{b}_2 \cdot \vec{a}_3 &= 0, & \vec{b}_3 \cdot \vec{a}_3 &= 2\pi. \end{aligned} \quad (1.7)$$

The fundamental vectors of the reciprocal lattice $\{b_1, b_2, b_3\}$ are thus given by:

$$\vec{b}_1 = 2\pi \frac{\vec{a}_2 \times \vec{a}_3}{\vec{a}_1 \cdot \vec{a}_2 \times \vec{a}_3}, \quad \vec{b}_2 = 2\pi \frac{\vec{a}_3 \times \vec{a}_1}{\vec{a}_1 \cdot \vec{a}_2 \times \vec{a}_3}, \quad \vec{b}_3 = 2\pi \frac{\vec{a}_1 \times \vec{a}_2}{\vec{a}_1 \cdot \vec{a}_2 \times \vec{a}_3}. \quad (1.8)$$

A brief but incisive distinction among the two lattices is provided by Kittel¹.

When we rotate a crystal, we rotate both the direct lattice and the reciprocal lattice. Vectors in the crystal lattice have the dimensions of [length]; vectors in the reciprocal lattice have the dimensions of [length]⁻¹. The crystal lattice is a lattice in real and ordinary space; the reciprocal lattice is a lattice in the Fourier space.

The statement that the reciprocal lattice belongs to the Fourier space is justified as follows, considering a mono-dimensional periodic function:

$$f(x+l) = f(x) \quad (1.9)$$

In order to represent functions with the periodicity of a given lattice, it is possible to express this function as a Fourier series,

$$f(x) = \sum_n A_n e^{2\pi i n x / a}$$

where n is an integer. This can also be written in the form

$$f(x) = \sum_n A_n e^{i g x}$$

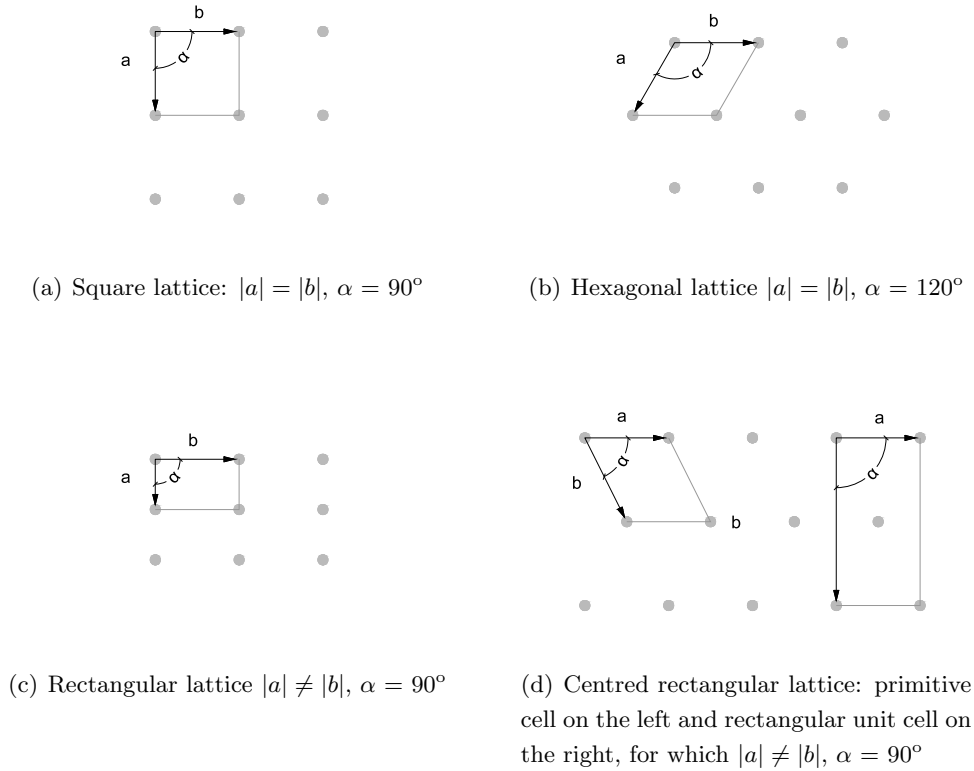


Figure 1.1: The five 2D Bravais lattices: square, hexagonal, rectangular, oblique and centred rectangular.

where g belongs to the set of reciprocal lattice lengths⁴⁹,

$$g_n = n \frac{2\pi}{a} \quad (1.10)$$

The coefficients in the Fourier series are determined by

$$A_g = \frac{1}{a} \int_{cell} f(x) e^{-igx} dx \quad (1.11)$$

where the integration spans only one cell of the lattice. The proof that the Fourier series implies the periodicity of function $f(x)$ is given by the condition that, for any g ,

$$e^{igl} = 1 \quad (1.12)$$

The group theory defines the number of Bravais lattices that it is possible to have in each space dimension. In particular there exist one kind of 1-D lattice, 5 kinds of 2D lattices and 14 kinds of 3D lattices. In particular, there are five direct 2D lattices: oblique, square, hexagonal, primitive rectangular and centred rectangular (see Fig. 1.1).

Since the focus of this work is on two-dimensional square arrays, in the following the characteristic features of this kind of lattices are specified. Using the same notation of

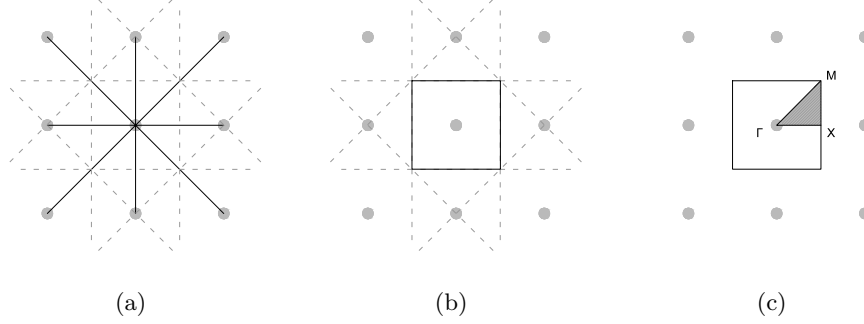


Figure 1.2: Construction steps of the 1st Brillouin zone for a square lattice.

section 1.2, the reciprocal lattice vectors for a square lattice are defined by:

$$\vec{G} \cdot \vec{R} = 2\pi n \quad \Leftrightarrow \quad \vec{a}_i \cdot \vec{b}_j = 2\pi\delta_{ij} \quad (1.13)$$

From (1.13) we have:

$$\vec{a}_1 \cdot \vec{b}_1 = 2\pi \quad \text{and} \quad \vec{a}_1 \cdot \vec{b}_2 = 0 \quad (1.14)$$

This implies

$$\vec{b}_2 \perp \vec{a}_1 \parallel x \Rightarrow \vec{b}_2 \parallel y \quad (1.15)$$

Reiterating the same operations for y, we have:

$$\vec{b}_1 = \frac{2\pi}{a_1} \hat{x} \quad \text{and} \quad \vec{b}_2 = \frac{2\pi}{a_2} \hat{y} \quad (1.16)$$

Thus, the reciprocal lattice of a square lattice with lattice constant a is a square lattice with lattice constant $2\pi/a$. The Brillouin zones are defined as the Wigner-Seitz cells of the reciprocal lattice, i.e. the region of space built around a node of the reciprocal lattice and made of the points which are closer to that point than to any other. Thus it is possible to spot the 1st Brillouin zone by joining the points which are equidistant from adjacent sites of the reciprocal lattice, as shown in Fig. 1.2. Three high symmetry directions are spanned in the band analysis: ΓX , XM and ΓM , where the $\Gamma = [0, 0]$, $X = [\pi/a, 0]$, $M = [\pi/a, \pi/a]$.

The most significant parameters for the description on an array are the lattice constant a and the filling fraction ff . The lattice constant a of a square lattice corresponds to one of the vectors of the base, i.e. the distance between two adjacent lattice sites. The filling fraction ff is defined as the ratio of the area occupied by the scatterers to the total area of the unit cell. For cylindrical scatterers in a square lattice, it is:

$$ff_{cyl,sq} = \frac{\pi r^2}{a^2} \quad (1.17)$$

The maximum filling fraction for a square lattice is achieved when $a = 2r$, i.e. adjacent cylinders have a contact point. This occurs at a $ff_{max} = 0.785$.

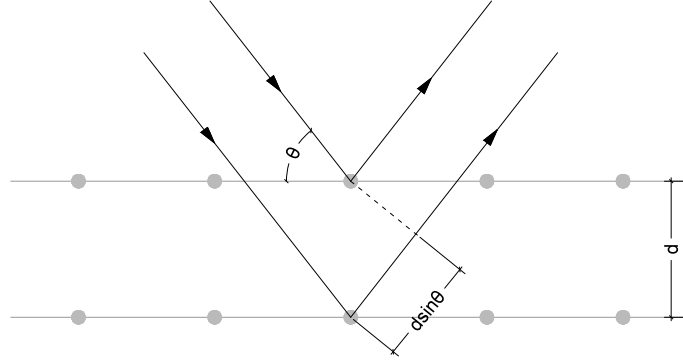


Figure 1.3: Bragg scattering.

1.2.2 Bragg scattering and Laue diffraction

The crystalline structure of solids has been historically investigated through the diffraction of photons, neutrons or electrons. In 1913, W. L. Bragg gave an effective explanation to the observed angles of diffracted beams from a crystal. In particular, he observed that for certain incidence angles and wavelengths, the intensity of the reflected radiation was strengthened. He explained that considering the structure of the crystal as a set of parallel lattice planes spaced apart of a distance d . Whenever the path difference for rays reflected from adjacent planes is an integer number of the incident wavelength λ , the reflections from all parallel planes add up in phase giving a strong reflected beam (see Fig. 1.3). The condition for Bragg scattering is then:

$$2d\sin\theta = n\lambda \quad (1.18)$$

M. T. F. Von Laue determined the amplitude of the scattered wave. The detailed derivation is reported in Kittel¹ and is based on the hypothesis of elastic scattering, i.e. the wavelength of the particle (phonon or neutron) is not changed on reflection. Consider a plane wave incident on a crystal with primitive axes a_1, a_2, a_3 . The origin of the coordinate system O is chosen anywhere inside the crystal. Assuming time-harmonic dependence, the amplitude of the wave in free-field at point \vec{x} is given by:

$$F(\vec{x}) = F_0 e^{i\vec{k}\vec{x}}$$

Assuming that the plane wave propagation is not affected by the presence of the lattice, at some point \vec{R} inside the crystal the amplitude of the incident wave is:

$$F(\vec{R}) = F_0 e^{i\vec{k}\vec{R}}$$

At some point $\vec{\rho} = \vec{R} + \vec{r}$ outside the crystal, the contribution of the atom at \vec{R} to the scattered field involves a phase factor of the incident radiation and a phase factor of the scattered radiation as observed at $\vec{\rho}$. The total phase factor is:

$$e^{i\vec{k}\vec{R}}e^{i\vec{k}'\vec{r}} = e^{i\vec{k}\vec{R}+i\vec{k}'\vec{r}}$$

If $\vec{\rho}$ is larger than the dimension of the crystal, $r \simeq \rho - R\cos(\vec{R}, \vec{\rho})$ and the total phase factor can be expressed as

$$e^{i\vec{k}\vec{R}+i\vec{k}'\vec{\rho}-i\vec{k}\vec{R}\cos(\vec{R}, \vec{\rho})}$$

Considering that the amplitude of the wave scattered at $\vec{\rho}$ is likely to be proportional to the density of atoms $n(\vec{R})$ in the crystal, it is also proportional to the integral

$$\int dV n(\vec{R}) e^{i\vec{k}\vec{R}-i\vec{k}\vec{R}\cos(\vec{R}, \vec{\rho})} \quad (1.19)$$

where $e^{ik\rho}$ is omitted as constant over the volume and the difference between $1/r$ and $1/\rho$ is neglected. The argument of the exponential can be expressed as

$$i\vec{k}\vec{R} - i\vec{k}\vec{R}\cos(\vec{R}, \vec{\rho}) \equiv i\vec{R}(\vec{k} - \vec{k}') = -i\vec{R}\Delta\vec{k}$$

where \vec{k}' is the wave vector in the scattering direction $\vec{\rho}$ and $\Delta\vec{k} = \vec{k}' - \vec{k}$ is the difference between the scattered wave vector and the initial wave vector. Considering the finite nature of the lattice, the integral in Eq. 1.19 reduces to a finite sum over the lattice points \vec{R} (Eq. 1.2). The total scattered radiation amplitude seen at $\vec{\rho}$ is then proportional to

$$A \equiv \sum_{\vec{R}} e^{-i\vec{R}\cdot\Delta\vec{k}}$$

Some algebra¹ leads to the conclusion that the maxima of the diffracted wave occur whenever the following equations, known as Laue equations, are satisfied simultaneously.

$$\vec{a}_1 \cdot \Delta\vec{k} = 2\pi q \quad \vec{a}_2 \cdot \Delta\vec{k} = 2\pi s \quad \vec{a}_3 \cdot \Delta\vec{k} = 2\pi t \quad (1.20)$$

where q, s, t are integers. These equations are proved to be equivalent to Bragg's law¹. The solution is particularly simple if the primitive vectors are mutually orthogonal, for then

$$\Delta\vec{k} = 2\pi \left(\frac{q}{a_1} \hat{a}_1 + \frac{s}{a_2} \hat{a}_2 + \frac{t}{a_3} \hat{a}_3 \right) \quad (1.21)$$

If the axes are not mutually orthogonal, considering the expression

$$\Delta\vec{k} = q\vec{A} + s\vec{B} + t\vec{C}$$

it is possible to verify by direct substitution that Eq. 1.2.2 satisfies the Laue equations if and only if $\Delta\vec{k}$ is equal to any reciprocal lattice vector \vec{G} . The diffraction condition hence becomes

$$\Delta\vec{k} = \vec{G} \quad (1.22)$$

This equation can be further manipulated to return another formulation of the diffraction law. In fact, it is possible to write

$$\vec{k} + \vec{G} = \vec{k}'$$

By squaring this equation, one has $(\vec{k} + \vec{G})^2 = k'^2$, but $k = k'$ in elastic scattering, thus the diffraction law may be written as

$$2\vec{k} \cdot \vec{G} + G^2 = 0 \quad (1.23)$$

It is possible to notice that the above mentioned problem can be accounted to as a single-scattering problem, i.e. the contribution to the scattered field given by each scatterer is computed as if each scatterer was isolated from the others. This approximation holds until the atoms are spaced apart by a considerable distance compared to their diameter, as often is the case in crystal lattices.

1.2.3 The Bloch-Floquet theorem

The Bloch theorem in the Solid State Physics states that⁴⁹

For any wave-function/state function that satisfies the Schrödinger equation (or its classical or quantal equivalent) there exist a vector \vec{k} such that translation by a lattice vector \vec{l} is equivalent to multiplying by the phase factor $e^{i\vec{k}\vec{l}}$.

In mechanics, this theorem is known as Floquet theorem, thus in the following it will be referred to as Bloch-Floquet theorem. That statement can be formulated as follows:

$$\psi_{\vec{k}}(\vec{r} + \vec{l}) = e^{i\vec{k}\vec{l}} \psi_{\vec{k}}(\vec{r}) \quad (1.24)$$

where $\psi_{\vec{k}}$ is a Bloch wave function (or Bloch state) with a given wave vector \vec{k} . In other words, the wave function of a particle placed in a periodic potential, i.e. a Bloch wave, consists of the product of a plane wave and a periodic function which has the same periodicity as the potential. In the free field, the wave equation would satisfy

$$\psi_{\vec{k}}(\vec{r}) = e^{i\vec{k}\vec{r}} \quad (1.25)$$

Then, to use a notation which recalls more directly the free field propagation, Bloch-Floquet theorem can be expressed as:

$$\psi_{\vec{k}}(\vec{r}) = e^{i\vec{k}\vec{r}} u_{\vec{k}}(\vec{r}) \quad (1.26)$$

where u is a periodic function, i.e.

$$u_{\vec{k}}(\vec{r} + \vec{l}) = u_{\vec{k}}(\vec{r}) \quad (1.27)$$

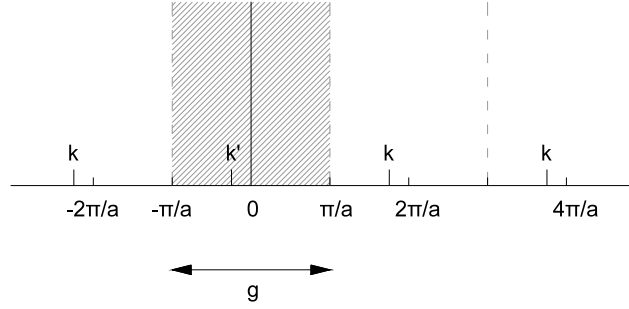


Figure 1.4: Reduced zone scheme in a one-dimensional reciprocal lattice. All the points k are equivalent.

The term $e^{i\vec{k}\vec{l}}$ shows many similarities to the term $e^{i\vec{g}\vec{l}}$ that appeared in subsection 1.2.1, suggesting that both \vec{k} and \vec{g} belong to the reciprocal space. In fact, if a Bloch function has wave vector \vec{g} , since $e^{i\vec{g}\vec{l}} = 1$, it would be a periodic function:

$$\psi_{\vec{g}}(\vec{r} + \vec{l}) = e^{i\vec{g}\vec{l}}\psi_{\vec{g}}(\vec{r}) = \psi_{\vec{g}}(\vec{r}) \quad (1.28)$$

for all \vec{l} .

Consider a Bloch function has wave vector \vec{k} such that

$$\vec{k} = \vec{g} + \vec{k}' \quad (1.29)$$

where \vec{g} is some vector of the reciprocal lattice and \vec{k}' is another vector. Then

$$\psi_{\vec{k}}(\vec{r} + \vec{l}) = e^{i(\vec{g} + \vec{k}')\vec{l}}\psi_{\vec{k}}(\vec{r}) = e^{i\vec{g}\vec{l}}e^{i\vec{k}'\vec{l}}\psi_{\vec{k}}(\vec{r}) = e^{i\vec{k}'\vec{l}}\psi_{\vec{k}}(\vec{r}) \quad (1.30)$$

i.e. the Bloch function $\psi_{\vec{k}}$ satisfies the Bloch-Floquet theorem as if it had the wave vector \vec{k}' . It is to notice that \vec{k} can assume multiple values for a given \vec{k}' because it depends also on the vectors \vec{g} of the reciprocal lattice. Thus it is necessary to define uniquely the wave vector of a given Bloch function. Considering a one-dimensional lattice, a state may be assigned any wave number in the set

$$k = n\frac{2\pi}{a} + k' \quad (1.31)$$

The standard choice is to consider k' as representative for all k values, being $|k'|$ as small as possible. In particular, it has to lie closer to the origin than to any other point of the reciprocal lattice - i.e. in the first Brillouin zone. The wavenumber is then chosen in the range

$$-\frac{\pi}{a} < k \leq \frac{\pi}{a} \quad (1.32)$$

It is clear that any point \vec{k} in the reciprocal space can be reduced to a point in the Brillouin zone and any Bloch wave can be characterised by its reduced wave vector. Since

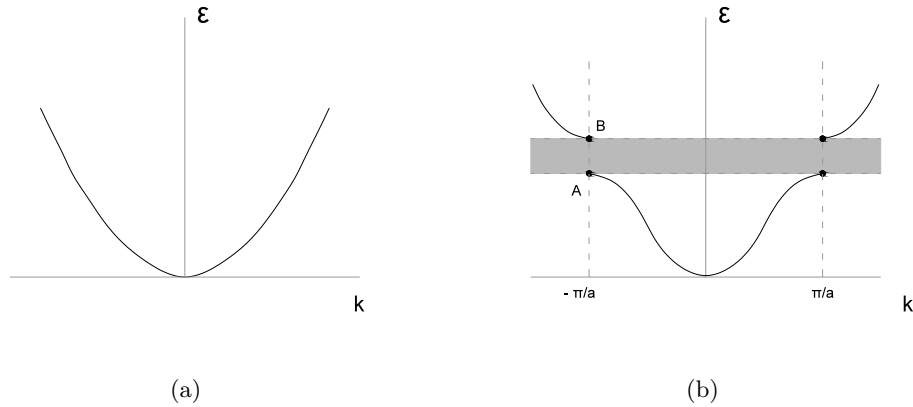


Figure 1.5: Energy vs wave vector for a free electron (a) and for an electron in a mono-dimensional linear lattice of lattice constant a (b).

many states have the same reduced wave vector and different energies, the *reduced zone scheme* allows to represent them all by folding the energy bands inside the 1st Brillouin Zone.

As wave functions are periodic in the direct lattice, the solutions in the Fourier space are periodic in the reciprocal lattice, i.e. as well as the calculations in the direct lattice are constrained to the unit cell, in the reciprocal lattice the calculations are constrained to the 1st Brillouin zone.

1.2.4 Energy bands formation

Electron in crystals are arranged in energy bands, separated by regions in which no energy states are allowed. These regions where propagation is inhibited are called *band gaps*, while the allowed states are generally referred to as *pass bands*. The formation of energy band gaps derives directly from Laue diffraction conditions and are derived in the following with reference to the nearly free electron model, i.e. assuming that the band electrons are perturbed only weakly by the periodic potential of the ion cores.

Fig. 1.5 plots the energy versus the wave vector for a free electron (left) and for an electron in a linear lattice with constant a (right) showing an energy gap. The Bragg condition $(\vec{k} + \vec{G})^2 = k^2$ in one dimension becomes:

$$k = \pm \frac{1}{2}G = \pm \frac{n\pi}{a} \quad (1.33)$$

where $G = \pm 2n\pi/a$ is a vector of the reciprocal lattice and n is an integer.

When Bragg condition is satisfied a wave traveling in one direction is soon Bragg-reflected and then travels in the opposite direction. Each subsequent Bragg reflection reverses the direction of travel again. The only time-independent situation is formed by standing waves¹. From the free-electron model, we have two traveling waves $e^{i\pi x/a}$ and

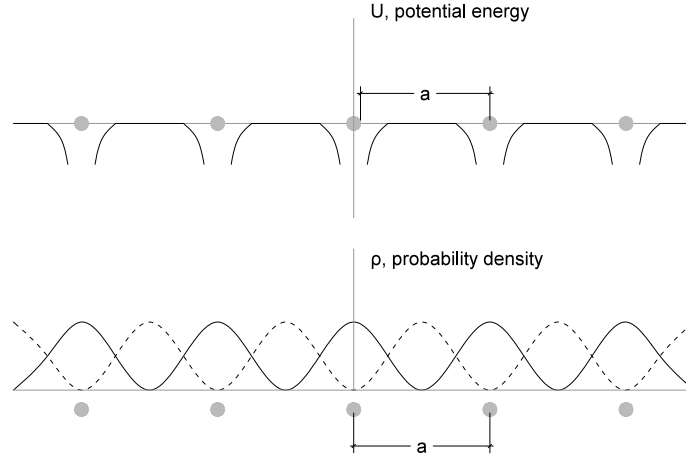


Figure 1.6: Periodic potential and probability density for the standing waves ψ^+ (continuous line) and ψ^- (dashed line).

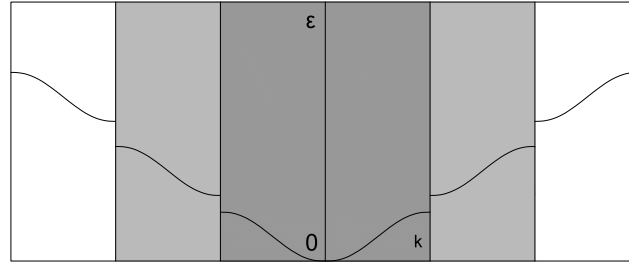
$e^{-i\pi x/a}$ which can in turn form two standing waves:

$$\begin{aligned}\psi^+ &\propto (e^{i\pi x/a} + e^{-i\pi x/a}) = 2\cos(\pi x/a) \\ \psi^- &\propto (e^{i\pi x/a} - e^{-i\pi x/a}) = 2i\sin(\pi x/a)\end{aligned}\tag{1.34}$$

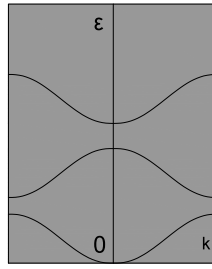
Fig. 1.6 sketches the distribution of probability density $\rho = |\psi^2|$ for the standing waves ψ^+ and ψ^- . While a traveling wave would distribute electrons uniformly in x , the standing wave ψ^+ distributes the electrons preferably on the ion cores, where the potential energy is lower, and ψ^- distributes electrons between the ion cores. Thus the average potential energy of ψ^+ will be lower than that of a traveling wave, whereas the average potential energy of ψ^- will assume higher values. The difference between ψ^- and ψ^+ is the width of the energy gap at $k = \pi/a$, i.e. when the wave vector k lies on the boundary of the 1st Brillouin zone.

1.2.5 Band gaps in sonic crystals

When trying to translate the concept of electron energy bands into acoustics, several hypotheses fall. Considering an array of scatterers immersed in a fluid. First of all, the scatterers are not immersed in a periodic potential. Infinite periodicity is clearly an abstract concept, which can be considered a valid assumption for instance in crystalline structures where the dimension of the crystal is sensitively smaller than the wavelength used to investigate it. Dealing with sonic crystals, the dimensions of the scatterers cannot be neglected anymore.



(a) Extended zone scheme



(b) Reduced zone scheme

Figure 1.7: Extended (a) and reduced (b) zone schemes.

Assuming a harmonic temporal dependence, the wave equation in free field

$$(\nabla^2 + k^2)p = 0 \quad (1.35)$$

has a solution of the type e^{ikx} , where k is the wave vector. In a periodic medium, we will have to solve

$$(\nabla^2 + k^2)p_k = 0 \quad (1.36)$$

with the periodic condition

$$p_k(r + R) = p_k e^{ikR} \quad (1.37)$$

where k represent the wave vector inside the periodic medium and its values lie within the first Brillouin zone. Since in a 2D periodic medium the eigenvalue problem is restricted to a single unit cell, the eigenvalues $\omega(k)$ form a set of discrete frequencies which represent the frequencies supported by the lattice³. Thus, for each value of wavenumber k there is an infinite set of modes with discretely spaced frequencies, which can be labelled by a band index n . Since k enters as a continuous parameter, we expect that the frequency of each band, for each n , varies continuously as k varies. The band structures thus are a set of continuous functions $\omega_n(k)$ indexed in order of increasing frequency by the band number³.

The relation between ω and k is usually referred to as dispersion relation, and in the free field the proportional constant is the speed of sound, $c = \omega/k$. The flattening of the dispersion curves can be thought as of a decrease of the speed of sound inside the crystal.

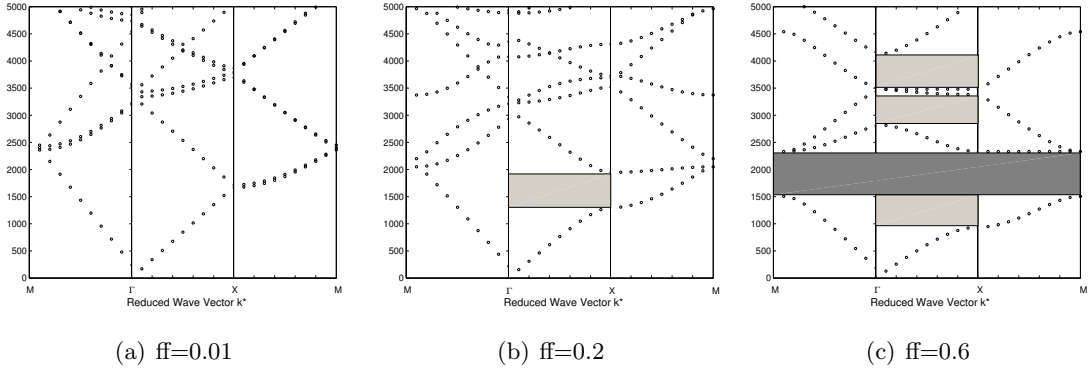


Figure 1.8: Dispersion curves extracted using the PWE method for three different arrays; the lattice constant L_c is 0.1 m and the filling fraction is $ff = 0.01$ (a), $ff = 0.2$ (b), $ff = 0.6$ (c).

Since the periodicity of the medium in general depends on the direction of propagation, the dispersion curves are usually represented in direction-dependent diagrams. For a 2D square lattice, the frequency at which Bragg scattering occurs are determined for normal incidence (ΓX direction) and or an incidence angle of 45° (ΓM direction) from:

$$v_{\Gamma X} = \frac{c_{\text{sound}}}{2 \cdot L_c}, \quad v_{\Gamma M} = \frac{c_{\text{sound}}}{2\sqrt{2} \cdot L_c} \quad (1.38)$$

where L_c will hold from now on as the lattice constant of a sonic crystal. When dealing with acoustic wave and propagation in a medium, the formation of the band gap cannot be found obviously in the existence of a periodic potential, but some conclusions still hold. At Bragg frequency, i.e. at the boundary of the 1st Brillouin zone, a standing wave is formed inside the crystal due to the interaction of the incident and the back-scattered wave. Since standing waves have null group velocity, $v_g = \delta\omega/\delta k = 0$, the dispersion curves will assume a horizontal tangent moving towards the boundaries of 1st Brillouin zone, leading to the opening of a band gap. The envelope of the standing wave which is formed at Bragg frequency displays a maximum in between the cylinders, i.e. where the material with higher sound propagation velocity lies. Thus, for the same wavenumber, two different frequencies are possible due to the different sound propagation velocities inside the two media. The width of the band depends on the difference in velocity. Band structures are thus the solutions of the eigenvalue problem plotted in direction-dependent diagrams. The eigenvalue problem can be formulated by different means; the most common is the Plane Wave Expansion method⁵ and the Multiple Scattering Theory^{7;50}.

For this phenomenon to be appreciable, the crystal must show a certain filling fraction. Fig. 1.8 depicts three band structures calculated for a lattice constant $L_c = 0.10$ m, where the first Bragg band gaps are expected at 1,720 Hz for normal incidence (ΓX direction) and at 1,210 Hz for an incidence angle of 45° (ΓM direction). Three filling fractions are considered, 0.01, 0.2, 0.6 which implies, leaving the lattice constant unchanged, the radii of the cylinders to be 0.0056, 0.0252 and 0.0437 m respectively. The x-axis reports the reduced wave vector k , while y-axis reports the frequency. If the filling fraction is small,

Table 1.1: Wavelengths of the standing waves inside the sonic crystal reported as multiples or submultiples of the lattice constant a .

	$n = 1$	$n = 2$	$n = 3$	$n = 4$	$n = 5$	$n = 6$	$n = 7$
1 st harmonic	2Lc	4Lc	6Lc	8Lc	10Lc	12Lc	14Lc
2 nd harmonic	Lc	2Lc	3Lc	4Lc	5Lc	6Lc	7Lc
3 rd harmonic	2Lc
4 th harmonic	2Lc
5 th harmonic	2Lc
6 th harmonic	2Lc	...
7 th harmonic	2Lc

as in Fig. 1.8 (a), the wave propagation inside the crystal is not affected by the presence of the scatterers and the dispersion relation assumes linear values, according to the law $k = \omega/c$. Increasing the filling fraction to 0.2, Fig. 1.8 (b), a band gap opens in the ΓX direction (dark grey shade), centred around the Bragg frequency calculated above. With a filling fraction of 0.6, Fig. 1.8 (c), the band gap in the ΓX direction increases in width and band gaps open also for the ΓM and XM directions (light grey shade), leading to the formation of a complete band gap.

The formation of standing waves inside the sonic crystal at Bragg frequency can be derived theoretically from subsection 1.2. In fact, the opening of the band gaps occur at the boundaries of the 1st Brillouin zone, i.e. when the conditions for Bragg diffraction are met (cfr. Eq. 1.22). A very simple way to relate Bragg band gap to the multiple interaction of the sound wave inside the crystal is to consider the contribution that single lattice plane bring in terms of standing waves. Considering the sonic crystal in plan as a set of open-ended pipes, the behaviour of the sample can be analysed in terms of Fabry-Perot resonances. In particular, for both directions the first harmonics are reported in Table 1.1. From the diagonal values of the table, it is clear that the standing wave which is enhanced by the addition of rows of cylinders is the one corresponding to a wavelength of twice the lattice constant.

Chapter 2

Theoretical models

Three theoretical models have been used in this work to support the experimental evidences: the Plane Wave Expansion (PWE), the Multiple Scattering Theory (MST) and the Finite Element (FE) method.

The Plane Wave Expansion method is based on the solution of the wave equation by applying Bloch-Floquet theorem and expanding the properties of the media in Fourier series. In its basic formulation, it allows to calculate the band structure of the medium. The PWE method can be applied to arrays of any kind of scatterers but only infinite arrays can be modelled. The Multiple Scattering Theory is a formulation that computes the pressure field as a sum of the multiple scattering process. It generates when a wave impinging on a scatterer produces a scattered wave which in turn is scattered by the other scatterers and so on. The implementation of this method allows to compute the sound field generated by any array and no constrain on the periodicity or regularity of the array is required. Multiple scattering formulations have also been used to compute the band structures of periodic acoustic composites⁷. The Finite Element method is a numerical method to solve partial differential equations. The domain is discretised into small regions in which the differential equations are approximately solved. This meshing procedure allows to describe also complex geometries. This method is not widely used in acoustic scattering problems due to the computational costs and to its inborn inability to cope with unbounded domains. It is though a robust method to calculate sound pressure fields also through sonic crystals and can be used in together with other softwares, to calculate band structure.

In this work, the PWE method is used for the calculation of band structures, the MST is used for the determination of the pressure field for finite samples and the FE method is used for both purposes. Section 2.1 describes the theoretical background of the PWE method and the results of the calculation of band structures. Section 2.2 presents the self-consistent formulation of the MST and a study on the convergence of the method related to some lattice parameters. Section 2.3 reports the acoustic formulation of the FE method. The results from the three methods are finally compared in section 2.4.

2.1 Plane Wave Expansion method

As I have always pointed out, the first thing to do in any case where certain wave-lengths are absent as a result of an unknown process (...) is to find out where the absent wave-lengths have gone.

R.W. Wood, Phys. Rev. B **48**, 1935.

The Plane Wave Expansion is a powerful method to predict energy bands in periodic media which is based on the direct resolution of the wave equations⁵¹. With specific reference to acoustic applications, this method is powerful when the density contrast between the inclusions and air is very large, i.e. the waves that propagate inside the inclusions do not contribute significantly to the scattering of the acoustic wave in the air background. This method allows to model only infinite arrays arranged in a regular pattern, thus no finite or random media can be analysed. Moreover, it shows convergence problems due to the large numbers of plane waves required to calculate the band structures⁵². The following will mainly refer to the work by Kushwaha *et al.*⁵.

2.1.1 The PWE method for two-dimensional periodicity

The wave equation is given by:

$$\rho \frac{\delta^2 u}{\delta t^2} = \nabla \cdot (\rho c_l^2 \nabla u) \quad (2.1)$$

where u is the sound pressure, ρ is density of the medium and c_l is the sound velocity inside the medium. Consider a 2D periodic array of identical, infinite cylinders with arbitrary cross section immersed in air. Since the medium is periodic, its properties (ρ , c_l) can be expanded in Fourier series:

$$\begin{aligned} \rho(r) &= \sum_G \rho(G) e^{iGr} \\ \rho(r) c_l^2(r) &= \sum_G \Lambda(G) e^{iGr} \end{aligned} \quad (2.2)$$

where G are vectors of the reciprocal lattice. The sound pressure must satisfy the Bloch-Floquet theorem:

$$u(r, t) = e^{i(Kr - \omega t)} \sum_G u_K(G) e^{iGr} \quad (2.3)$$

where K is the Bloch wave vector. Substitution of Eqs. 2.3 and 2.2 into 2.1 leads to

$$\sum_{G'} [\Lambda(G - G') u_K(G') \cdot (K + G')(K + G) - \omega^2 \rho(G - G') u_K(G')] = 0 \quad (2.4)$$

If G takes all the points of the reciprocal lattice, Eq. 2.4 is a linear set of equations for the eigenvectors $u_K(G)$. For a given value of K , this set of equations has solution for some eigenvalues $\omega_n(K)$, where $n = 1, 2, \dots$ are the so-called *bands*.

If each unit cell is composed only of two materials a and b , then the Fourier coefficients in Eq. 2.2 assume a simpler form. The occupancy ratios for the two materials are defined as $ff = \pi r_0^2/A_c$, A_c being the area of the unit cell and r_0 the radius of the cylinders, and are respectively ff and $(1 - ff)$. Introducing the so called structure function F , for circular scatterers:

$$F(G) = A_c^{-1} \int_0^{r_0} r dr \int_0^{2\pi} e^{-iGr \cos\theta} d\theta = 2ff J_1(Gr_0)/(Gr_0) \quad (2.5)$$

where J_1 is the Bessel function of the first kind of order 1. Then the Fourier coefficients are:

$$\rho(G) = \begin{cases} \rho_a ff + \rho_b(1 - ff) \equiv \bar{\rho}, & G = 0 \\ (\rho_a - \rho_b)F(G) \equiv (\Delta\rho)F(G), & G \neq 0 \end{cases} \quad (2.6)$$

$$\Lambda(G) = \begin{cases} \rho_a c_{la}^2 ff + \rho_b c_{lb}^2(1 - ff) \equiv \bar{\rho} c_l^2 \equiv \bar{\Lambda}, & G = 0 \\ (\rho_a c_{la}^2 - \rho_b c_{lb}^2)F(G) \equiv \Delta(\rho c_l^2)F(G) \equiv (\Delta\Lambda)F(G), & G \neq 0 \end{cases} \quad (2.7)$$

The square lattice configuration has a reciprocal lattice vector defined in the PWE method as

$$G = \left(\frac{2\pi}{a}\right) (n_x x + n_y y) \quad (2.8)$$

Further developments of the method are represented by the *Extended Plane Wave Expansion*, which allow to compute the complex band structures⁵³ and the *supercell approximation*, which allows to calculate band structures of sonic crystals with point defects.

2.1.2 Band structures of sonic crystals

The band structures that follow, as well as those reported in Chapter 1, have been calculated by solving the eigenvalue problem exposed above and implemented in Matlab[®]⁵⁴. In these calculations, the integers n_x and n_y in Eq. 2.8 were allowed to take values between -10 and +10, providing 441 plane waves. One parameter has been changed at time in order to spot the emergence of band gaps in relation to the features of the PWE method. First, unit cells are analysed in which the lattice constant has been doubled, keeping the filling fraction unchanged by increasing the radius of the cylinder accordingly (Fig. 2.1). The general trend of the dispersion curves is the same in the two configurations, but the magnitude of the band gap opening is reduced and shifted down in frequency.

Then, the lattice constant has been kept unchanged at $Lc = 0.069$ m and the filling fraction has been varied from 0.3 to 0.7 by increasing the radius of the cylinder (Fig. 2.2). Band gaps occur in different frequency regions in the different directions of the first Brillouin zone. In particular, with a filling fraction of 0.3 four partial band gaps occur in

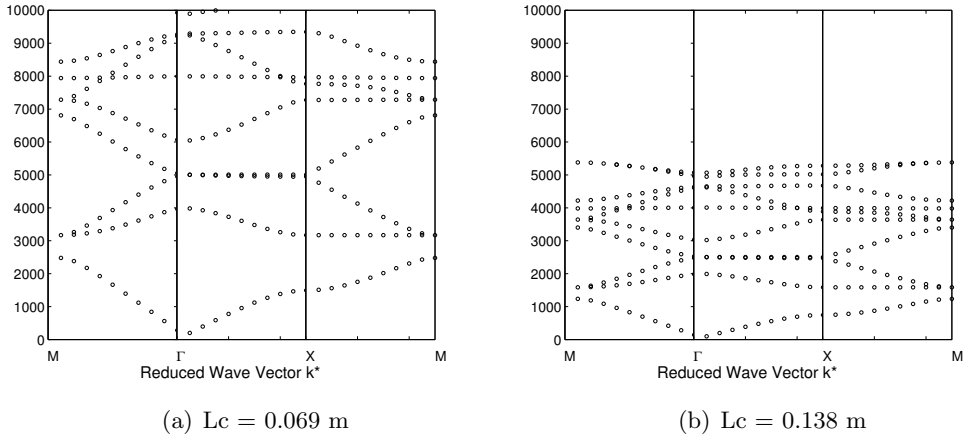


Figure 2.1: Dispersion curves calculated with the PWE method for two different arrays with filling fraction $ff = 0.5$ and lattice constant $L_c = 0.069$ m (a), $L_c = 0.138$ m (b).

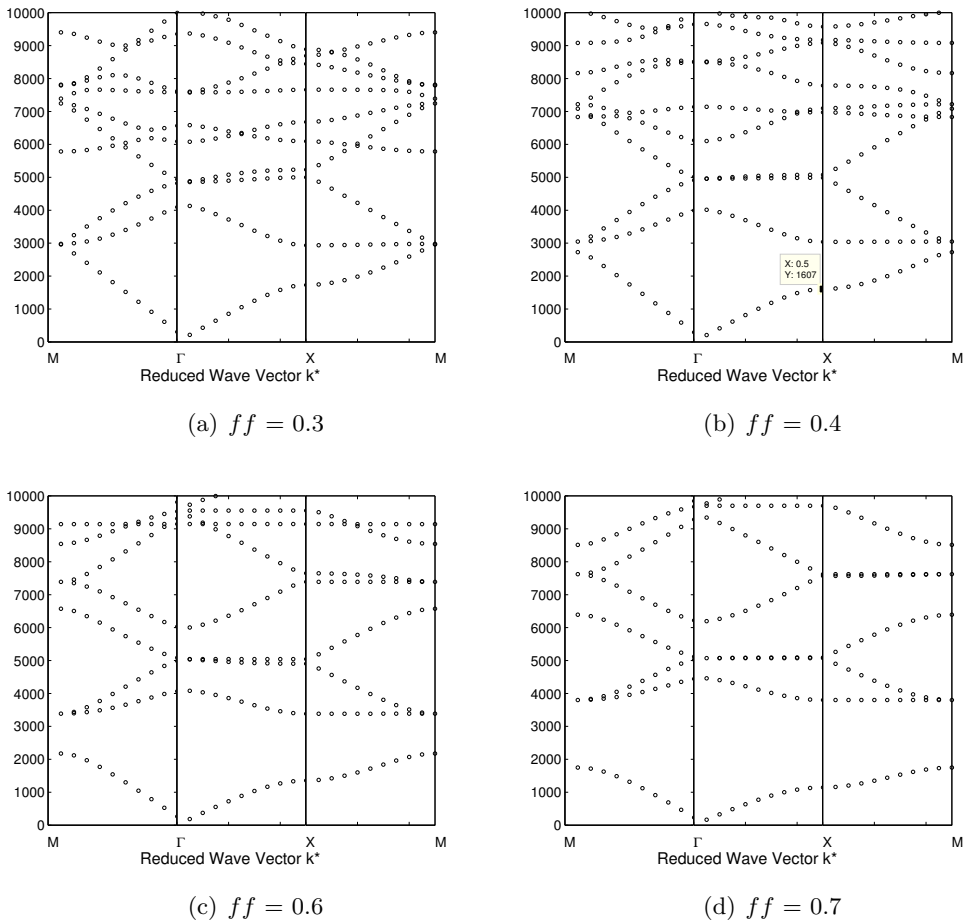


Figure 2.2: Dispersion curves calculated with the PWE method for three different arrays with lattice constant $L_c = 0.069$ m and filling fraction $ff = 0.3$ (a), $ff = 0.5$ (b), $ff = 0.6$ (c), $ff = 0.7$ (d). The configuration with $ff=0.5$ has been omitted as equal to Fig. 2.1 (a).

Table 2.1: Central frequencies of Bragg band gaps.

ff	0.3	0.4	0.5	0.6	0.7
ΓX	2,330 Hz	2,320 Hz	2,330 Hz	2,370 Hz	2,470 Hz
$X - M$	-	2,890 Hz	2,810 Hz	2,780 Hz	2,780 Hz

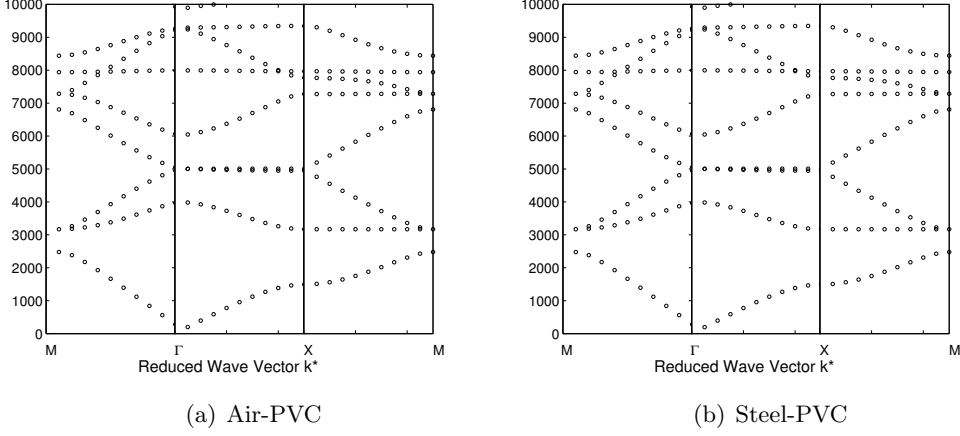


Figure 2.3: Dispersion curves calculated with the PWE method for three different arrays with different density constast. PVC cylinders (a) and steel cylinders (b) in air background.

the ΓX direction, the first one being located in the range 1730-2940 Hz. When the filling fraction is increased to 0.4, the four partial band gaps are shifted in frequency, the first BG spanning 1610-3040 Hz. A total band gap opens in the range 2730-3050 Hz while at higher frequencies only partial band gaps occur. Following the same trend, increasing the ff to 0.5, 0.6 and 0.7 the dispersion curves flatten, increasing the width of the band gap and and shifting upwards in frequency the occurrence of partial band gaps in the ΓX direction (see Tab. 2.1). Though the dispersion relations are modified in the vicinity of the band gap, the centre frequency of the BG can be approximately assumed to fulfill Eq. 1.38. For this lattice thus, Bragg scattering is expected to occur around 2490 Hz in the ΓX direction.

Finally, the density contrast between the materials has been changed by computing band structures of PVC cylinders and steel cylinders immersed in air (Fig. 2.3). The density contrast has been anyway kept high in order to maintain the hypothesis of rigid scattering and to continue considering negligible the scattering contribution due to waves propagating inside the cylinders. The band structures were computed for a square array of cylinders with $L_c = 0.069$ m and $ff = 0.5$. The mechanical properties of the materials are: $\rho_{air} = 1.2$ kg/m³, $\rho_{PVC} = 1,400$ kg/m³, $\rho_{steel} = 7800$ kg/m³, $v_{air} = 342$ m/s, $v_{PVC} = 2395$ m/s, $v_{steel} = 5740$ m/s. From Fig. 2.3 it is clear that the density contrast variation was not sufficient to generate any appreciable variation in the band structures.

2.2 Multiple Scattering Theory

Multiple scattering is the interaction of fields with two or more obstacles⁵⁵. The scattering by N cylinders has been approached with a variety of methods. The following refers to the direct method devised by Zaviska in 1913 and to the successive formulations^{56;55;37} for incident plane and cylindrical waves. First, a brief introduction will give an insight on the self-consistent approach and the difference with the n -th order of scattering approaches^{25;30}, and will mainly refer to the work by Martin⁵⁵. Next, the multiple scattering theory is formulated for plane and cylindrical incident waves after the works of Linton and Evans⁵⁶ and Umnova *et al.*³⁷. For the mathematical formulations, the reference is Gradshteyn and Ryzhik⁵⁷. Finally, the convergence of the MST codes based on Refs.^{56;37} and implemented in Matlab[©] is discussed.

2.2.1 The self-consistent method

The first approach developed to the multiple scattering is the single-scattering approximation, in which the total scattered field is the sum of the fields scattered by the single obstacles, computed as if each obstacle was isolated from the others. This method can be made recursive by extending it to other orders of scattering. This procedure is clearly formalised by Twersky²⁵:

...consider the s 'th cylinder as excited only by the incident plane wave, in response to which it scatters its "first order of scattering" (...single scattering approximation). Next, in response to all waves of the first order of scattering from the remaining cylinders, the s 'th cylinder scatters a wave of the "second order of scattering"... We proceed in this fashion to the m 'th order of scattering, and letting m approach infinity, sum the various order of scattering to obtain (...) the total wave scattered by the s 'th cylinder.

V. Twersky, J. Acoust. Soc. Am. **24** (1), 1950.

Recent literature agrees that this method provides a good match with experimental data even cutting the expansion procedure after the double-scattering term³⁰. The main drawback of this recursive procedure is that it becomes critical to handle as the number of bodies increases⁵⁶. Once the field scattered by each obstacle in isolation is known, the multi-obstacle problem can be solved by the self-consistent method, where the field acting on a scatterer includes the effects of all orders of scattering. In particular, the field associated to each cylinder is described as a general cylindrical wave radiating away from the cylinder by mean of an expansion in terms of Bessel functions. The multiple scattering problem is then solved using the Foldy-Lax self-consistent method⁵⁵, resumed in the following.

Consider an incident plane wave and a set of rigid cylinders in 2D. The total field is

given by:

$$p = p_{inc} + \sum_{j=1}^N p_{sc}^j \quad (2.9)$$

where p_{inc} is the given incident field and p_{sc}^j is the field scattered by the j -th cylinder. The field incident on the n -th cylinder in the presence of the other $N-1$ is given by:

$$p_n = p_{inc} + \sum_{\substack{j=1 \\ j \neq n}}^N p_{sc}^j \quad (2.10)$$

Since the problem is linear, it is possible to write:

$$p_{sc}^j = T_j p_j \quad (2.11)$$

being T_j an operator that relates the incident field on the j -th scatterer, p_j , to the field scattered by the j -th element, p_{sc}^j . We have:

$$p_n = p_{inc} + \sum_{\substack{j=1 \\ j \neq n}}^N T_j p_j \quad (2.12)$$

Solving for p_n we have:

$$p = p_{inc} + \sum_{j=1}^N T_j p_j \quad (2.13)$$

The first application of the self-consistent method was introduced by Lord Rayleigh and successfully adapted to problems in Solid State Physics by Korringa, Kohn and Rostoker; this is why it is often referred to as KKR method⁵⁸.

2.2.2 Incidence of a plane wave

The self-consistent multiple scattering problem as reported in the following takes as a reference the milestone paper by Linton and Evans⁵⁶ which deals with rigid cylinders immersed in air. The objective is to solve the Foldy-Lax problem with a radiation condition at infinity and some boundary conditions (BCs) at the cylinder-air interface.

Consider N vertical cylinders with radii a_j and infinite in length. $N+1$ coordinate systems are used: (r, θ) are polar coordinates in the (x, y) plane centred at the origin while (r_j, θ_j) , $j=1, \dots, N$ are polar coordinates centred at the centre of the j -th cylinder. An incident plane wave with incident angle β with respect to the x axis can be expressed as:

$$\phi_I = e^{ik(x\cos\beta + y\sin\beta)} \equiv e^{ikr\cos(\theta-\beta)} = I_j e^{ikr_j\cos(\theta_j-\beta)} \quad (2.14)$$

where $I_j = e^{ik(x_j\cos\beta + y_j\sin\beta)}$ is a phase factor associated with the j -th cylinder. From a Jacobi expansion it is possible to express a plane wave in terms of a sum of Bessel functions (see Gradshteyn⁵⁷, p. 923, MO27):

$$\phi_I = I_j \sum_{m=-\infty}^{\infty} J_m(kr_j) e^{im(\pi/2 - \theta_j + \beta)} \quad (2.15)$$

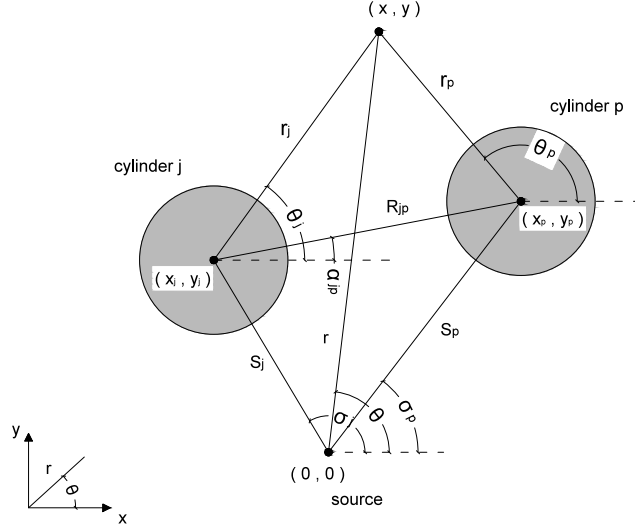


Figure 2.4: Cartesian and polar coordinates of the cylinders in the (x,y) plane.

In plane polar coordinates, the Helmholtz equation has separated solutions of the form $J_n(kr)e^{\pm in\theta}$ and $Y_n(kr)e^{\pm in\theta}$. To satisfy Sommerfeld's radiation conditions, the Hankel function of the first kind is considered: $H_n^{(1)}(kr)e^{\pm in\theta} \equiv [J_n(kr) + iY_n(kr)]e^{\pm in\theta}$, which represent an outwards propagating wave. The superscript ⁽¹⁾ for Hankel functions of the first kind is omitted in the following for sake of simplicity.

The field scattered by the j -th cylinder can be expressed as a general outgoing cylindrical wave, represented as an expansion of Hankel functions of the first kind centred at the origin of the coordinate system associated with cylinder j .

$$\phi_s^j = \sum_{n=-\infty}^{\infty} A_n^j Z_n^j H_n(kr_j) e^{in\theta_j} \quad (2.16)$$

where the unknown coefficients A_n^j are determined applying boundary condition on each cylinder. Coefficients Z are here introduced for later convenience and, for rigid cylinders, assume the values

$$Z_n^j = \frac{J_n'(ka_j)}{H_n'(ka_j)} \quad (2.17)$$

In order to set the boundary conditions on the j -th cylinder ($r_j = a$), each term of the scattered field must be expressed in the coordinate system of the j -th cylinder, i.e. as a function of (r_j, θ_j) .

This is possible by mean of the Graf's addition theorem for Bessel functions, that transform one expansion with respect to one point in a similar expansion with respect to another point. A formulation of Graf's addition theorem is found in Gradshteyn⁵⁷, p. 930, WA394(6), reported in the following with a slight change of notation coherent with

the symbols used before:

$$e^{im(\pi+\alpha_{jp}-\theta_p)} H_m(kr_j) = \sum_{n=-\infty}^{\infty} J_n(kr_p) H_{n+m}(kR_{jp}) e^{in(\pi+\alpha_{jp}-\theta_p)} \quad (2.18)$$

This formulation of Graf's addition theorem holds only for $r_p < R_{jk}$ and $r_p < S_p$, i.e. only if the evaluation point is closer to the centre of the cylinder rather than to the centre of any other cylinder or the source itself. This is certainly true on the surface of each cylinder, thus the equation above can be suitably used to describe boundary conditions on each cylinder. To solve the problem we need boundary conditions, which are usually expressed in terms of the total field:

$$\phi = \phi_I + \sum_{j=1}^N \phi_s^j \quad (2.19)$$

Using the addition theorem and replacing m by $-m$ in the double summation, the total field in the vicinity of cylinder p can be expressed as:

$$\begin{aligned} \phi(r_p, \theta_p) = & \sum_{m=-\infty}^{\infty} I_p J_m(kr_p) e^{im(\pi/2-\theta_p+\beta)} + \sum_{n=-\infty}^{\infty} A_n^p Z_n^p H_n(kr_p) e^{in\theta_p} + \\ & \sum_{\substack{j=1 \\ j \neq k}}^N \sum_{n=-\infty}^{\infty} A_n^j Z_n^j \sum_{m=-\infty}^{\infty} J_m(kr_p) H_{n-m}(kR_{jp}) e^{im\theta_p} e^{i(n-m)\alpha_{jp}} \end{aligned} \quad (2.20)$$

The first summation contains the incident field and second one represents the field scattered by the p -th cylinder. The third summation is the contribution of the scattered field of the j -th cylinders expressed in terms of the origin of the p -th cylinder.

Considering the mismatch between the elastic properties of the media, in particular $\rho_{cyl} \gg \rho_{air}$, we can assume rigid scatterers, i.e. Neumann boundary conditions.

$$\frac{\partial u}{\partial n} = 0 \quad i.e. \quad \frac{\partial u_{sc}}{\partial n} = -\frac{\partial u_{inc}}{\partial n} \quad on \quad r = a \quad (2.21)$$

Differentiating with respect to r_p , posing $r_p = a_p$ and considering the orthogonality of $e^{im\theta}$ we get:

$$A_m^p + \sum_{\substack{j=1 \\ j \neq k}}^N \sum_{n=-\infty}^{\infty} A_n^j Z_n^j e^{i(n-m)\alpha_{jp}} H_{n-m}(kR_{jp}) = -I_p e^{im(\pi/2-\beta)} \quad (2.22)$$

which is an infinite set of equation that can be solved by truncation. In particular, considering $m, n \in [-M; M]$ and N cylinders, it becomes a system of $N(2M+1)$ equations. Linton⁵⁶ pointed out that $M=6$ is sufficient to have accurate results in terms of convergence.

2.2.3 Incidence of a cylindrical wave

Consider a cylindrical source positioned at the origin of the coordinate system. The total field is given by the sum of the incident field, represented by a Hankel function of the first

kind, and the scattered field, expressed as for the plane wave, for some set of unknown coefficients.

$$\phi = H_0(kr) + \sum_{j=1}^N \sum_{n=-\infty}^{\infty} A_n^j Z_n^j H_n(kr_j) e^{in\theta_j}$$

where the Z factors are defined as in the plane wave case. The expansion of the incident wave in terms of Bessel functions and the application of Graf's addition theorem yield:

$$\begin{aligned} \phi(r_p, \theta_p) = & \sum_{m=-\infty}^{\infty} J_m(kr_p) H_m(kS_p) e^{im\theta_p} e^{-im(\pi-\sigma_p)} + \\ & \sum_{n=-\infty}^{\infty} A_n^p Z_n^p H_n(kr_p) e^{in\theta_p} + \\ & \sum_{\substack{j=1 \\ j \neq k}}^N \sum_{n=-\infty}^{\infty} A_n^j Z_n^j \sum_{m=-\infty}^{\infty} J_m(kr_p) H_{n-m}(kR_{jp}) e^{im\theta_p} e^{i(n-m)\alpha_{jp}} \end{aligned} \quad (2.23)$$

Again, the application of the Graf's addition theorem is restricted by $r_p < R_{jp}$ and $r_p < S_p$. These conditions are verified at the surface of the cylinders, thus Eq. (2.23) can be used to apply boundary conditions on each cylinder. In particular, the application of Neumann BC lead to an infinite set of equations that can be solved by truncation:

$$A_m^p + \sum_{\substack{j=1 \\ j \neq k}}^N \sum_{n=-\infty}^{\infty} A_n^j Z_n^j e^{i(n-m)\alpha_{jp}} H_{n-m}(kR_{jp}) = -H_m(kS_p) e^{im(\pi+\sigma_p)} \quad (2.24)$$

for $p = 1, \dots, N$ and $m = 0, \pm 1, \pm 2 \dots$

2.2.4 Implementation of a MST-based algorithm

A MST-based code has been implemented in Matlab[®] adapting a code based on Ref.³⁷ to implement Neumann boundary conditions on the cylinders and adding a plane wave source. The convergence of the algorithm is tested by changing some inputs of the system. In particular, three characteristic features of sonic crystals are considered: the filling fraction (ff), the distance of the receiving microphone from the sample (d) and the lattice constant (Lc). MST predictions are calculated on a 7×3 square lattice of cylinders. One of the three inputs discussed above was changed at a time, leaving the other two unchanged. Fig. 2.5 reports the frequency at which, for each case, the relative error between predictions performed with the truncation orders $M=5$ and $M=6$ is greater than 0.2 dB. The choice of $M=5$ and $M=6$ is arbitrary as well as the threshold, with the only aim of pointing out the behaviour of the algorithm. For sake of simplicity, the data are reported in relation to a "base" lattice constant $a = 0.069$ m. The black squares represent the predictions in which $ff = 0.5$, $Lc = a$ and $d = \{0.33Lc; Lc; 3Lc\}$. The white triangles represent the predictions in which $d = Lc$, $Lc = a$ and $ff = \{0.4; 0.5; 0.6\}$. The grey circles represent the predictions in which $ff=0.5$, $d = Lc$ and $Lc = \{a; 2a; 4a\}$.

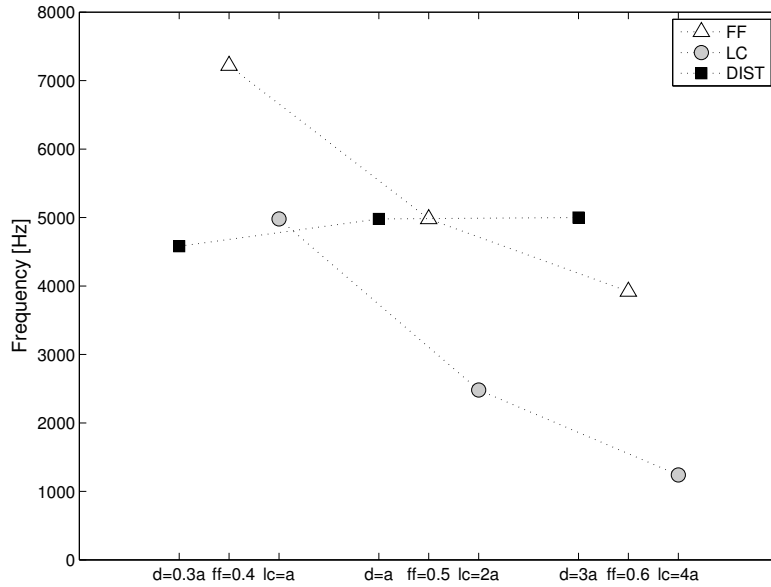


Figure 2.5: Convergence of the relative error.

Fig. 2.5 shows that the frequency up to which the truncation order provides reliable results is not strongly related to the distance of the microphone relative to the cylinders. It is instead strongly dependent either on the lattice constant and on the filling fraction. Great lattice constants require higher truncation orders, while smaller lattice constants require lower truncation orders. Since the frequency range in which reliable results are requested varies significantly with the filling fraction and with the lattice constant, for each of the arrays under study it is necessary to perform a convergence test to define the minimum truncation order to use in MST prediction considering the frequency range 400-6,000 Hz.

To define the minimum truncation order required to get reliable results, two arrays used for the measurements have been analysed. Array I has $d=0.135$ m and $ff=0.13$; array II has $d=0.069$ m and $ff=0.50$. In particular, for the two cases, MST predictions are computed at a point is chosen that had the same position relative to the sonic crystal, the truncation order varying from $M=4$ to $M=7$. The absolute values of the relative errors occurring between two consecutive truncation orders is shown in Fig. 2.6, where the dotted line represent a threshold of 0.5 dB. With that threshold, the minimum truncation order required is $M=5$ for both arrays. Considering a threshold of 0.1 dB (dashed line in Fig. 2.6), the truncation orders would be $M=5$ and $M=6$ for arrays I and II respectively, confirming thus the trend highlighted in Fig. 2.5.

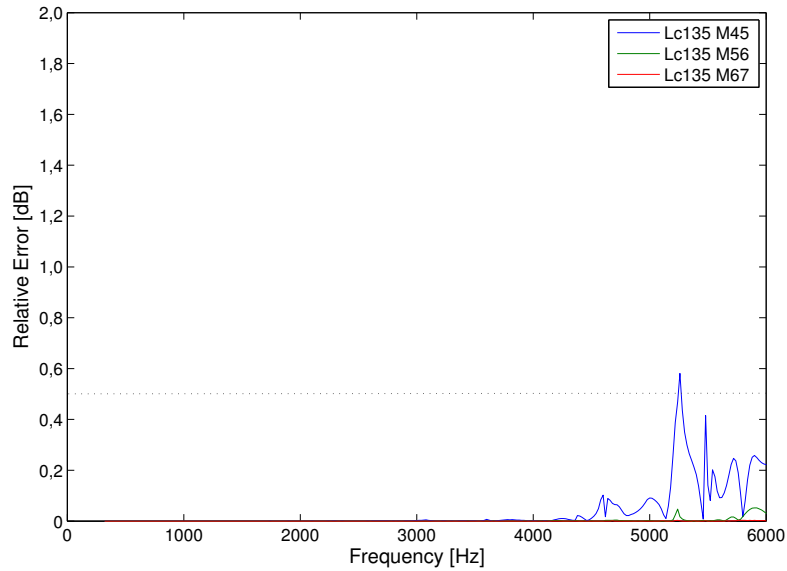
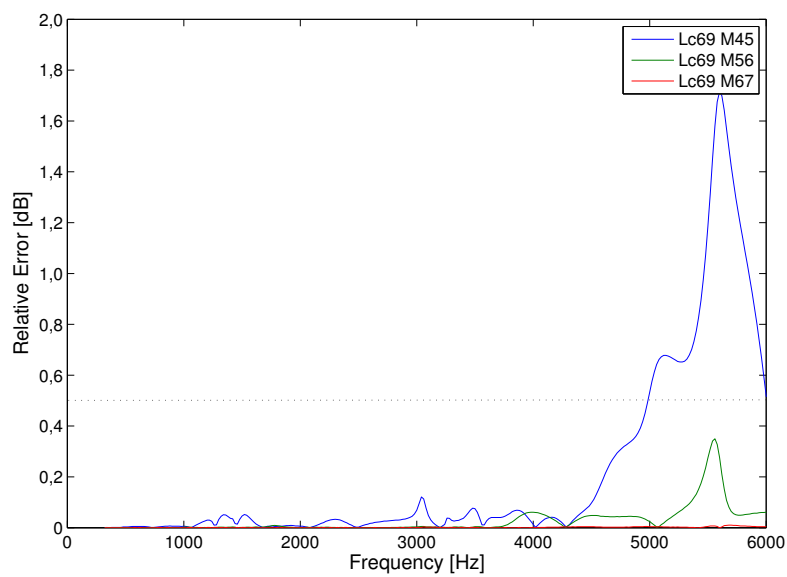
(a) Array I. $L_c = 0.135$ m, $ff = 0.13$ (b) Array II. $L_c = 0.069$ m, $ff = 0.50$

Figure 2.6: Absolute values of the relative errors between MST predictions computed with two successive truncation orders, varying from $M=4$ to $M=7$. Predictions were performed for two square 7×3 arrays: array I (a) and array II (b).

2.3 The Finite Element Method

The Finite Element method is a numerical method to solve partial differential equations. The main steps comprising the method are five: the definition of a strong formulation of the problem; the establishment of a weak formulation; an elementwise approximation of the unknown function over the entire body; the choice of a test function; the solution of the linear problem. The finite element method takes his name from the procedure of dividing the domain into smaller parts, the so called *finite elements* and to establish on them the approximation of the unknown, to finally extend the results on the entire region of interest. This is achieved by choosing the best suited element to mesh the domain and its *basis functions*, i.e. functions which are used to describe how the unknown varies within the element once the values that it assumes at the nodes are known.

Consider a differential equation in its strong formulation,

$$Lu + g = 0 \quad (2.25)$$

where L is a differential operator $u(x)$ is the unknown function, $g(x)$ is a known function and $a \leq x \leq b$ is the domain. Boundary conditions are given at $x = a$ and $x = b$. To derive the weak formulation, Eq. 2.25 must be multiplied by an arbitrary test function $\nu(x)$ and integrated over the domain:

$$\int_a^b \nu(Lu + g) dx = 0 \quad (2.26)$$

Note that Eq. 2.26 is still a strong formulation, as to get the weak form an integration by parts should be introduced. An approximate solution to the unknown function $u(x)$ can be assumed in the form:

$$u^{app} = \vec{\chi} \cdot \vec{a} \quad (2.27)$$

i.e. as a linear combination of the basis functions χ and coefficients a , which are the values that the unknown function assumes at the nodes. With this formulation it is possible to separate the information relative to the geometry of the mesh, through the basis functions which are defined once the geometry of the element is known, from the physical problem, i.e. the unknown coefficients at the nodes. The basis functions only depend on the geometry of the finite element and in general polynomials are used which include at least an arbitrary linear polynomial (completeness requirement) and which allow to achieve the continuity across the element boundaries (compatibility requirement). The choice of the approximated solution must satisfy the convergence criterion: the smallest the finite elements, the closer approximation will be to the solution. By substituting u^{app} to u , it will result

$$Lu^{app} + g = e \quad (2.28)$$

where e is the residual error, and by substituting into Eq. 2.26 we get the expression of the orthogonality of the functions $\nu(x)$ and $e(x)$, which serves to determine the a coefficients.

$$\int_a^b \nu e dx = 0 \quad (2.29)$$

The arbitrary test function ν can be written as

$$\nu = \vec{V} \cdot \vec{c} \quad (2.30)$$

where V are known functions and c are arbitrary coefficients which do not depend on x . Since ν is a number, and its transpose is equal to itself, and given that c are arbitrary and V are known, it is possible to write

$$\int_a^b \vec{V}^T e \, dx = 0 \quad (2.31)$$

Recalling Eqs. 2.27 and 2.28, Eq. 2.31 can be reformulated as:

$$\left(\int_a^b \vec{V}^T L(\chi) \, dx \right) a = - \int_a^b \vec{V}^T g \, dx \quad (2.32)$$

and again, using a more compact notation,

$$K \vec{a} = \vec{f} \quad (2.33)$$

where K is the coefficient matrix with dimensions $n \times n$, being n the number of nodes. This is a linear system to be solved with the unknown a in order to determine the approximate solution u^{app} . The Galerkin method, which belongs to the category of the weighted residual methods, consists in choosing the components V_i equal to the trial functions χ_i .

2.3.1 The acoustic formulation

The governing equations for the 2D propagation of a time-harmonic wave are:

$$\nabla^2 u + k^2 u = 0, \quad \text{in } \Omega \quad (2.34)$$

$$\frac{\partial u}{\partial n} + \beta u = g, \quad \text{on } \Gamma \quad (2.35)$$

where k, β are constants, $\partial u / \partial n$ denotes the outward normal derivative and Ω is a bounded domain with boundary Γ . To establish the weak form, Eq. 2.34 is multiplied by an arbitrary function - the so called weight function or test function ν - and integrated over the domain.

$$\int_{\Omega} \nu \nabla^2 u \, dx + \int_{\Omega} k^2 u \nu \, dx = 0 \quad (2.36)$$

Applying the divergence theorem to the first term in Eq. 2.36 and recalling the boundary conditions (Eq. 2.35), the weak formulation translates into finding u such that

$$\int_{\Omega} (\nabla u \nabla \nu - k^2 u \nu) \, dx + \beta \int_{\Gamma} u \nu \, ds = \int_{\Gamma} \nu g \, ds \quad (2.37)$$

holds for all ν . In this notation, dx is an element of area and ds is the element of arc length on Γ . The weak formulation is the basis for the application of the FE method and has some interesting mathematical advantages. First, the order of differentiation of the unknown function is decreased at the expense of the weight function being differentiated. This

implies that, when the Galerkin method is used in combination with a weak formulation, a symmetric coefficient matrix arises. Moreover, the weak formulation remains unchanged even in the presence of discontinuities, whereas the strong formulation would require further constraints. To solve Eq. 2.37, the finite element mesh must be defined together with the mesh size. The rule of thumb indicates that at least 10 elements per wavelength are required⁵⁹. Following the notation above, the approximate solution to u can be built as

$$U(x) = \sum_{j=1}^N u_j \chi_j(x) \quad (2.38)$$

where u_j are the unknown coefficients and $\chi_j(x)$ are the basis functions. Substituting Eq. 2.38 into Eq. 2.37 yields:

$$\sum_{j=1}^N \left[\int_{\Omega} (\nabla \chi_j \nabla \nu - k^2 \chi_j \nu) dx + \beta \int_{\Gamma} \chi_j \nu ds \right] u_j = \int_{\Gamma} \nu g ds \quad (2.39)$$

Since this equation holds for all ν , according to the Galerkin method the test function is chosen equal to the basis function, i.e. $\nu = \chi_m$, with $m = 1, \dots, N$. Thus the resulting linear system is:

$$\sum_{j=1}^N \left[\int_{\Omega} (\nabla \chi_j \nabla \chi_m - k^2 \chi_j \chi_m) dx + \beta \int_{\Gamma} \chi_j \chi_m ds \right] u_j = \int_{\Gamma} \chi_m g ds \quad (2.40)$$

for $m = 1, \dots, N$, which can be solved using numerical techniques.

The elementary solution of the Helmholtz equation e^{ikr} is periodic, with wavelength $\lambda = 2\pi/k$. The mesh resolution n_{res} is defined as

$$n_{res} = \frac{\lambda}{h} \approx \text{constant} \quad (2.41)$$

where h is the mesh size and λ is the wavelength considered. When dealing with Galerkin FE analysis, the asymptotic error estimate can often be expressed as:

$$\frac{\|u\| - \|U\|}{\|u\|} \leq Ch^2 \quad (2.42)$$

which holds for h sufficiently small. C depends on f , on the approximate solution u and on the wavenumber k . k represents the oscillatory nature of the exact solution, which becomes critical at high frequencies. This is solved by imposing a fixed number of elements per wavelength. As pointed out before, a rule of thumb requires $n_{res} = 10$ when interpolating an oscillatory function, and the computational costs increase accordingly. For large values of k pollution errors arise, due to the wave not being modelled properly and the error propagating through the numerical solution. Many solutions have been proposed to solve this issue and a more detailed discussion is reported in Ihlenburg⁵⁹.

The use of finite element methods in acoustics is troublesome in acoustic scattering applications with unbounded domain. To ensure the uniqueness of the solution, in this case Sommerfeld radiation conditions must be imposed that demand:

$$u(x) = O\left(r^{-(d-1)/2}\right), \quad (2.43a)$$

$$\frac{\partial u}{\partial r}(x) - iku(x) = o\left(r^{-(d-1)/2}\right) \quad (2.43b)$$

as $r \rightarrow \infty$, where r is the radial direction and d the dimension of the problem. The Sommerfeld radiation conditions cannot be included into the variational formulation due to a mismatch on the order of the test functions⁵⁹, thus different solutions have been searched to allow the computation of unbounded domains with the FE method.

One solution is to truncate the infinite domain by introducing an artificial boundary B that determines two regions: a bounded domain of interest Ω and a residual infinite domain D . A non-reflecting boundary condition (NRBC) is derived on B in order to avoid spurious reflections. Then, this NRBC is used to solve the problem in Ω by using the FE method⁶⁰, incorporating thus the far-field behaviour into the Finite Element model.

A most recent solution is the introduction of Perfectly Matched Layers (PML). PMLs were first introduced in 1994 by Berenger⁶¹ applied to electromagnetic computations. The idea is to introduce an exterior layer at the artificial boundary in order to inhibit reflection for an arbitrary angle of incidence, and to make the transmitted wave vanish at infinity. Due to the exponential decay within this layer, though the computation is truncated at a finite distance within the layer, the resulting artificial reflections are small. In mathematical terms, PML consists of the linearised Euler equations which are reformulated by adding a damping factor (σ in⁵⁹) and expressed through a coordinate transformation that scales to complex coordinates so that any wave impinging on this layer decays in the direction perpendicular to the interface between the PML and the physical domain⁶².

2.3.2 Extraction of dispersion curves using the FE analysis

Dispersion curves can be calculated using FE method. In this work, thanks to a collaboration with Eng. M. Miniaci and Eng. A. Marzani, band structures have been calculated by looping the commercial softwares Matlab[©] and Comsol Multiphysics[©].

Here are reported the results of band structure calculation considering cylinders immersed in air and arranged in a square lattice. A lattice constant of 0.20 m is chosen, expecting the first Bragg BG at around 860 Hz. Two inclusions have been considered: a PVC bar of radius $r = 0.08$ m and a hollow PVC cylinder with outer radius $r = 0.08$ m, thickness $t = 3.2$ mm. Unit cells are presented in Fig. 2.7 along with proper periodic boundary conditions in terms of pressure distribution, while the properties of the materials used in the calculations are presented in Tab. 2.2. For both the considered cases, band structures are computed along the three high symmetry directions of the first irreducible Brillouin zone ΓX , XM and $M\Gamma$ using the FE method and exploiting the Bloch-Floquet

Table 2.2: Properties of the materials used in the FE analyses.

Material	Density ρ [kgm^{-3}]	Longitudinal wave speed c_L [ms^{-1}]	Shear wave speed c_S [ms^{-1}]
Air	1.25	343	-
PVC	1400	2142	874

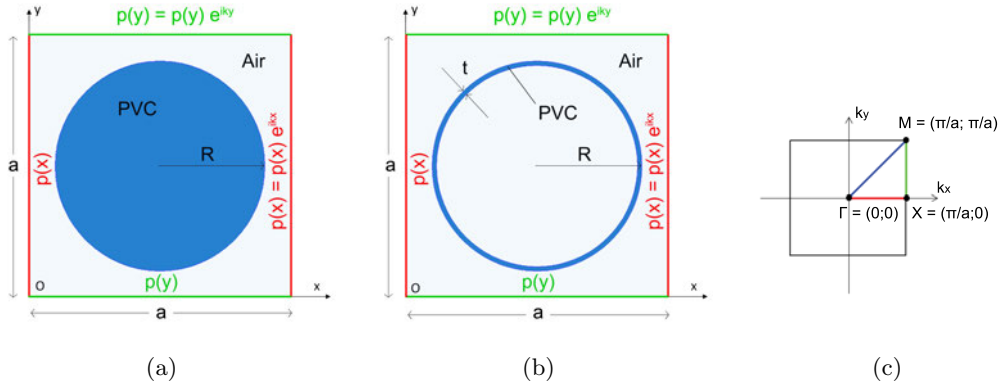


Figure 2.7: The unit cells together with the boundary conditions: (a) Air-PVC bar unit cell; (b) air-PVC hollow cylinder unit cell and (c) the first Brillouin zone.

theorem with the aid of the commercial software Comsol Multiphysics[©]. The unit cell domains are modelled under 2D plane strain assumption exploiting the “Acoustic-Solid interaction” module and meshed by means of 3-node triangular elements of maximum size 0.01 m to provide accurate eigensolutions up to 2,500 Hz. In particular, the modelling of the hollow cylinder required a mesh refinement up to $3.2 \cdot 10^{-3}$ m in correspondence of the inclusion. The analyses of the resulting eigenvalue problems are solved using the PARDISO algorithm for the ΓX , XM and $M\Gamma$ paths. A detailed description of the procedure to extract the band structures can be found in Refs.^{63;64}.

The band structures are presented in Fig. 2.8 in terms of the reduced wave vector $\mathbf{k}^* = [k_x a/\pi; k_y a/\pi]$, where k_x and k_y are the wave vectors in the x and y directions, respectively. At least one complete band gap (BG, dark grey rectangle) as well as partial band gaps (light grey rectangles) exist in the range 0 - 2,500 Hz frequency range for each unit cell. In particular, a complete band gap extends from 860 Hz to 1,110 Hz for case (a) and from 870 Hz to 1,120 Hz for case (b). In the latter case, an additional lower complete band gap between 150 and 200 Hz is nucleated. Fig. 2.8 suggests that, due to the high acoustic mismatch between air and PVC, the complete band gap centred at around 1,000 Hz mainly depends on the outer shape of the inclusion rather than on the geometrical differences of the considered inclusions⁶⁵. Thus, in the following while barriers of hollow cylindrical pipes will be tested experimentally, numerical FE harmonic simulations will consider filled pipes to alleviate the computational needs.

Some bands in Fig. 2.8 exhibit nearly flat portions in the ΓX (a) and ΓX , $M\Gamma$ (b) paths. Modes associated to such flat band portions are supposed to have a nearly zero

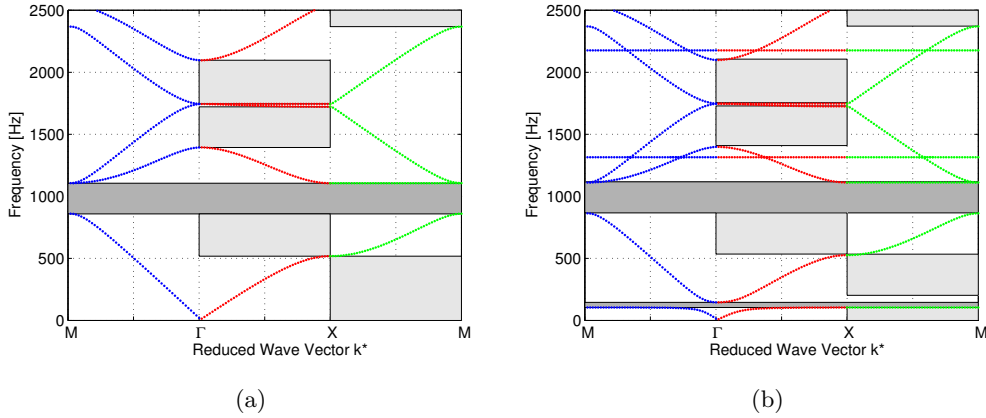


Figure 2.8: Band structures for (a) air-PVC bar unit cell and (b) air-PVC hollow cylinder unit cell in the first irreducible Brillouin zone.

group velocity, thus to be characterised by a strong spatial localisation³⁵. Finally, it is worth noting that some waves coalesce at the high symmetry point M outside the band gap boundaries, as it occurs between second and third curves for the filled cylinder or between third and fourth curves for the hollow cylinder.

2.3.3 FE modelling of sonic crystals

The band structure analysis shows that filtering properties exist in an infinite sonic crystal barrier made of cylinders with a proper spatial arrangement. However, in order to quantify the magnitude of such attenuation, the finite length of the sonic crystal must be taken into account. To this end, FE time-harmonic analyses are performed on a finite-size sonic crystal.

Fig. 2.9 shows the computational domain used for the case of a barrier made of 3 rows of cylinders for plane wave and spherical wave propagation. Since the windowing procedure allows to cut off the ground reflection and the edge diffraction effects, the cylinders are modelled as a bi-dimensional domain constrained on the sides in order to compute the transmitted sound component only. Moreover, due to the similarity in the band structures in Fig. 2.8, in these simulations the hollow PVC cylinders are modelled as filled to ease the generation of the FE mesh. Neumann boundary conditions (acoustically hard surfaces) are applied to their perimeters. The two domains corresponding to different wave spreadings are modelled differently. For plane wave calculations, one side of the rectangular domain is the sound source, and the opposite side is modelled with a PML in order to simulate Sommerfeld's radiation conditions. The other two sides are modelled as reflecting surfaces, due to the well-known problems encountered with absorbing boundary condition for a wave propagating parallel to the boundary interface. The choice of a reflecting wall leaves the propagation of the incoming plane wave unchanged but provides lateral reflection which can be thought as generated by mirror sources located beyond the boundary. In this way the sample is characterised as infinite in the direction normal to

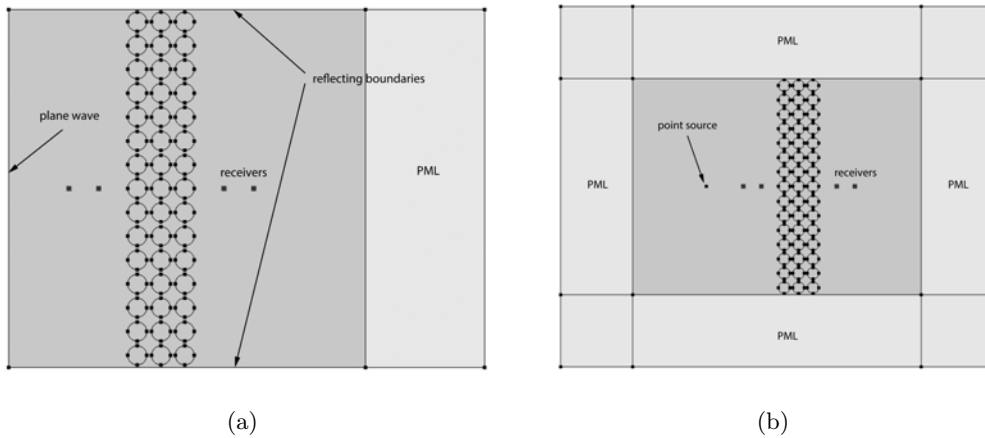


Figure 2.9: Computational domains and boundary conditions used for the FE modelling with an incident plane wave (a) and with a point source (b).

the wave vector of the incoming plane wave. Predictions with a point source allowed the use of a finite array of cylinders, thus PMLs are applied to all the boundaries. In both cases, the thickness of the PML was chosen of 1 m to be effective in the lower frequency range of interest. In order to provide accurate results up to 2,500 Hz, a mesh made of constant strain triangular elements of maximum edge size of 0.01 m is set. The source radiation characteristics are reproduced using a point source excitation that provides a pressure level of 94 dB at a distance of $L_s = 1$ m from the first row of pipes or, for the plane wave propagation, with a pressure amplitude of 1 Pa, corresponding to 94 dB. Sound attenuation, evaluated as the difference between the spectra with and without the sonic crystals, is extracted at the same in the two test configurations.

Sound insulation values calculated with the FE method for incidence of plane and spherical waves are shown in Fig. 2.10. The dashed line represents the FE predictions with point source while the and dotted line represents the plane wave source. The first Bragg band gap is well identified by both kinds of sound source, while the second band gap is characteristic only of the plane wave propagation, consistently with the results provided by band structures calculations. The plane wave simulation predicts a very smooth insulation profile in frequency. An exception is given at around twice Bragg frequency, where a tangential component of the sound field determines the failure of the PML. Figure 2.11 shows the pressure maps of the sound field near the cylinders at different frequencies. At Bragg frequency (860 Hz) no sound propagates through the sonic crystal. At 1,000 Hz the sound transmission increases slightly with respect to the configuration before, while sound reflection is strongly increased. At 1,720 Hz sound transmission is prevented again, but an anomaly emerges due to some numerical artefact related to the selectivity of PMLs, who work properly only when excited by waves propagating normally to the domain-PML interface.

The calculation of the sound field using both plane and spherical waves allows on one side to refer to the results predicted by the band structure calculations (PWE), to the

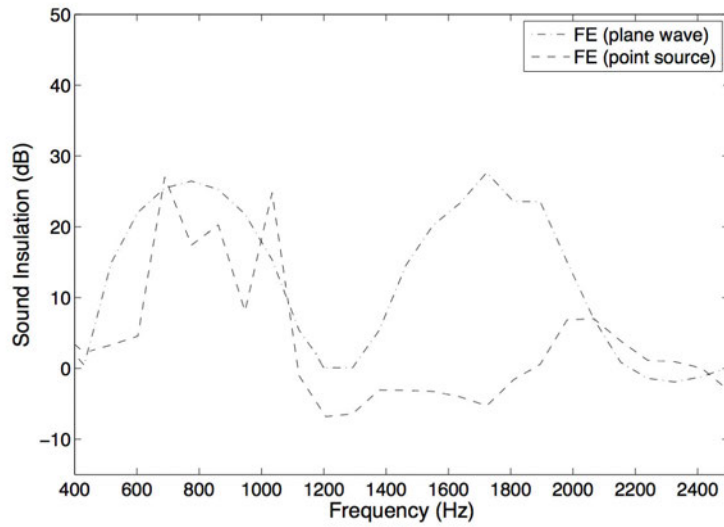


Figure 2.10: Sound insulation (dB) calculated with the FE method for spherical and plane wave propagation on an array of 15x3 cylinders.

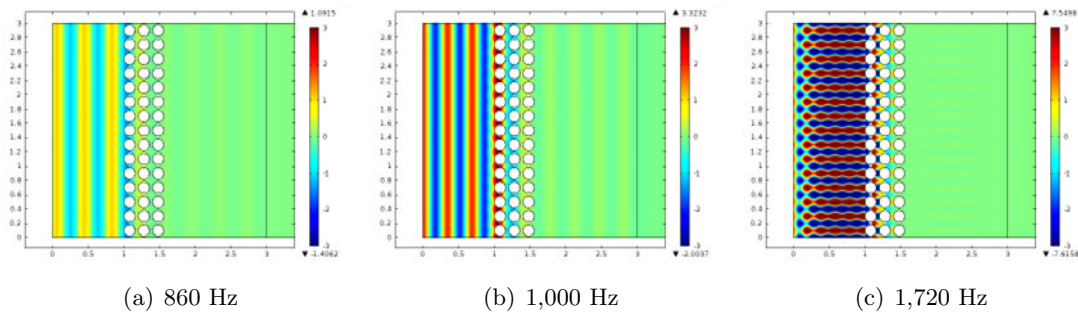


Figure 2.11: Sound pressure field computed with Comsol Multiphysics[©] for a 3-rows sonic crystal for plane wave propagation.

results of the MST (plane wave) and on the other side to connect FE analysis to the results of the measurements, performed with a point source. Indeed, in Chapter 3 the comparison between numerical predictions and experimental measurements is made consistent by a combination of assumptions adopted in the FE models and in the experimental acquisition procedure. In particular: (i) the single point sound insulation is computed at a point that lies at the same height of the sound source; (ii) the frequency steps in the time-harmonic analyses are set in accordance to the maximum frequency resolution achievable due to the windowing procedure of the impulse responses (IRs); (iii) the application of a time window is mimicked in the numerical model introducing PMLs (which allow to neglect the reflections from the boundaries), limiting the domain in width (thus preventing edge diffraction effects) and assuming a two-dimensional plane strain domain (to avoid ground and top barrier edge reflections).

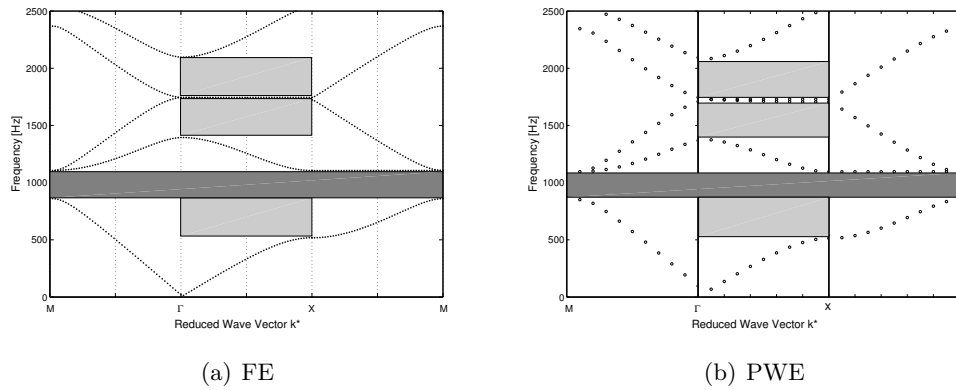


Figure 2.12: Band structures calculated with the FE method (a) and the PWE method (b) for a 15x3 square array of cylinders with radius 0.08 m and $L_c = 0.200$ m.

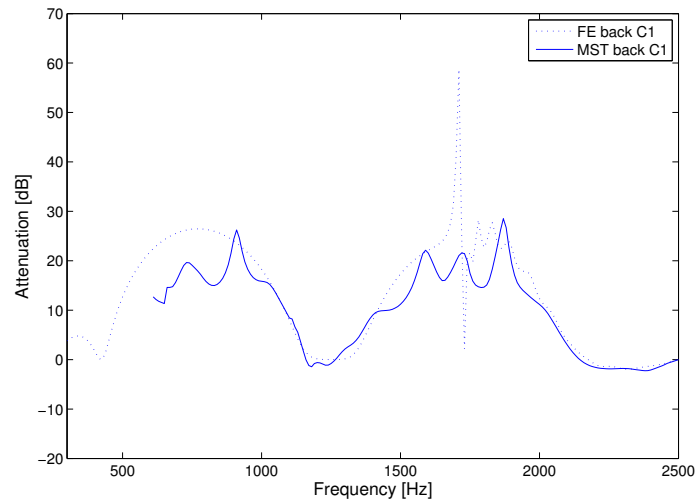
2.4 A comparison between the methods

The availability of a number of analytical tools allows to perform comparisons between the numerical calculations.

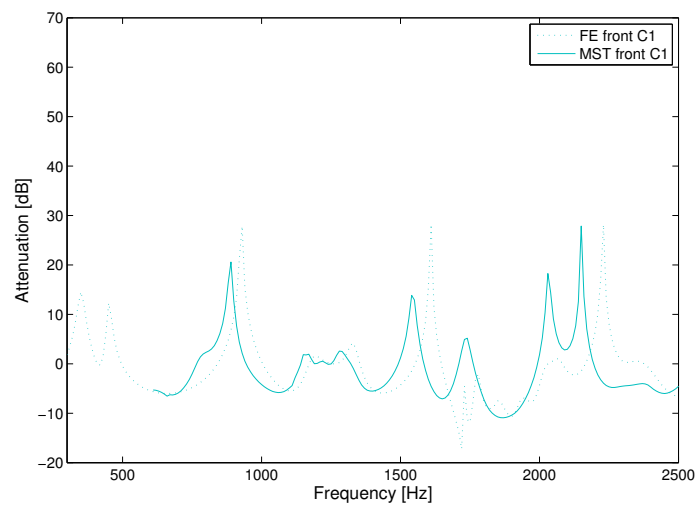
Band structures have been calculated with the PWE method and the FE method looped with Matlab[®], the unit cell consisting of a cylinder immersed in air with lattice constant $L_c = 0.200$ m and radius $r = 0.08$ m. The results show very good agreement. The first band gap is predicted in the range 850-1,100 Hz by the PWE method and in the range 860-1,110 for the FE method. The first partial band gaps match equally well: 510-1100 Hz for PWE calculations and 518-1110 Hz for FE calculations.

MST calculations have been performed implementing plane and cylindrical sources; FE calculations implemented plane and spherical waves. Thus a comparison between MST and FE calculations is provided by the characterisation of sonic crystals using plane wave sources. The same array analysed for the FE/PWE comparison is considered here. The sound pressure field transmitted and reflected by the sonic crystal has been calculated using the two methods and results for a receiver are reported in Fig. 2.13. The spectra of the reflected sound field shows an evident frequency shift between the FE and the MST calculations which increases with frequency, though convergence has been tested for both methods. The attenuation peaks at around 900 Hz display a difference of about 40 Hz between the two methods while the peaks at 2,200 Hz show a difference of about 80 Hz. This shift does not occur for the transmitted sound field. With specific reference to the FE calculations, these results are presented with a greater frequency resolution with respect to last section, thus the numerical artefact arising at twice Bragg frequency discussed in section 2.3 is clearly evident.

Finally, the FE method was also used to compute the scattered field with a point source. This provides a benchmark to test the experimental measurements which will be discussed in the next chapter.



(a) Transmission



(b) Reflection

Figure 2.13: Attenuation spectra computed with the MST and the FE method for plane wave propagation. Insulation (a) and reflection (b) results for a 15×3 square array of cylinders with radius 0.08 m and $L_c = 0.200$ m.

Chapter 3

Experimental results

This chapter reports the results of the experimental measurements performed on sonic crystals in the Acoustic Laboratory of the Department of Engineering and Innovation at the Open University (UK) and in the Acoustic Laboratory of the Department of Industrial Engineering at the University of Bologna. The two facilities are described in detail together with the procedures used to process the gathered data. Then the results of the measurements are presented divided into four categories. First, the sound field transmitted and reflected by the sonic crystal has been evaluated in discrete points. Then, the sound pressure field inside the arrays has been investigated by moving the microphone along the two symmetry axes of the arrays and evaluating the sound pressure pattern and the evanescent behaviour of modes inside the crystal. At the University of Bologna, a further set of measurements was conducted using an intensity probe. Moreover, the standardised indices for sound insulation and reflection were calculated in order to compare sonic crystals to other screening techniques.

3.1 The measurement facilities

Experimental measurements have been conducted on sonic crystals in two laboratories: the Acoustic Laboratory of the Open University in Milton Keynes (UK) and the Acoustic Laboratory of the Department of Industrial Engineering at the University of Bologna. The two measurement facilities provided different test conditions: in the UK measurements were conducted in an anechoic chamber while at the University of Bologna measurements were done in a large industrial hall. Three square arrays were tested, the unit cell consisting of hollow PVC cylinders immersed in air. The lattice constant and/or the filling fraction of the sonic crystal varied between the samples in order to set up a comparison on a reduced number of variables.

3.1.1 The anechoic chamber at the Open University (UK)

The anechoic chamber at the Open University hosted the first measurement campaign. The dimensions of the anechoic chamber are approximately 3 x 3 x 3 m . In one wall of

Table 3.1: Temperature and relative humidity measured inside the anechoic chamber at the Open University during the measurements.

Day	Lc	Measurement	T (°C)	RH (%)	v_{sound} (m/s)
16/12/14	135	Ins/Ref 1, SW	17.9÷18.3	50	342.3
19/01/15	135	Ins/Ref A,	14.8÷15.4	47	340.5
19/01/15	69	Ins/Ref 1, Ins/Ref A	15.9÷16.2	48	341.0
19/01/15	69	SWT	16.2÷16.4	48	341.2
20/01/15	69	SWL	13.6÷14.0	42	339.7

the chamber there is a small hole - properly sealed during the measurements - that allows cables to pass and thus to perform measurement remotely from outside the chamber. The measurement chain consists of:

- Brüel & Kjær 4191 1/2" free-field microphone with type 2669-B preamplifier;
- Brüel & Kjær 4187 1/4" pressure microphone with type 2670 preamplifier;
- Brüel & Kjær dual channel microphone power supply type 5935;
- Cambridge Audio stereo A1 amplifier;
- Tannoy driver with a brass pipe 1 m long fixed to the end (inner diam. 1.8 cm);
- Computer running MLSSA.

During the measurements, the temperature and the relative humidity were monitored and are reported in Table 3.1 together with the relative speed of sound derived from $\nu \approx 331.4 + 0.6 \cdot T_c$ (m/s).

A square array of 7 x 3 hollow PVC cylinders was arranged in the anechoic chamber (Fig. 3.1). The pipes are 2 m high, have an outer diameter of 0.055 m and a thickness of 1.9 mm. The cylinders were fixed by means of two MDF boards in which 0.055 m diameter holes are drilled. One board was secured to the lower part of the sample and the second one to the top of the sample to assure static stability. Two lattice constants were analysed, $Lc_1 = 0.135$ m (array I) and $Lc_2 = 0.069$ m (array II), resulting respectively in filling fractions $ff_1 = 0.13$ and $ff_2 = 0.50$. The source and the microphone were set at an height of 0.90 m from the ground, the microphones lying on the vertical axis. The source was set at a distance of 1 m from the closest cylinder, pointing at the centre of the array, while the position of the receivers are discussed in the next sections..

An anti-aliasing Chebyshev filter with a bandwidth of 25 kHz was applied to the input signals. IR measurements were performed using Maximum Length Sequence (MLS) test signals with a length of 64k samples, the sampling rate set at 75.5 kHz. To improve the Signal to Noise Ratio, 32 time averages were carried out for each measurement.

As pointed out above, the source consisted of a driver with a brass pipe 1 m long fixed to the end, so that its extremity can be considered a point source. The resonance inside the pipe generated a secondary pulse which is delayed with respect to the first pulse by

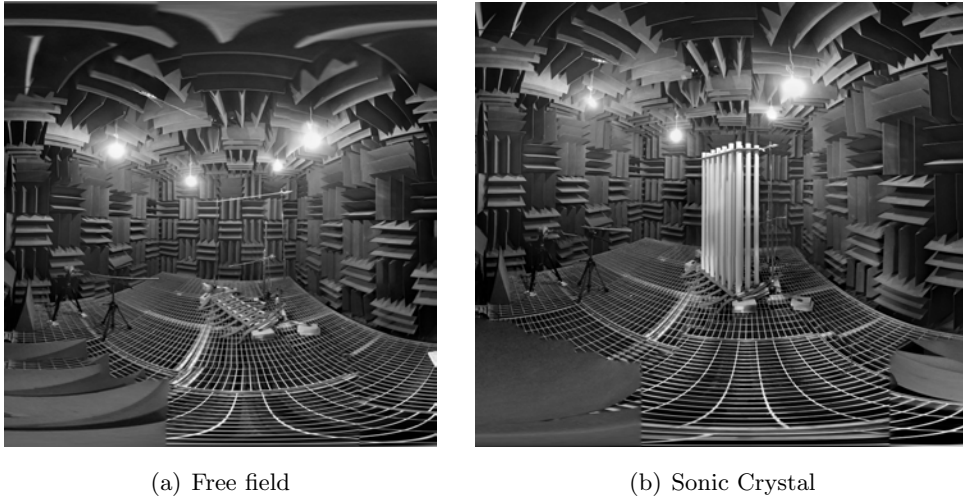
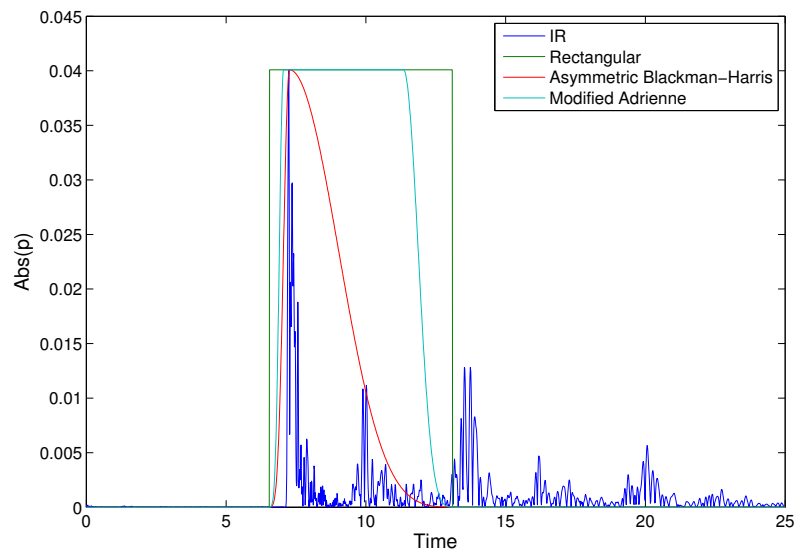


Figure 3.1: Panoramic view of the anechoic chamber of the Open University for the free field measurement (a) and the measurement with the sample interposed (b).

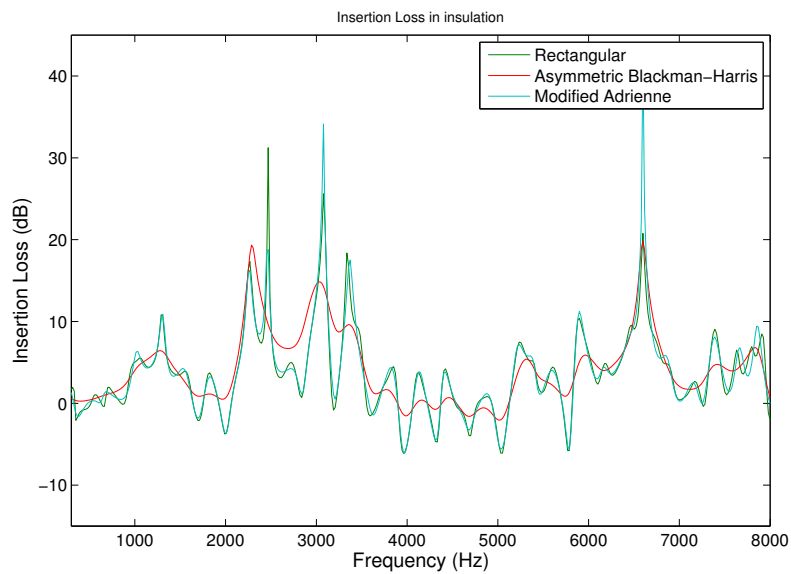
approximately 6 ms, i.e. twice the time needed to span twice the length of the pipe. This rendered necessary the use of a time window that isolates the primary pulse. Since 6 ms correspond to about 2 m of multiple reflections, the windowing procedure is not expected to affect the data significantly.

For free field measurements, the time instant at which the window is applied is determined upon the maximum of the IR, corresponding to the direct field, and shifted back by 0.2 ms. For the insulation measurements, the standard EN 1793-6⁶⁷ determines the time instant of application of the window by geometrical consideration, due to the fact that no direct component is detected as the pressure field is governed by diffraction. For sonic crystals, the direct component is clearly detectable on the IR and correspond to its maximum, thus the time instant of application of the window is determined also in this case from the maximum of the IR.

Figure 3.2 displays three different time windows applied to the same IR and the Insertion Loss (IL) values derived using them. In particular, a rectangular, a asymmetric Blackman-Harris and a modified Adrienne windows were used. The total length of the windows is 6.5 ms and was chosen with reference to the Adrienne window. In fact, according to the EN 1793-6 standard⁶⁷, the flat portion of the Adrienne window must begin 0.2 ms before the arrival of the direct sound and an additional left-half Blackman-Harris of 0.5 ms is applied before the flat portion. Thus all windows are applied 0.7 ms before the arrival of the direct component. The asymmetric Blackman-Harris window is made of: (i) a leading edge having a left-half Blackman-Harris shape and a total length of 0.7 ms; (ii) a trailing edge having a right-half Blackman-Harris shape and a total length of 5.8 ms. These two edges meet at the maximum of the IR measured in the free field. The modified Adrienne window is made of: (i) a leading edge having a left-half Blackman-Harris shape and a total length of 0.5 ms; (ii) a flat portion having a total length of 4.26 ms; (iii) a trailing edge having a right-half Blackman-Harris shape and a total length of



(a)



(b)

Figure 3.2: The different time windows applied to a IR: rectangular, asymmetric Blackman-Harris and modified Adrienne window. Visualisation of the time windows over the measured IR (a) and Insertion Loss computed in the three cases (b).

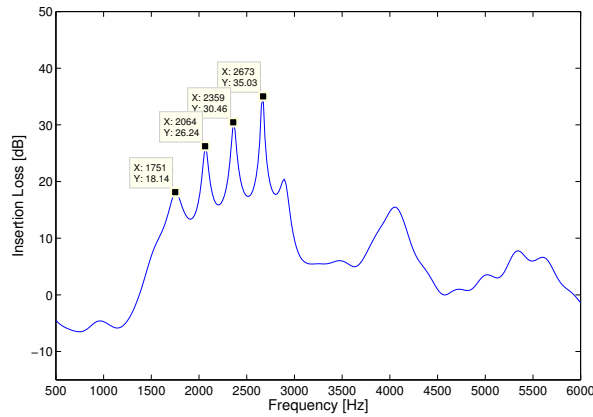


Figure 3.3: Influence of the floor grille on the calculation of the Insertion Loss. This figure plots the IL measured at point SWT5 and windowed with a 6 ms right-half Blackman-Harris window. Peaks are found with a regular spacing of 300 Hz and are related to the floor grille in the relative free field measurement.

1.74 ms. The dimensions of the window were adapted to the arrival time of the secondary pulse, respecting the 7/3 ratio between the flat portion and the trailing edge required by Ref.⁶⁷. The comparison between these three windows shows that the rectangular and the modified Adrienne time window provide similar results, with a significant oscillation in frequency. Some artefacts arise due to the window and are evident with regards to the magnification of some IL values at certain frequencies.

After 3 ms from the arrival of the direct sound, a reflection was found that could be attributed to the floor grille. Though the Blackman-Harris time window has the advantage of minimising the effects of the ground reflections, having a steep slope, the effects of the pavement grill are still concerning in the spectra of the free field IRs. In particular, this was noticed from the IR measured inside the sonic crystal in position SWT5, the IL of which is reported in Fig. 3.3. The analysis on the relative free field measurement showed that floor grille was responsible for the peaks found with a regular spacing of 300 Hz. Thus a further analysis was conducted on a free field measurement and the corresponding measurement with the sonic crystal interposed. Two different time windows with two different lengths were used to analyse the free field measurement: a rectangular window and a right-half Blackman-Harris window with a length of 3 ms and 6 ms respectively, as shown in Fig. 3.4. Fig. 3.4 (c) reports the spectra of the rectangular and Blackman-Harris 6 ms time windows and Fig. 3.4 (d) reports the spectra of the Blackman-Harris time windows of 3 and 6 ms respectively. The rectangular window shows its typical artefacts but some oscillations are found also with the 6 ms Blackman-Harris time window. The different windowing procedure on the free field measurement affects significantly the results. Fig. 3.5 plots the attenuation measured at the position corresponding to the free field IR analysed above. The need to cancel the ground reflection implies the waste of useful signal, and adds a certain degree of uncertainties to

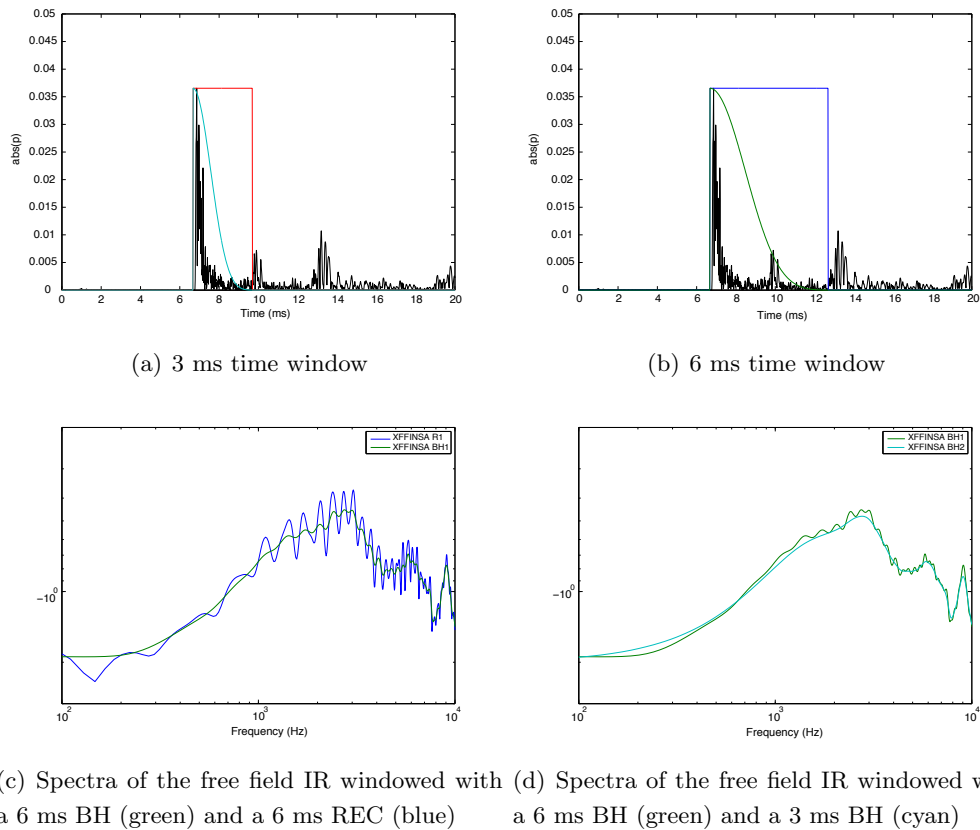


Figure 3.4: Comparison between time windows of different lengths and shapes. (a) and (b) report respectively the 3 ms and 6 ms rectangular and Blackman-Harris time windows plotted over the absolute value of the free field IR. (c) reports the spectra of the rectangular and Blackman-Harris 6 ms time windows and (d) reports the spectra of the Blackman-Harris time windows of 3 and 6 ms respectively.

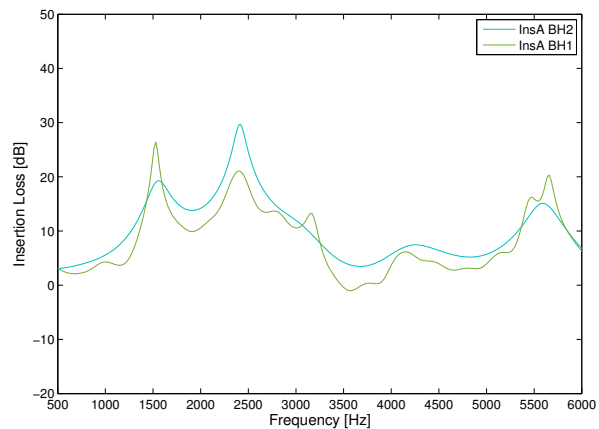


Figure 3.5: IL measured behind the sonic crystal using a 6 ms (green) and a 3 ms (cyan) right-side Blackman-Harris window.

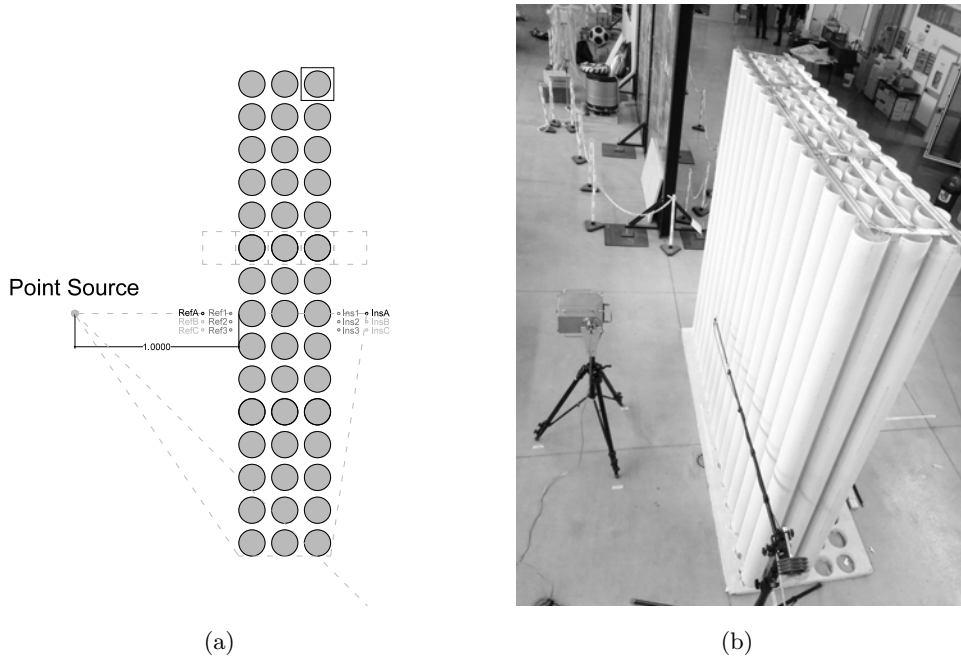


Figure 3.6: Measurement setup at the Acoustic Laboratory of the University of Bologna. Position of the source and the microphone array for the sound reflection and the sound insulation indices (a) and picture of the setup from above (b).

the results of the measurements. This is particularly critical for reflection measurements. Luckily, the lower frequency of interest is not affected by that windowing limit as the first Bragg band gap occurs approximately at 1,270 Hz for array I and at 2,490 Hz for array II.

After the windowing procedure, a 4096 points FFT is calculated and the attenuation provided is given by the dB-ratio of the power spectra of the IRs measured in free field and with the sample. In particular, the results are returned in terms of Insertion Loss (IL), namely

$$IL = -20 \log_{10} \frac{p_w}{p_{w/o}} \quad (dB) \quad (3.1)$$

i.e. the logarithmic difference between the pressure field with and without the barrier. Though the definition of Insertion Loss does not include the minus⁶⁸, the definition proposed here is the most commonly found in the literature.

3.1.2 The Acoustic Laboratory of the University of Bologna

The Acoustic Laboratory of the University of Bologna is a large industrial hall with a volume of about 5,000 m³ currently used to test noise barriers according to the standards EN 1793-5⁶⁶ and EN 1793-6⁶⁷. Measurements were performed over a 3 x 3 m sample consisting of PVC pipes 3 m long, with an outer diameter of 0.16 m and a thickness of 3.2 mm. The cylinders were arranged in a 15 x n square lattice, where n varied from 2 to 5. The lattice constant was $Lc_3 = 0.200$ m and the filling fraction was $ff = 0.50$ (array

Table 3.2: Temperature and relative humidity measured inside the Acoustic Laboratory at the University of Bologna during the measurements.

Day	Lc	Measurement	T (°C)	RH (%)	v_{sound} (m/s)
18/2/15	200	Ins/Ref A, SW	21.8÷22.5	34	344.7
26/2/15	200	Sound Intensity	25.3÷20.9	25	345.3

III).

This lattice has been chosen to test a configuration which could be effective for traffic noise. The sonic crystal was designed to exhibit a complete band gap in the one-third octave bands from 800 Hz to 1,250 Hz, i.e. the frequency range in which tyre/road noise spectrum shows a prominent peak⁶⁹. The lattice constant was thus set in accordance to the Bragg scattering theory; looking for a band gap in the one-third octave band with centre frequency at approximately 1,000 Hz, the resulting lattice constant is 0.17 m, given $c_{air} = 343$ m/s the speed of sound in air at 20°C. To comply to the ease of fabrication, a lattice constant of 0.20 m was chosen, expecting the first Bragg frequency at around 860 Hz. Using a tailored time window, the dimensions of the sample allow to compute the transmitted field only, neglecting the contributions of ground reflection and edge diffraction.

The cylinders were fixed by means of a stratified board (plywood, plasterboard and polyester) on the ground and by some aluminium profiles on the top. This fastening system does not provide top edge reflections and allowed to perform measurements which take into account top diffraction. The source and the microphone were set at an height of 1.5 m from the ground, the microphones lying on the vertical axis. The source was set at a distance of 1 m from the closest cylinder, pointing at the centre of the array. The measurement equipment consisted of:

- PCB 130E20 1/4" microphone
- PCB Piezotronics signal conditioner;
- Crown XLS 1000 amplifier;
- Fireface 800 sound card;
- MCIRMS (internally developed) software;
- Zircon loudspeaker.

During the measurements, the temperature and the relative humidity were monitored and are reported in Table 3.2 together with the relative speed of sound. Figure 3.6 (a) displays the measurement positions considered for the sound insulation and sound reflection measurements.

The measurements positions were chosen according to Fig. 3.6. The points at a fixed distance of 0.050 m which were analysed at the Open University were considered too influenced by the reactive part of the sound field and thus were not taken into account.

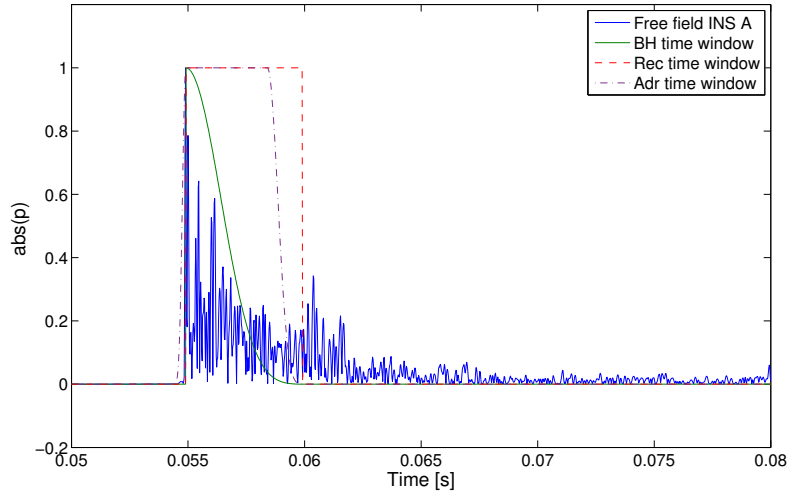


Figure 3.7: Time window used to cancel the ground reflection at the University of Bologna: a 5 ms Blackman-Harris centred on the arrival of the direct sound; a 5 ms rectangular time window and a modified Adrienne time window. The IR is a free field measurement: the ground reflection is clearly visible.

Only points Ins A, B, C and Ref A, B, C were considered, lying at a distance of $1 L_c$ from the sample. Inside the crystal, measurements were performed with a resolution of $1/4$ of the lattice constant. Since measurements were performed in a laboratory and no impulsive background noises were present, IR measurements were performed using 128k Exponential Sine Swept (ESS) test signals sampled at 44.1 kHz, which were proved to be better suited in these conditions⁷².

The analysis of these data followed closely the procedure used to process the IR measured at the OU, the IL being calculated according to Eq. 3.1. Where not specified, the IRs are windowed with a 5 ms right-half Blackman-Harris time window. In this way, only the transmitted component is taken into account as ground reflection and top and edge diffractions are windowed out (see Fig. 3.7). To compute the sound insulation and reflection with an increasing number of rows of cylinders, a modified Adrienne time window is used, made of (i) a leading edge having a left-half Blackman-Harris shape and a total length of 0.5 ms; (ii) a flat portion having a total length of 3.5 ms; (iii) a trailing edge having a right-half Blackman-Harris shape and a total length of 1.5 ms. The same time window is used to compute the standardised sound insulation and sound reflection indices, as discussed in detail in section 3.5.

3.2 Sound transmission and sound insulation measurements

This section reports the result of the transmission and reflection measurements performed on the three array, whose properties are reported briefly in Tab. 3.3.

The measurement position chosen to evaluate the sound field transmitted and reflected

Table 3.3: Specifications of the three arrays investigated.

Name	Lc (m)	ff	1 st BG in ΓX (Hz)	Location
Array I	0.135	0.13	1,270	OU
Array II	0.069	0.50	2,485	UniBO
Array III	0.200	0.50	858	UniBO

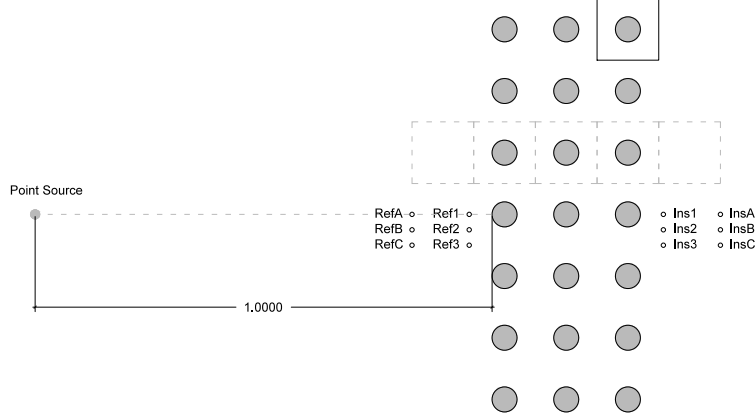


Figure 3.8: Insulation and reflection measurement positions. Points labeled A, B, C lie at a distance of 1 lattice constant from the edge of the external unit cells; points labeled 1, 2, 3 lie at a fixed distance of 0.05 m from the external cylinders.

by the sonic crystal is sketched in Fig. 3.8 together with the nomenclature. In both setups, the source was set at a distance of 1 m from the closest cylinder, pointing at the centre of the array. Two different sets of measurement positions were chosen lying respectively at a fixed distance of 0.05 m from the cylinders (positions labelled 1, 2, 3) and at 1 Lc from the array (labelled A, B, C). Within the same set of measurement points, the microphone was shifted along the sample covering three measurement positions, spaced apart by $1/4$ of the lattice constant (Fig. 3.8). The first position has the microphone facing the central cylinder; the third sees the microphone between two adjacent cylinders and the third is in an intermediate position between the two. This choice is due to the fact that there are great differences between the arrays considered and since the source-receiver position has always been kept at 1 m, the characteristics of the sound field scattered by the cylinders will diverge completely in the three different cases.

Arrays I and II are made by 7×3 unit cells while array III is a $15 \times n$ unit cells. When not specified, it is assumed that array III is also comprised of 3 rows of cylinders, in order to leave a greater amount of variables unchanged between the configurations. Measurements on arrays I and II are processed using the same time window, which is tailored to cancel the secondary pulse and, more restrictively, the grille reflection. Thus, since the lattice constant is doubled, the IL values relative to the array with smaller lattice

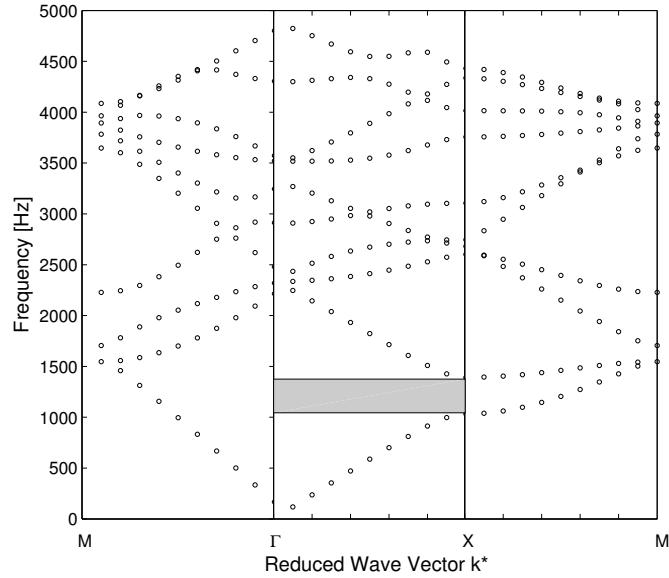


Figure 3.9: Dispersion curves for a square array with $L_c = 0.135$ m and $r = 0.0275$ m evaluated using the PWE method.

constant will take into account a greater quantity of the sound field diffracted from the edges. This does not occur for array III, where the length and height of the sample are the same. In this case, the time window which allow to cancel ground reflection cancels also top and side diffraction.

3.2.1 Array I

The first array under test has $L_c = 0.135$ m and $ff = 0.13$. The first Bragg band gap for normal incidence is expected at $f_{Bragg,\Gamma X} = 1,270$ Hz. The band structures calculated with the PWE method (Fig. 3.9) spot a partial band gap in the ΓX direction in the range 1,040-1,400 Hz.

The IL values calculated in the aforementioned points is presented in Fig. 3.10. The analysis of insulation at points 1, 2, 3 (Fig. 3.10 a) shows that the first attenuation peaks occurs at Bragg frequency, and that up to this frequency the difference between measurements at positions 1, 2, 3 is negligible. The highest attenuation is achieved at frequencies higher than the Bragg frequency, confirming that with such low filling fraction the stop-band properties typical of sonic crystals have not totally emerged yet.

With reference to the transmitted and reflected sound field measured at point 1 (Fig. 3.10 e), it is interesting to notice that at Bragg frequency reflection is close to zero, while negative values of IL would be expected due to the constructive interference generated by Bragg scattering. Moreover just below 2,000 Hz both insulation and reflection measurements have a negative value, implying constructive interference on both sides of the sample. Opposite values are found instead between 2,000 and 3,500 Hz at measurement point 3 (Fig. 3.10 f).

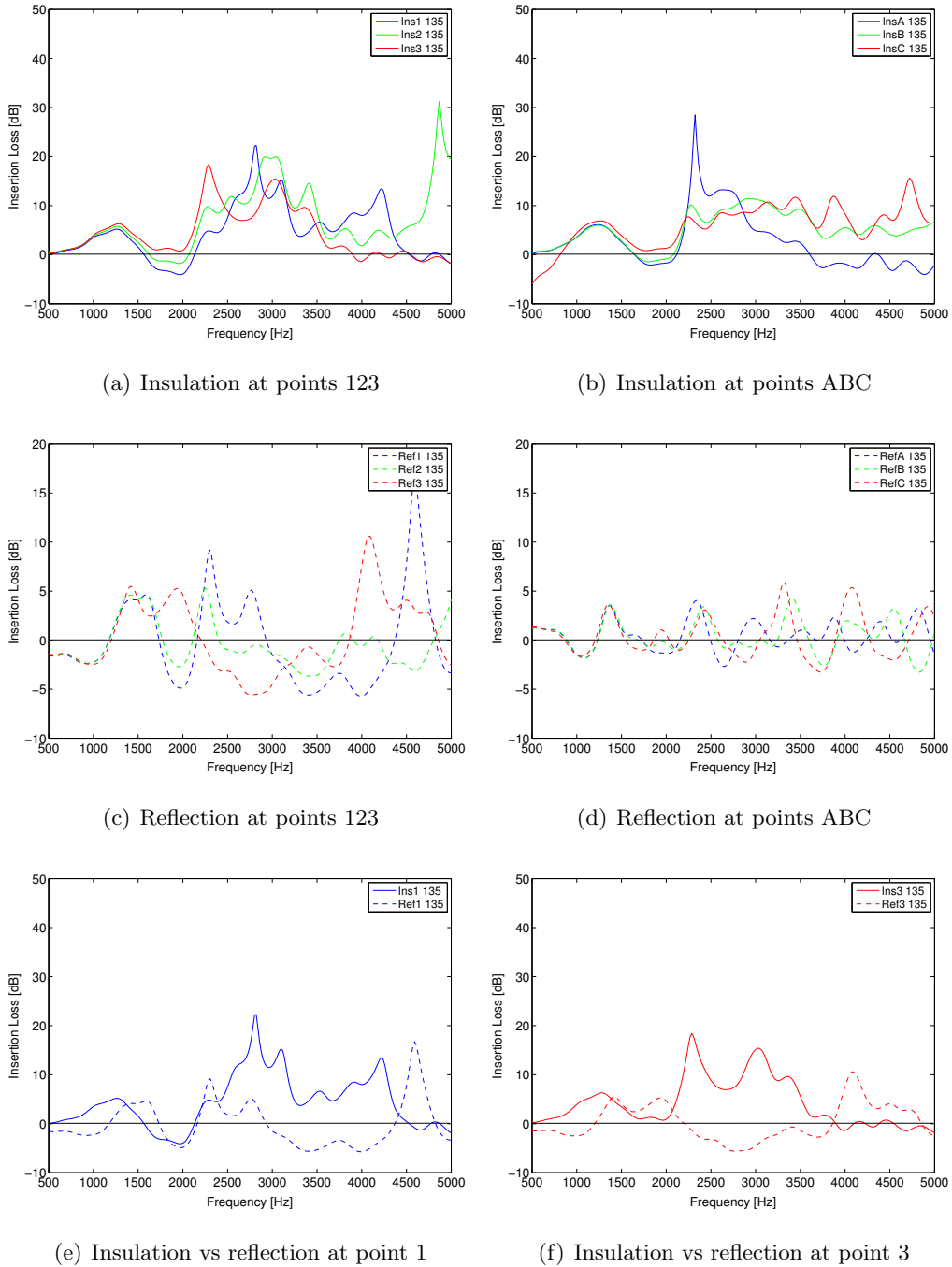


Figure 3.10: Array I. Insertion Loss at positions 1, 2, 3 and A, B, C for insulation and reflection measurements.

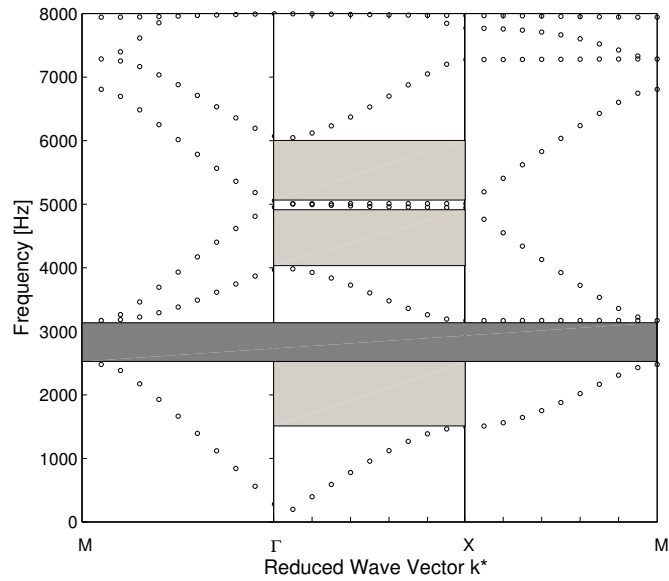


Figure 3.11: Dispersion curves for a square array with $L_c = 0.069$ m and $r = 0.0275$ m evaluated using the PWE method.

As mentioned above, measurements positions 1, 2, 3 were chosen at a fixed distance of 0.05 m from the cylinders; for the lattice constant $L_c = 0.135$ m, that means that the measurement point lies almost on the edge of the unit cell. Thus results might be strongly influenced by the sound field generated inside the crystal and not return a global characterisation of the sound field generated by the sonic crystal.

Measurements in points A, B, C were chosen to overcome this limit, as their distance from the cylinders is related to the lattice constant. Insulation measurements at these points match insulation measurements at points 1, 2, 3 (Fig. 3.10 b) whilst reflection measurements do not show any appreciable agreement (Fig. 3.10 b), excluding the fact that points A, B, C return overlapping values up to 1,480 Hz. Thus, the measurements related to this second set of points are considered not significant to the analysis.

3.2.2 Array II

The second array under test has $L_c = 0.069$ m and $ff=0.50$. The first Bragg band gaps are expected at $f_{Bragg,\Gamma X} = 2,485$ Hz for normal incidence and at $f_{Bragg,\Gamma M} = 1,757$ Hz for an incidence angle of 45° . The band structures calculated with the PWE method (Fig. 3.11) spot a complete band gap in the range 2,480-3,170 Hz. In the ΓX direction, the width of the band gap is greater and extends down to 1,510 Hz. A second band gap is clearly visible on ΓX spanning the range 3,980-6,050 Hz. The measured values of IL in the control points referred to above are reported in Fig. 3.12.

The trend of the IL of the transmission measurements sound field displays two main crests, centred at multiples of the Bragg frequency for normal incidence (Fig. 3.12 a). Below Bragg frequency, some components show up at 1,000 Hz, showing attenuation

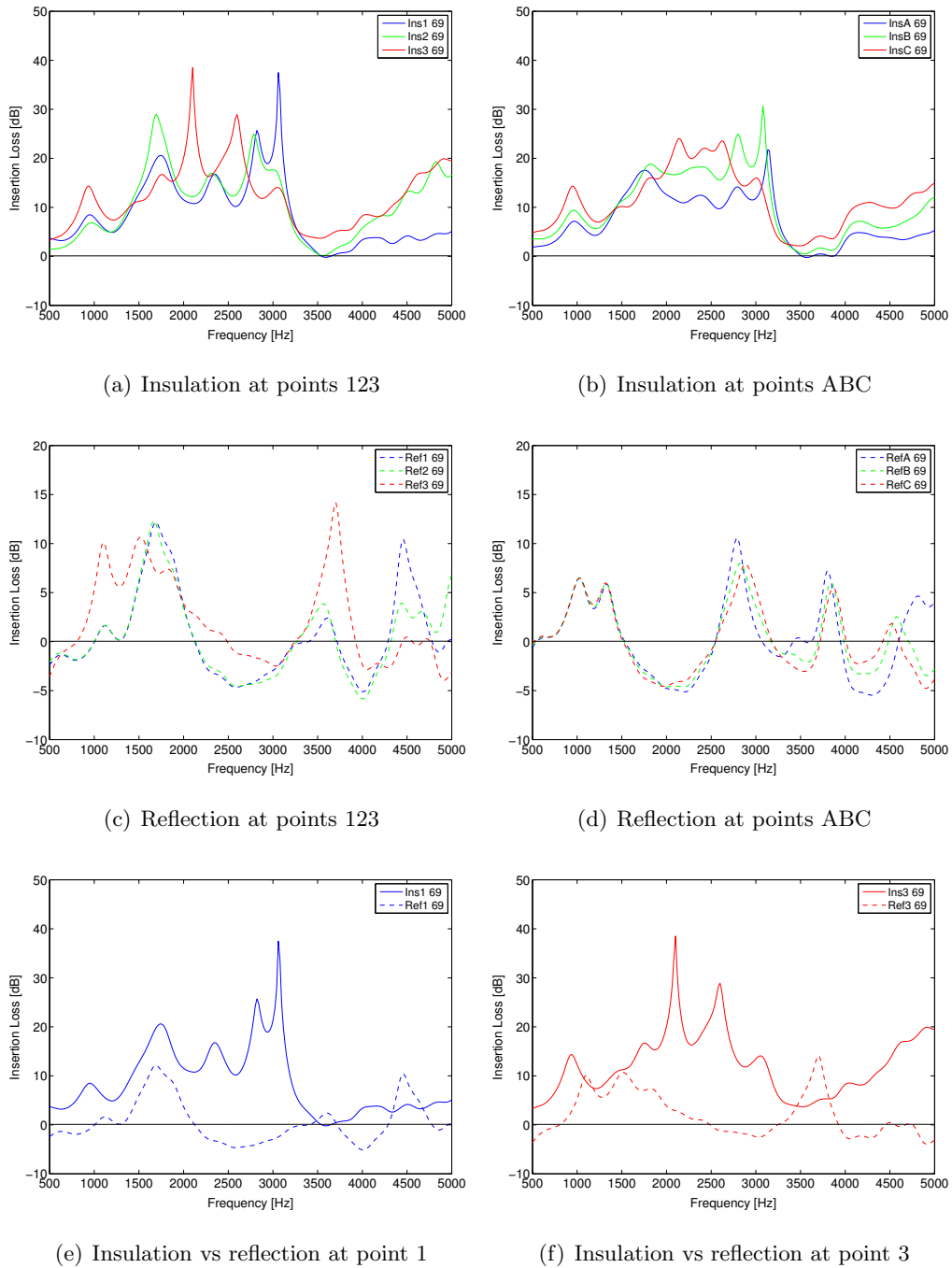


Figure 3.12: Array II. Insertion Loss at positions 1, 2, 3 and A, B, C for insulation and reflection measurements.

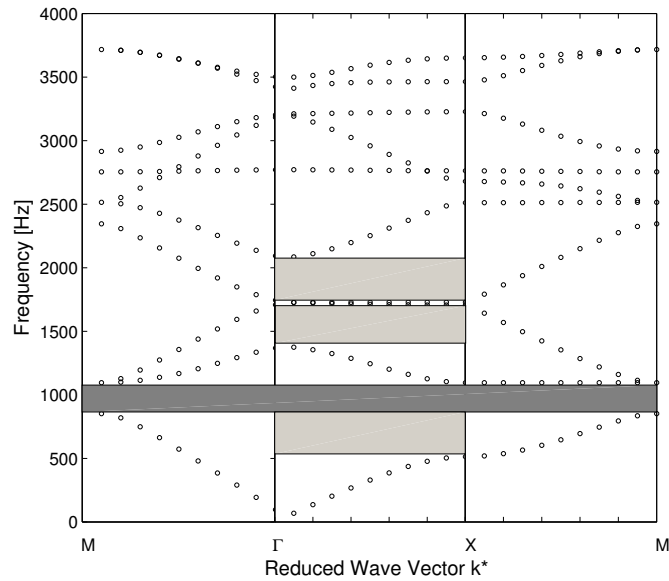


Figure 3.13: Dispersion curves for a square array with $L_c = 0.200$ m and $r = 0.080$ m evaluated using the PWE method.

ranging from 7 to 10 dB. At Bragg frequency, differences still emerge between the results of the measurements performed at positions 1, 2, 3. In reflection measurements, IL values computed for points 1 and 2 match significantly well up to 4,200 Hz (Fig. 3.12 c). For measurement positions 1, 2, 3 (Fig. 3.12 a, c), the behaviour in reflection is well-matched to that in insulation, as at Bragg frequency a positive IL value in insulation corresponds to a negative value in reflection as expected. Below Bragg frequency, there is a region in which the IL measured in position 1 shows positive values both in insulation and reflection, indicating an attenuation on both sides of the sample (Fig. 3.12 e).

Moving the measurement points away from the sample, i.e. for measurement position A, B, C (Fig. 3.12 b, d), no constructive interference is found at Bragg frequency in reflection as the dip of negative values is shifted backwards in frequency. For this set of points the behaviour in reflection seems more homogeneous among the points A, B, C (Fig. 3.12 d). In insulation, the same trend spot by measurements in 1, 2, 3 is found.

3.2.3 Array III

The third array under test has $L_c = 0.200$ m and $ff = 0.50$ and the relative dispersion curves are reported in Fig. 3.13. The first Bragg band gaps are expected at $f_{Bragg,\Gamma X} = 858$ Hz for normal incidence and at $f_{Bragg,\Gamma M} = 606$ Hz for an incidence angle of 45° . The band structures calculated with the PWE method spot a complete band gap in the range 850-1,100 Hz. In the ΓX direction, the width of the band gap is greater and goes down to 520 Hz. A second band gap is clearly visible on ΓX in the range 1,370-2,090 Hz.

The measured values of IL are presented in Fig. 3.14. As anticipated above, the measurements performed at a distance of 0.05 m from the cylinders were not analysed thus

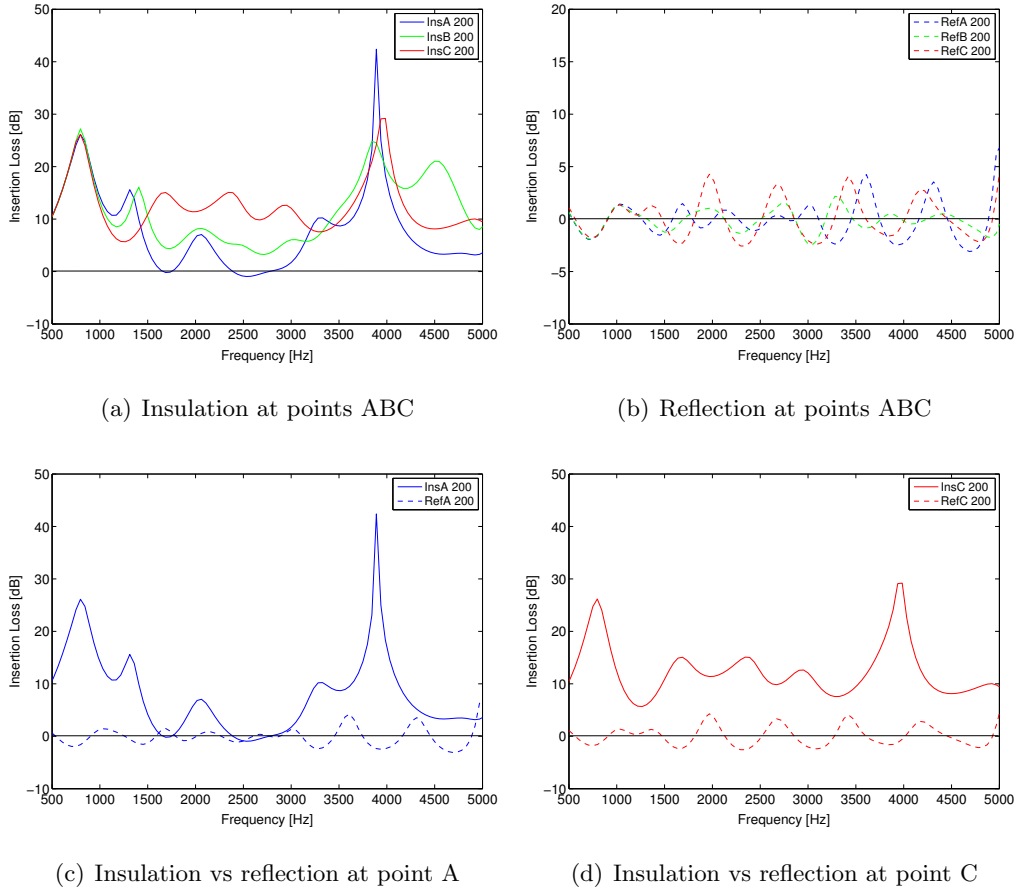
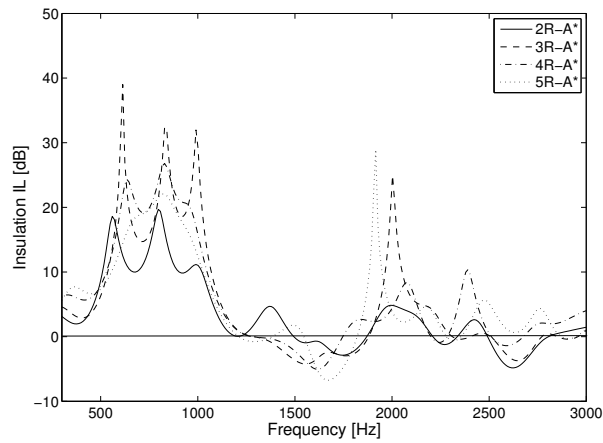


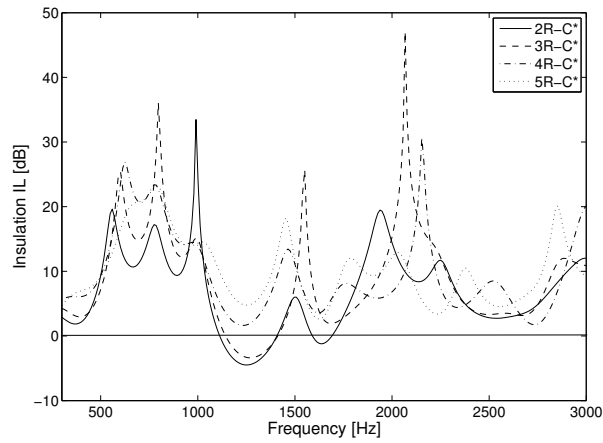
Figure 3.14: Insertion Loss measurements at positions A, B, C for insulation and reflection measurements. The IRs were processed using a Blackman-Harris time window.

only results relative to the measurement positions labelled A, B, C are presented. Insertion Loss in transmission displays values up to 25 dB at Bragg frequency (Fig 3.14 a). At higher frequencies, the behaviour of the sample depends significantly on the microphone position. Reflection measurements (Fig 3.14 b) do not provide relevant insight, just as the ones provided by the other two arrays at a distance of 1 lattice constant from the sample. As clearly visible in Fig. 3.14 (c, d), positive IL values in transmission correspond to (slightly) negative IL values in reflection.

Since array III has the same filling fraction of array II, it is possible to analyse differences and similarities between the measurements performed at a distance of 1 lattice constant and relate them to the results of array I, which has a different lattice geometry. At Bragg frequency, the magnitude of the attenuation for array III is about 25 dB and is almost constant between measurement positions A, B and C. This also occurred for array I where the attenuation was about 8 dB, while it does not happen for array II. Here, the sound insulation values vary between 10 and 25 dB at positions A, B and C without displaying any regular trend. For all arrays anyway the differences between the three measurement positions increase dramatically after the dip which separates the two crests



(a) Sound Insulation - Point A*

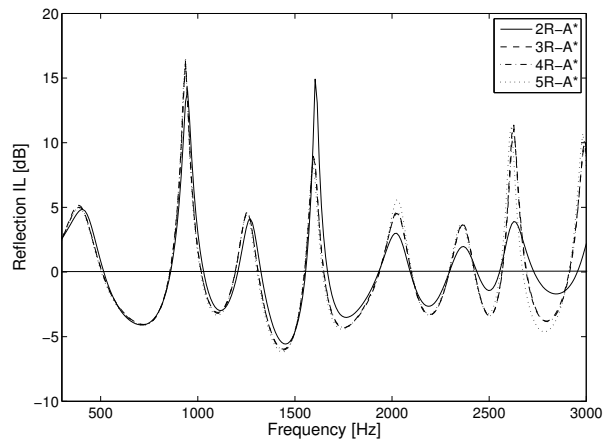


(b) Sound Insulation - Point C*

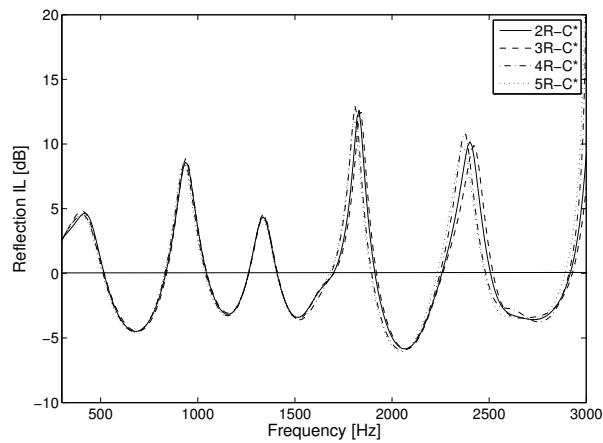
Figure 3.15: Sound insulation (dB) measured for array III with an increasing number of rows of cylinders at points A* (a) and C* (b). The IRs were processed with a modified Adrienne time window.

corresponding to the Bragg frequencies. At twice Bragg frequency in fact the impinging wavelength corresponds to the lattice constant. The IL measured in reflection follows a similar behaviour: attenuation found for arrays I and III ranges between +3 and -3 dB around Bragg frequency, while array II displays values ranging between +7 and -7 dB.

In order to investigate the effect of the addition of multiple layers of cylinders, sound insulation and reflection properties have been measured by varying the depth of the sample from 2 to 5 rows of cylinders. The IRs were windowed using an Adrienne time window, as reported in subsection 3.1.2. In each configuration, the relative distance between the sound source, the sample and the microphone was kept the same, and so was the time window applied to the IRs, whose length is determined upon the cancellation of ground reflection and diffraction. The IL measured in insulation is reported in Fig. 3.15 while the reflection IL is reported in Fig. 3.16. The points analysed are two per side, namely



(a) Sound Reflection - Point A*



(b) Sound reflection - Point C*

Figure 3.16: Sound reflection measured for array III with an increasing number of rows of cylinders at points A* (a) and C* (b). The IRs were processed with a modified Adrienne time window.

positions A and C, A facing the central cylinder and C facing an interstice between two adjacent cylinders. The points are labelled with an asterisk for being shifted with respect to their original positions.

The insulation properties of the sample are not strongly affected by the position of the microphone relative to the cylinders around the Bragg frequency, while at higher frequency distinctions arise between measurement positions A* and C*. In particular, the region of null or slightly negative IL values is wider in position A* and is shifted forward in frequency with respect to point C*. It is worth noting that the barrier with only two rows of cylinders already generates an appreciable mechanism of wave interference responsible for the band gaps nucleation. The reflection IL oscillates in frequency and shows not to be dependent on the position of the microphone. It reaches a local maximum at around 450 Hz, significantly below Bragg frequency, and nearly zero values at Bragg frequency.

3.2.4 Measurements vs FE and MST calculations

The experimental results for the three arrays are reported in Fig. 3.17 together with the IL values calculated with the MST of the FE method. Points Ins A and Ref A are chosen for this comparison, which have been measured for all arrays.

For array I (Fig. 3.17 a and b), MST predictions match well the experimental data, exceeding slightly in the estimation of the Insertion Loss but predicting properly the peaks and dips.

The match between measurements and MST predictions for array II (Fig. 3.17 c and d) is still good in reflection, where the peaks are properly individuated, while it is not satisfactory in insulation. Apart from the region of the first band gap, there are important shifts in frequency and magnitude. The match between MST predictions and measured insulation values is not brilliant. It should be noticed that MST takes into account edge diffraction, while in the experimental results this contribution is partially or totally windowed out. This effect is particularly clear for array II, which displays the smallest lattice constant and thus the biggest contribution of diffraction.

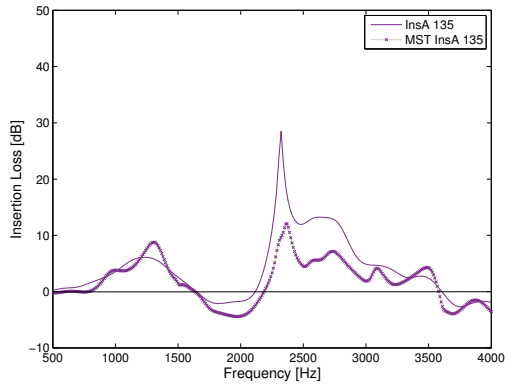
For array III, Fig. 3.17 (e and f) reports also the IL values calculated using the FE method using a point source, the domain being modelled with the constraints and boundaries reported in section 2.3.3 with a maximum mesh size of 0.006 m to get reliable results up to the frequency of interest. For sound insulation, the match between MST and FE calculation is almost total. Experimental measurements follow the trend in a satisfactory way except in the range 1,200 - 1,800 Hz, where the discrepancies between measurements and simulations are quite significant. In reflection, both methods fail to describe the sound pressure field. The FE method in particular shows a trend which is overturned with respect to the measured values.

3.3 The sound field inside sonic crystals

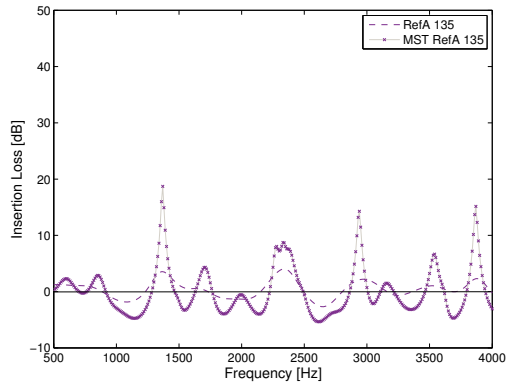
In order to verify the scattering process occurring inside sonic crystals, a set of measurements has been conducted by placing the microphone inside the sonic crystal and moving it along the transverse (SWT) and longitudinal (SWL) directions with a spacing of $1/4$ of the lattice constant. A sketch of the measurement positions considered for array I is displayed in Fig. 3.18. In the longitudinal direction, the measurement points extend beyond the sonic crystal in order to characterise the pressure field in this critical region. The stand that held the microphone was mounted on a sliding carriage which allowed to determine accurately the microphone positions.

3.3.1 Interpolation maps of the sound field

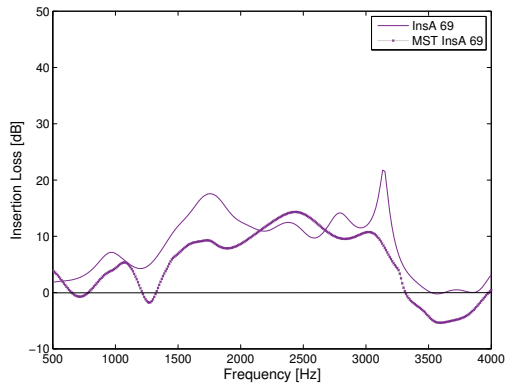
The results of the measurements inside the sonic crystals are reported on a 3D graph, having position and frequency on the x- and y-axis respectively and Insertion Loss on the z-axis. A cubic interpolation was made over the x-axis (position) in order to smooth the



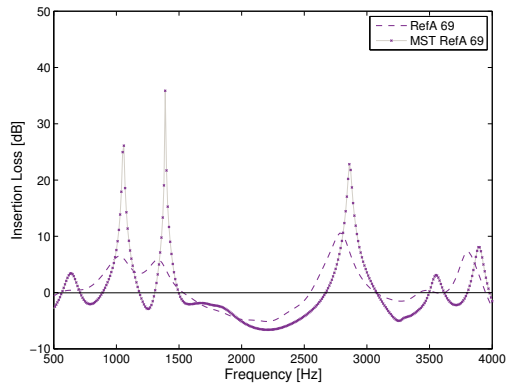
(a) Array I, INSA



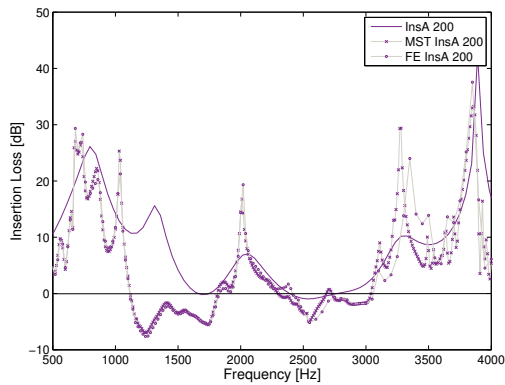
(b) Array I, REFA



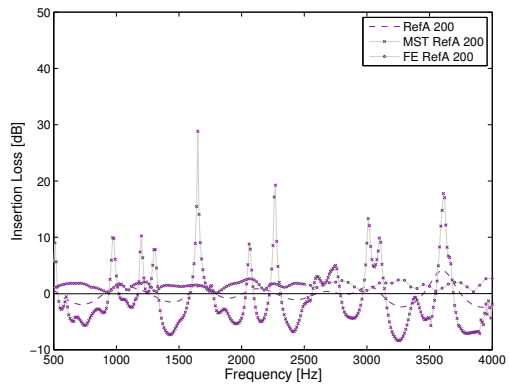
(c) Array II, INSA



(d) Array II, REFA



(e) Array III, INSA



(f) Array III, REFA

Figure 3.17: IL measurements vs FE and MST calculations at the points INSA and REFA in array I (a, b), array II (c, d) and array III (e, f).

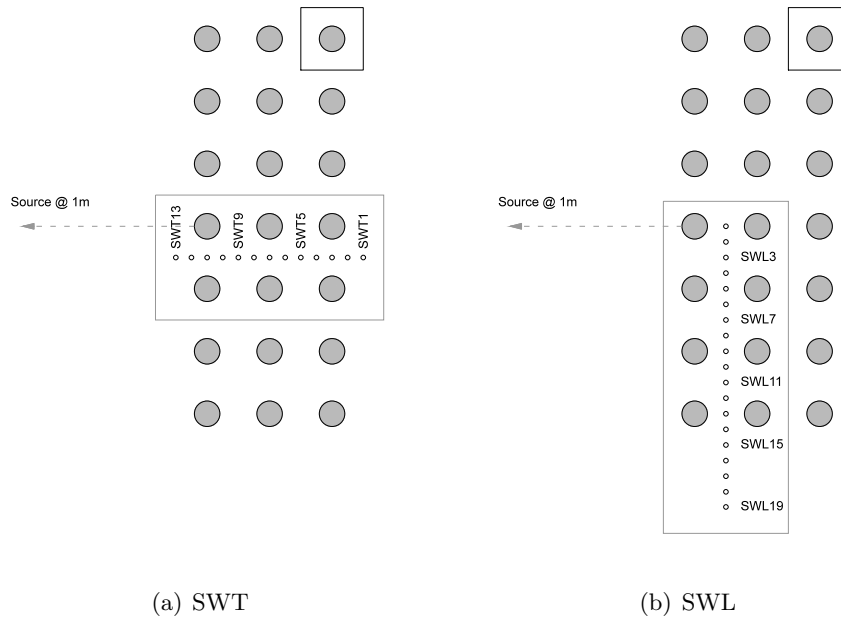
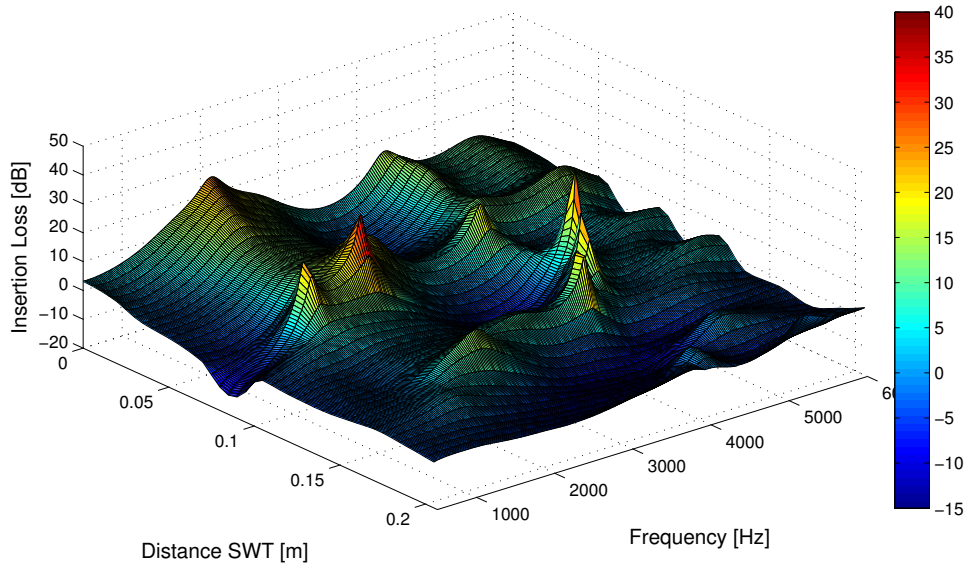


Figure 3.18: Measurement points inside the sonic crystal along the transverse (a) and longitudinal (b) directions. The distance between the points is $1/4$ of the lattice constant.

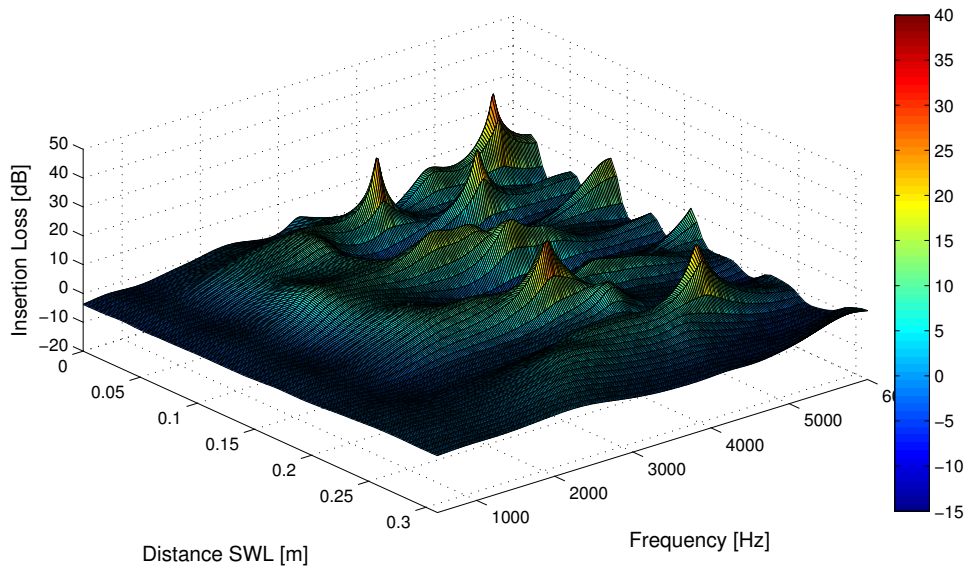
surface and render the data easy to read.

The IL measured inside array I is reported in Fig. 3.19, while Fig. 3.20 reports the IL calculated according to the Multiple Scattering Theory. For the sake of clarity, the measured data are reported in 2D in Fig. 3.21. In the transverse direction (Fig. 3.21 a), at Bragg frequency there is a general increase in IL which is particularly marked for the measurement positions located farther away from the closest cylinders. IL becomes more homogeneous with the distance moving away from the source, behaviour which is related to the exponential decay of the evanescent mode inside the band gap⁴⁶. After Bragg frequency, a region occurs in which the field is determined by constructive interference that repeats according to the Bloch-Floquet theorem with the periodicity of the crystal. In the longitudinal direction (Fig. 3.21 b) a similar pattern occurs. A first region with positive IL is found at 1,500 Hz, above the first Bragg frequency. Then the periodic pattern repeats up to 2,500 Hz, where a second particular region occurs. Outside the sonic crystal, the IL holds positive for a narrow region of space. The match between measurements and MST predictions is very good for measurements performed in the transverse direction, while in the longitudinal direction MST seems not to predict correctly the behaviour of the pressure field.

The measurements inside the sonic crystal performed on array II show a peculiar behaviour. Diagrams plotting the IL measured inside the crystal are reported in Fig. 3.22 in two-dimensions. For the transverse direction (Fig. 3.22 a), the 2D flattening shows

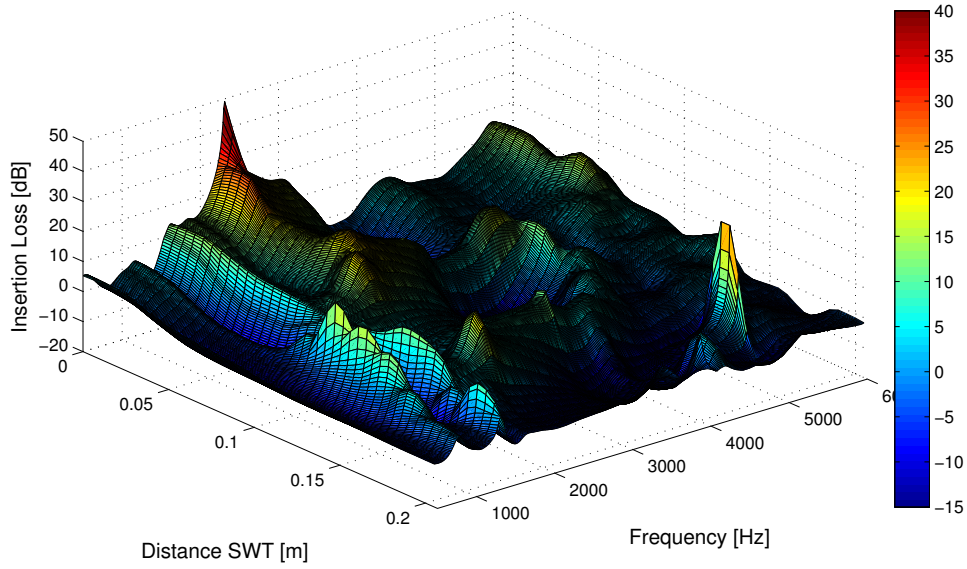


(a) Measurements SWT

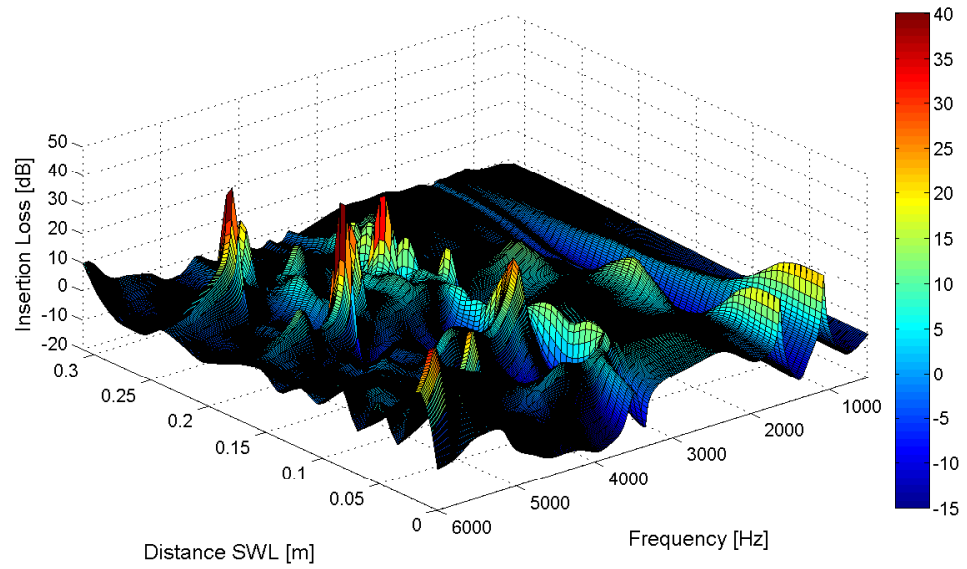


(b) Measurements SWL

Figure 3.19: Array I. Insertion Loss inside the sonic crystal: measurements in the transverse (a) and longitudinal (b) directions.

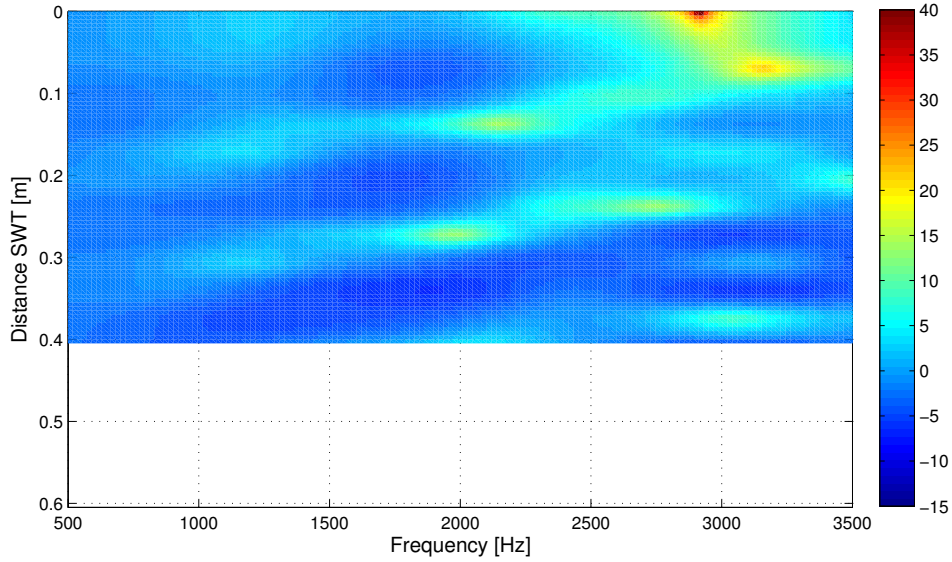


(a) MST predictions SWT

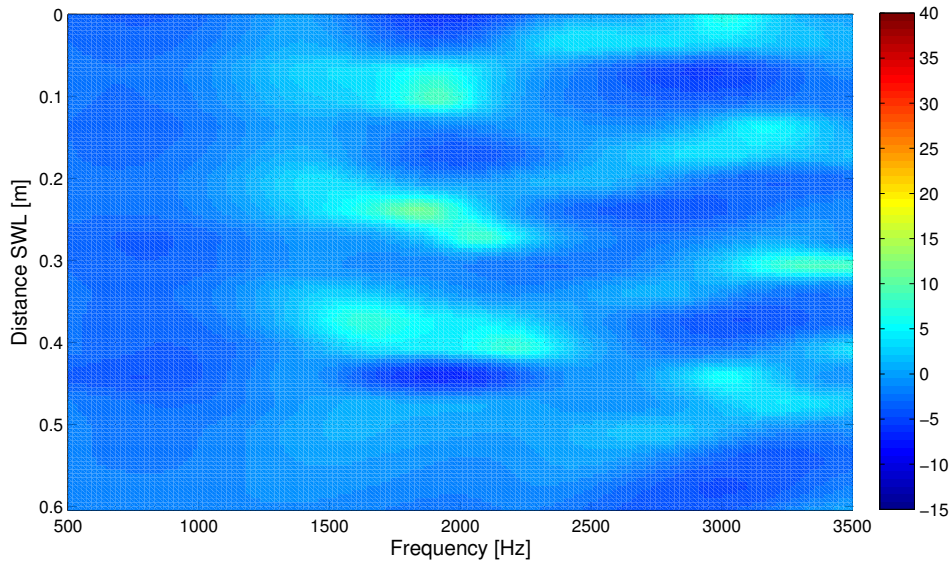


(b) MST predictions SWL

Figure 3.20: Array I. Insertion Loss inside the sonic crystal: MST predictions in the transverse (a) and longitudinal (b) directions.

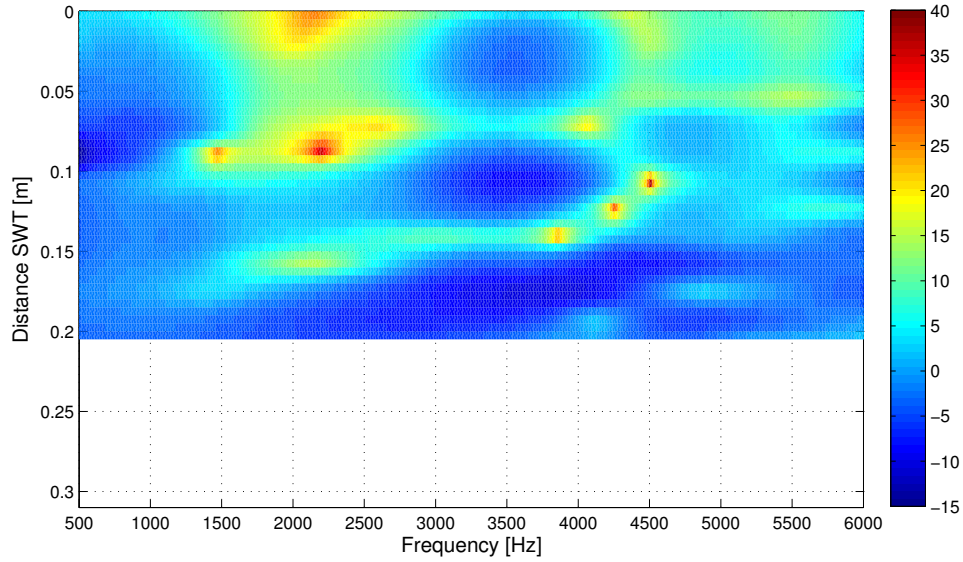


(a) IL (dB) in the transverse (SWT) direction. The source is located in the SW corner of the plot area.

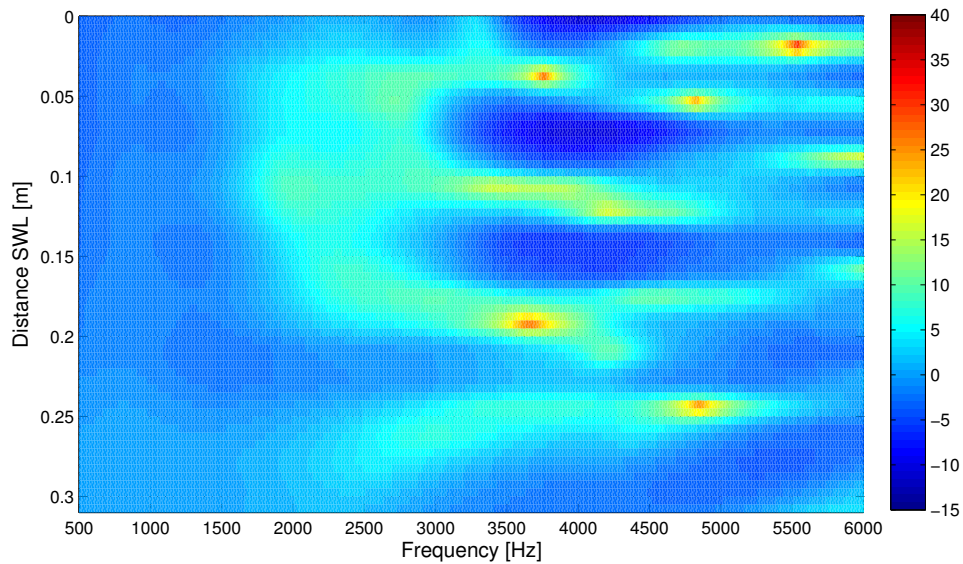


(b) IL (dB) in the longitudinal (SWL) direction. The source is located in the NW corner of the plot area.

Figure 3.21: Array I. Insertion Loss inside the sonic crystal in the transverse (a) and longitudinal (b) directions. Frequency on the x-axis, displacement inside the crystal on the y-axis.

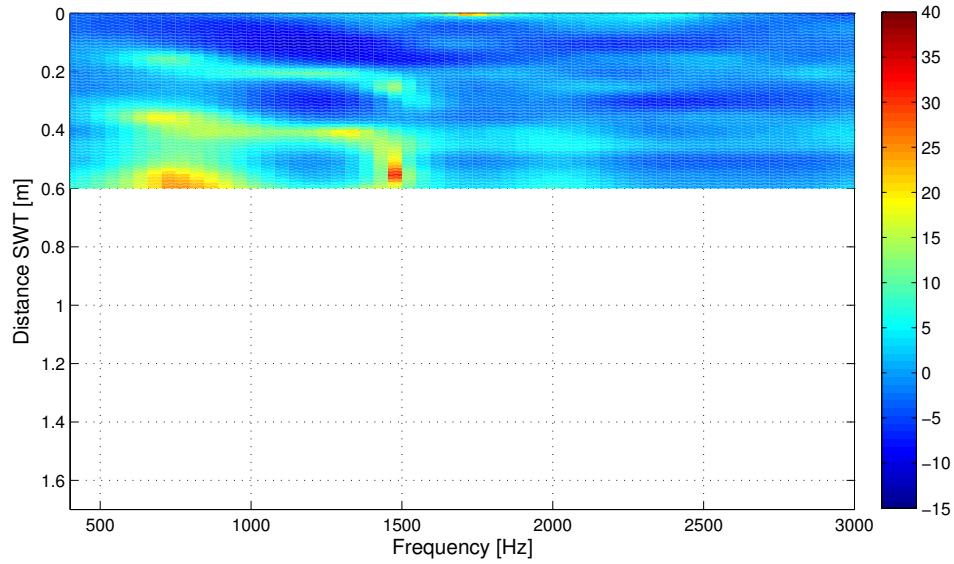


(a) IL (dB) in the transverse (SWT) direction. The source is located in the SW corner of the plot area.

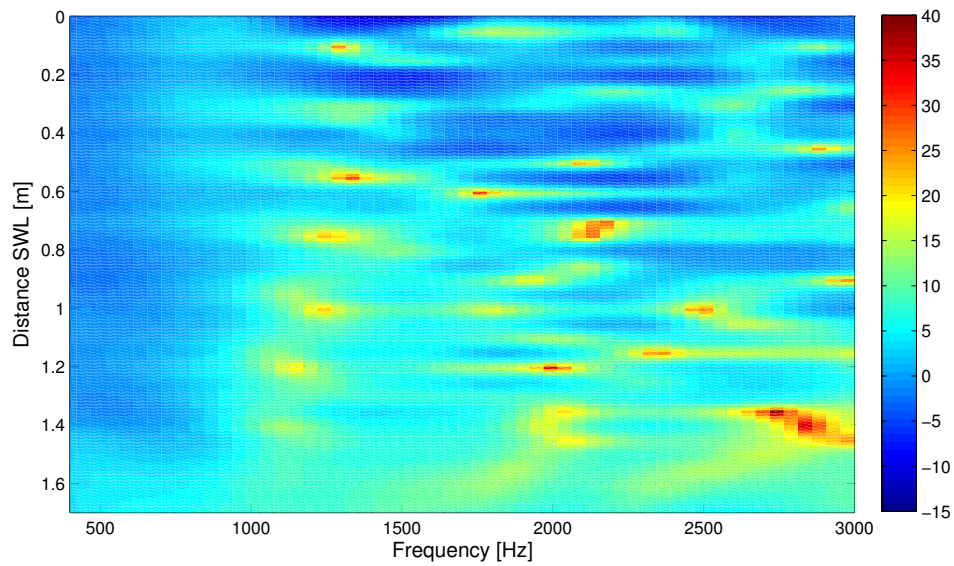


(b) IL (dB) in the longitudinal (SWL) direction. The source is located in the NW corner of the plot area.

Figure 3.22: Array II. Insertion Loss inside the sonic crystal in the transverse (a) and longitudinal (b) directions. Frequency on the x-axis, displacement inside the crystal on the y-axis.



(a) IL (dB) in the transverse (SWT) direction. The source is located in the NW corner of the plot area.



(b) IL (dB) in the longitudinal (SWL) direction. The source is located in the NW corner of the plot area.

Figure 3.23: Array III. Insertion Loss inside the sonic crystal in the transverse (a) and longitudinal (b) directions. Frequency on the x-axis, displacement inside the crystal on the y-axis.

two marked region corresponding to the first two Bragg band gaps in the ΓX direction, interrupted by a region in which a strong constructive interference occurs following the Bloch-Floquet theorem. Also in this case, the attenuation gradually increases moving farther away from the source. The longitudinal direction (Fig. 3.22 b) displays a similar pattern, showing a peculiar shift in frequency moving away from the source. In particular, the region of higher attenuation corresponds quite well to the range spot in the analysis over the transverse direction. In contrast, the dispersion curves calculated in section 3.2 (Fig. 3.11) indicate a band gap in the XM direction which extended over a smaller frequency range and that shared the same upper limit with the band gap in the ΓX direction.

Finally, Fig. 3.23 displays the 3D graphs of the measured IL inside the sonic crystal for array III. In the transverse direction (Fig. 3.23 a), the Bragg band gap in the ΓX direction is clearly detected around 800 Hz and at twice that frequency. As emerged from the results of array II, both the maxima and the minima of the IL increase moving away from the source. In the longitudinal direction (Fig. 3.23 b) the regions with positive IL shift to lower frequency as expected.

3.3.2 The evanescent modes

The IL measured inside the sonic crystals have been displayed above in a space-frequency-magnitude representation. The analysis of the 3D interpolation maps showed that an evanescent mode is clearly detectable in the transverse direction at Bragg frequency for arrays II and III, with a filling fraction of 0.50. In the longitudinal direction, an evanescent behaviour is also detected but shifted in frequency. Here, for these two arrays, the evanescent behaviour of modes inside the sonic crystals has been investigated.

The exponential decay inside the sonic crystal can be evaluated by means of an exponential fitting of the pressure *rms* values⁴⁶. Since to evaluate the exponential fitting it is necessary to perform a linear fitting of the pressure values, all inputs should be positive. Thus the exponential decay is calculated on *rms* values relative to measured IRs without subtracting the direct field. Considering the maxima of these trends, the exponential decay can be expressed as

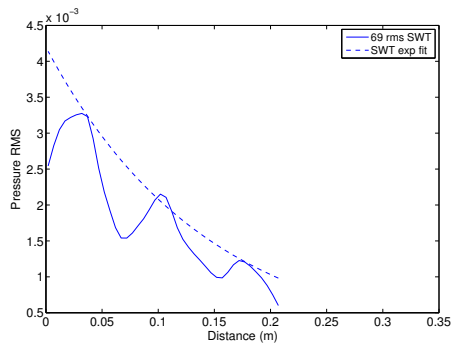
$$y = Ae^{Bx}$$

where $A = e^\beta$, being β the intercept of the linear regression calculated over the quantity $\ln(p_{rms})$ and $B = \alpha$, being α the angular coefficient of that linear regression. In particular, B indicates the imaginary part of the wave vector. The A and B coefficients of the two arrays are reported in Tab. 3.4.

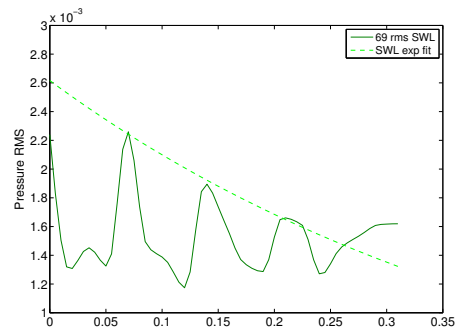
The exponential decays are then superimposed to the measured *rms* pressure values in Fig. 3.24. While the exponential decay is clearly detectable in the SWT direction (parallel to the incident wave vector), in the SWL direction (normal to the incident wave vector) it is less marked. In the measurements performed at the University of Bologna, the sample consisted of a greater number of cylinders, thus the shape of the decay is more

Table 3.4: Exponential functions fitting the *rms* pressure values measured inside two sonic crystals in the transverse (SWT) and longitudinal (SWL) directions.

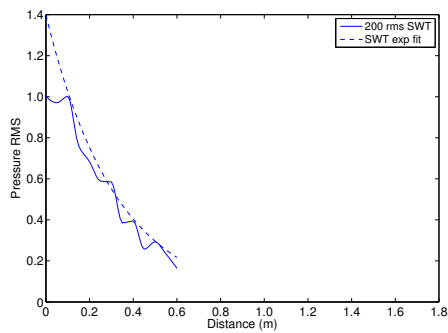
Array	Lc (m)	ff	Direction	Exponential fitting function
Array II	0.135	0.50	Transverse (SWT)	$y = e^{-5.47} \cdot e^{-7.02x}$
Array II	0.135	0.50	Longitudinal (SWL)	$y = e^{-5.95} \cdot e^{-2.20x}$
Array III	0.200	0.50	Transverse (SWT)	$y = e^{0.34} \cdot e^{-3.11x}$
Array III	0.200	0.50	Longitudinal (SWL)	$y = e^{-0.17} \cdot e^{-1.63x}$



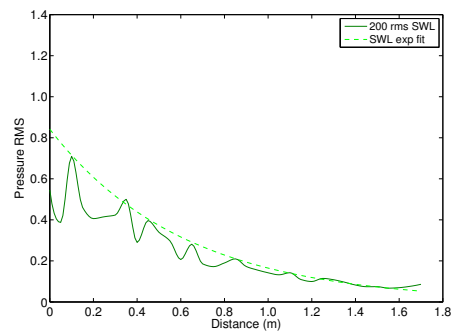
(a) Array II (OU) - SWT



(b) Array II (OU) - SWL



(c) Array III (BO) - SWT



(d) Array III (BO) - SWL

Figure 3.24: Exponential fitting over the *rms* pressure values measured inside the arrays II (a, b) and III (c, d) in the transverse (a, c) and longitudinal (b, d) directions. Both arrays have a filling fraction $ff = 0.50$; array II has $Lc = 0.069$ m while array III has $Lc = 0.200$ m.

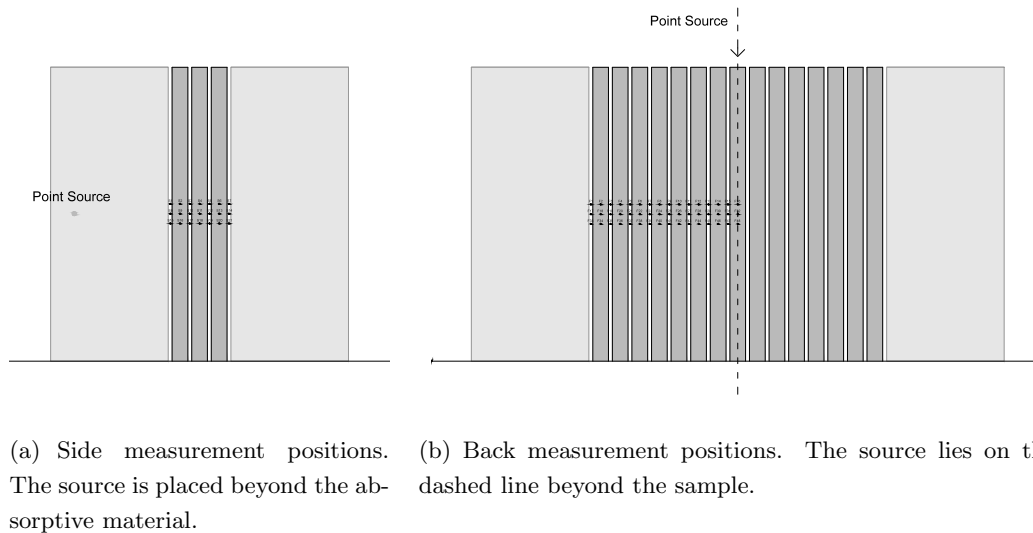


Figure 3.25: Measurement positions for sound intensity measurements at the University of Bologna. Side (a) and back (b) of the sample.

evident.

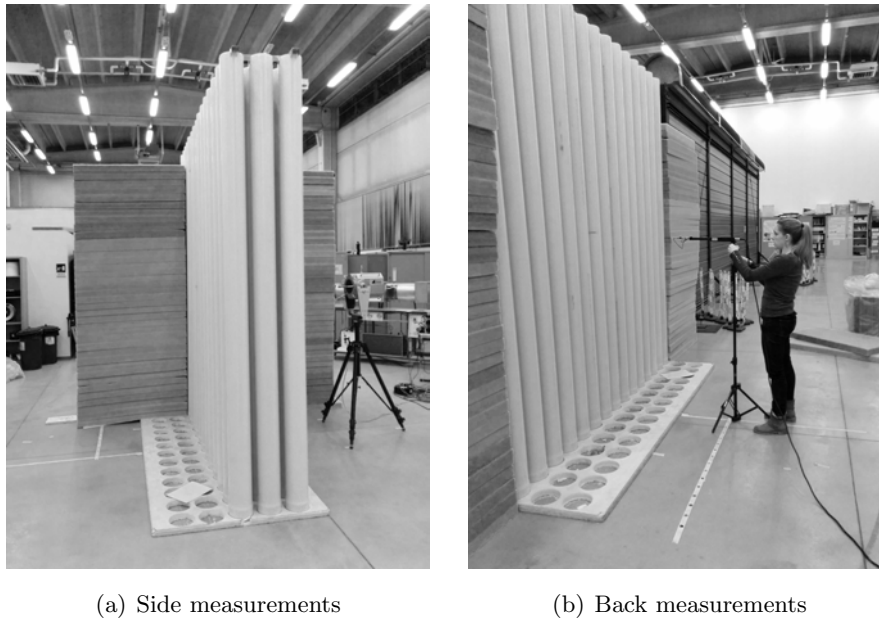
3.4 Sound intensity measurements

It is a topic long debated where there is any part of the sound field which travels in the longitudinal direction of sonic crystals. In order to evaluate the entity of sound emission from the sides of the sample, sound intensity measurements were conducted to investigate lateral and frontal transmission.

Measurements were conducted at the University of Bologna on a 15×3 square array of cylinders with $L_c = 0.200$ m and $ff = 0.50$ (array III). The measurement points are displayed in Fig. 3.25. The sound source was placed at a distance of 1 m from the sonic crystal and the intensity probe at a distance of 0.5 m. Two measurement positions were chosen per lattice constant, i.e. two consecutive measurement points are spaced apart by 0.10 m, and the probe was placed at three different heights: 1.4 m, 1.5 m and 1.6 m. In the following, only the measurements performed at a height of 1.5 m are presented. Fig. 3.26 shows the measurement setup. In order to minimise the effects of lateral diffraction and of the direct component, absorbing material was placed on the sides of the barrier.

The measurement chain consisted of the elements previously accounted for IR measurements plus:

- G.R.A.S. 50 AI-B Lemo 1/2" Intensity Probe;
- 01dB sound card;
- Ocenaudio software generating the pink noise.



(a) Side measurements

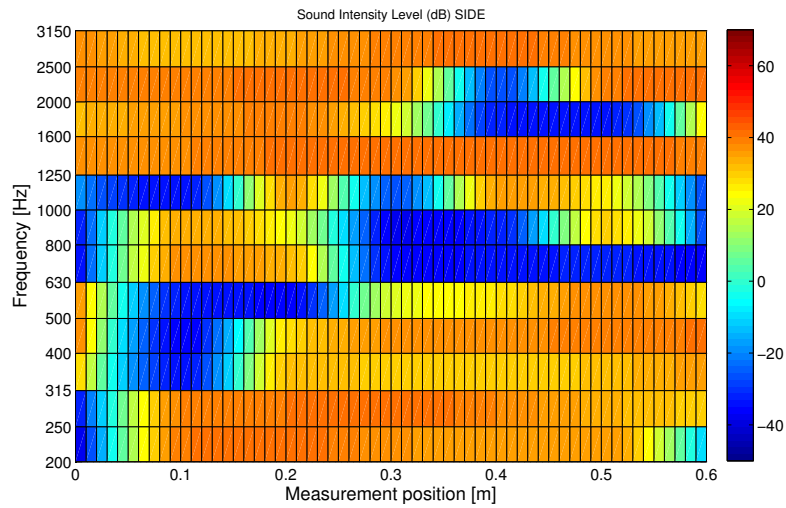
(b) Back measurements

Figure 3.26: Pictures of the sound intensity measurement setup - side (a) and back (b).

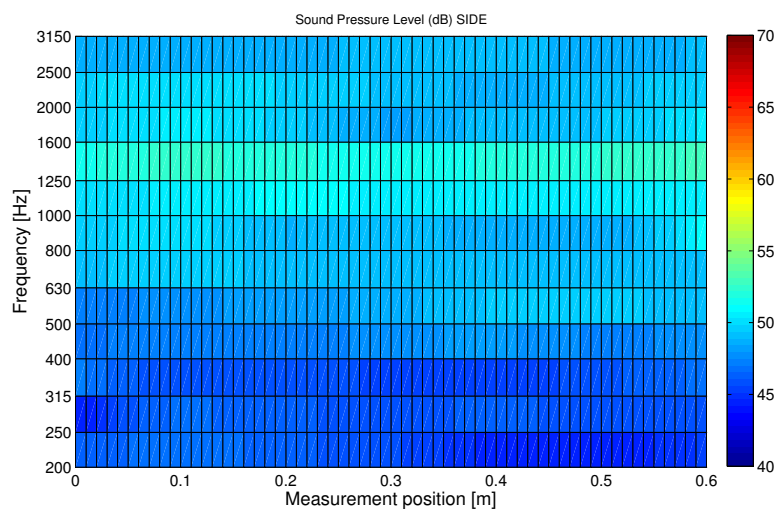
The results are reported as contour maps, where sound intensity and sound pressure levels are interpolated along the “back” and “side” displacement axes in one-third of octave bands ranging from 200 to 3,150 Hz (Fig. 3.28 and Fig. 3.27).

The sound intensity levels plotted in Fig. 3.27 (a) show areas with negative values around the first Bragg band gap. The appearance of negative values suggests that the field detected by the intensity probe is severely affected by the out-of-phase noise coming from the surrounding environment, being the front component negligible compared to that. Moving along the side of the sample, these darker regions are concentrated around 800 Hz, with no significant shift in frequency. The sound pressure level (Fig. 3.27 b) is homogeneous with the distance and shows a region of incremented values in the one-third of octave band of 1,250 Hz, region which also correspond to high sound intensity levels. This matches perfectly the pattern of the sound field inside the array displayed in Fig. 3.23 (b), providing an additional evidence of sound propagation in the longitudinal direction.

Measurements in the rear of the sample were made by shifting the intensity probe parallel to the sample. In this configuration, some regions are detected between the 315 and the 1,600 one-third octave bands which displays higher sound pressure levels compared to the surrounding areas (Fig. 3.28 b). A band of slightly lower sound intensity level is found between 800 and 1,000 Hz, at Bragg frequency. At twice Bragg frequency there is a sudden increase in sound pressure and intensity level at the measurement position closer to the sound source.

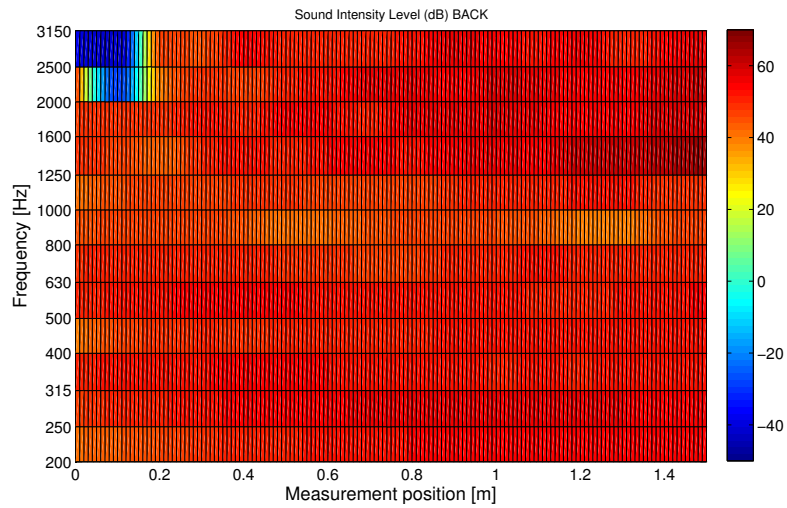


(a) Sound Intensity level (dB) - SIDE

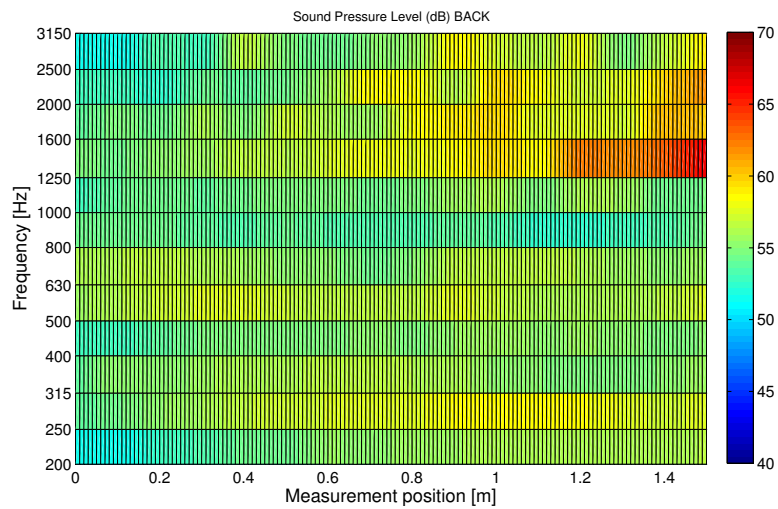


(b) Sound Pressure Level (dB) - SIDE

Figure 3.27: Sound intensity and sound pressure levels measured behind on one side of sample. The source is to the left of the plot areas.



(a) Sound Intensity level (dB) - BACK



(b) Sound Pressure Level (dB) - BACK

Figure 3.28: Sound intensity and sound pressure levels measured behind the sample. The source is to the right of the plot areas.

3.5 Standardised SI and RI measurements

The measurements conducted so far were aimed at pointing out the multiple scattering process and to enter the detail of the sound field distribution inside the sonic crystal. As pointed out in the literature review, after the first measurements conducted over the sculpture by Eusebio Sempere in Madrid²⁶, a flourishing literature has followed immediately, analysing the phenomenon with different lattice structures. Most of the measurements are carried out in anechoic chambers^{28;37;42} and on samples constrained in width; the resulting attenuation values thus comprise transmission and edge diffraction effects. In order to render negligible the contribution of the field diffracted from the edges, in many cases the microphone was placed very close to the sample⁴². Two significant exceptions to this measurement method are Refs.^{27;29} In Ref.²⁷ the IRs are windowed in order to minimise the reverberation effects, which were evident for the free-field measurements. A time window of 6 ms was used, but since the rods were 1 m long, diffraction effects were included. In Ref.²⁹ measurements were conducted on a 1.1 x 7.2 m sample. The width of the sample was kept large in order to minimise the edge diffraction and measurements were performed in open air.

The intrinsic acoustic characterisation of a noise barrier in itself as a product requires to assess the transmitted and reflected sound properties⁷⁰. In more recent years, Castineira-Ibàñez *et al.*⁴⁷ characterised ‘advanced’ sonic crystal barriers by acoustic standardisation tests performed according to EN 1793-2⁴⁸, i.e. under diffuse field conditions. In order to measure the effective sound insulation and reflection properties of the barrier for normal incidence, diffraction effects and all unwanted reflections should be cut off from the measurements. This is possible, even in a non-anechoic environment, using transient sound signals and a suitable windowing technique, which is currently standardised in EN 1793-6⁶⁷ and EN 1793-5⁶⁶. The main strength of using standardised indices is that they allow to do comparisons between different samples, and in particular to test the performance of sonic crystal noise barriers versus common noise barriers.

At the University of Bologna the Sound Insulation Index (SI) and the Reflection Index (RI) have been thus measured according to the EN 1793-5⁶⁶ and EN 1793-6⁶⁷ standards, which describe a method which allows to perform laboratory measurements returning results which do not differ significantly from in situ measurements⁷¹. The width and height of the sample determined the characteristics of a time window that was used to cancel ground reflection and edge diffraction, thus computing the transmitted sound component only.

The same cylinder arrangement used for the single point measurements (array III) has been used to test the acoustic properties of sonic crystal as noise barrier. The arrangement of the cylinder, repeated here for the sake of convenience, consisted in a $15 \times n$ square lattice of hollow PVC cylinders vertically standing, with a height of 3 m, $L_c = 0.200$ m and $ff = 0.50$. The depth of the barrier was varied by mounting 2 to 5 rows of cylinders.

The sound source is placed in front of the barrier at a height of 1.5 m, 1 m away from

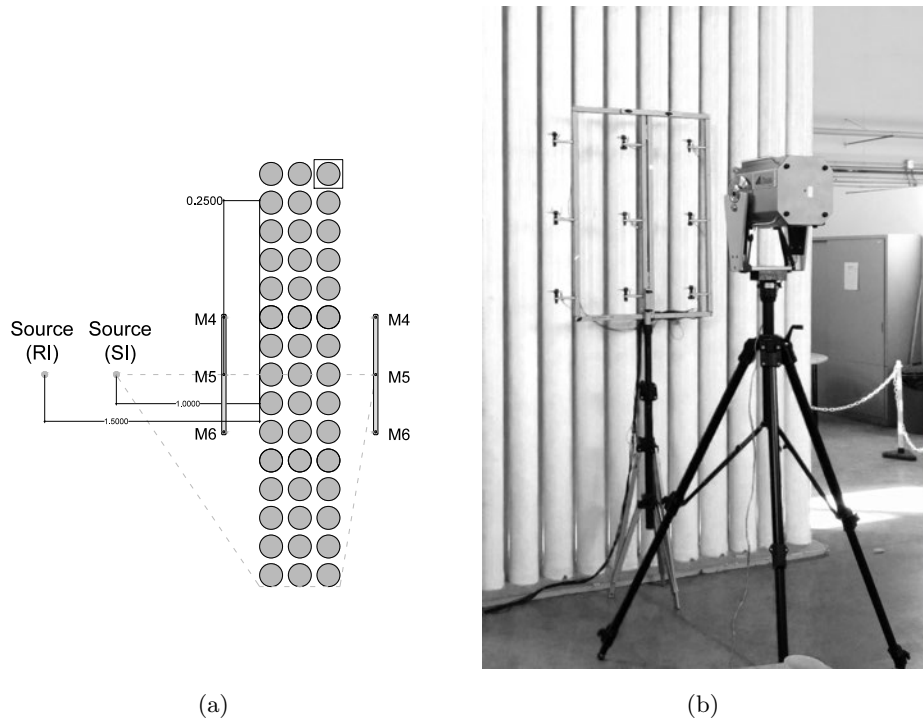


Figure 3.29: Measurement setup at the Acoustic Laboratory of the University of Bologna. Position of the source and the microphone array for the sound reflection and the sound insulation indices (a) and picture of the source and microphone array for reflection measurements (b).

the closest cylinders for sound insulation measurements and 1.5 m away for reflection measurements^{66;67}. The microphones are arranged in a 3x3 square array (M1-M9), spaced apart 0.40 m both in the horizontal and vertical directions. This array is positioned parallel to the sonic crystal at a distance of 0.25 m either on the side of the loudspeaker (reflection measurements) or on the opposite side (sound insulation measurements). The loudspeaker always faces the central microphone of the array, M5 (Fig. 3.29 a). Since the spacing between the microphones is a multiple of the lattice constant and given the periodicity of the sample, measurements were performed in two configurations; in configuration *a* the central microphone of the array faces the central cylinder, while in configuration *b* it faces the interstice between two adjacent cylinders.

The experimental apparatus consisted of:

- 16 channels Analog to Digital converter RME M-16 AD;
- RME Hammerfall HDSPe MADI for the A/D and D/A section;
- 9 Brüel & Kjær 4935 microphones;
- 16 channels Brüel & Kjær 2694 preamplifier;
- Samson Servo 201A power amplifier;
- ZIRCON loudspeaker.

IR measurements were performed using ESS test signals as previously discussed. Adri-

enne time windows functions are applied to the impulse responses; this permits to cancel unwanted reflections (ground reflection amongst all) as well as diffraction from the barrier top and side edges. The lengths of the different parts of the Adrienne time window have been set according to EN 1793-6⁶⁷, adapted to the dimensions of the sample and respecting the 7/3 ratio between the flat portion and the trailing edge. According to Fig. 13 reported in EN 1793-6⁶⁷, the lowest reliable frequency for a 3 m high barrier is about 260 Hz, hence the frequency range analysed is 400-5,000 Hz in 1/3 octave bands.

3.5.1 Sound Insulation Index

The sound insulation SI properties of the sample under test are evaluated according to EN 1793-6⁶⁷. The sound components transmitted through the barrier and the corresponding free-field reference measurement are post-processed to compute the SI index:

$$SI_j = -10 \log \left\{ \frac{1}{n} \sum_{k=1}^n \frac{\int |F[h_{t,k}(t)w_{t,k}(t)]|^2 df}{\int |F[h_{i,k}(t)w_{i,k}(t)]|^2 df} \right\} \quad (dB) \quad (3.2)$$

where $h_{i,k}(t)$ is the free-field impulse response at the k -th microphone position, $h_{t,k}(t)$ is the impulse response at the k -th microphone position with the barrier in between, $w_{i,k}(t)$ and $w_{t,k}(t)$ are the time windows (Adrienne temporal windows)⁶⁷ for the free-field and the transmitted components respectively at the k -th microphone position, F denotes the Fourier transform, j is the index of the j -th one-third octave frequency band, Δf_i is the width of the j -th one-third octave frequency band and $n = 9$ is the number of microphone positions.

Figure 3.30 reports the SI values measured in configurations *a* and *b*. A strong attenuation can be observed in the frequency range 500-1,100 Hz in both configurations *a* and *b*, i.e. with microphones facing the centre of the cylinders or the voids between cylinders. The highest SI is measured in configuration *b*. At twice Bragg frequency, the SI assumes values close to zero (setting *b*) or slightly negative (setting *a*). This implies the presence of a constructive interference mechanism which, given the fact that SI is averaged over 9 microphone positions, cannot be due to a single-point localised anomaly. Further data relative sound insulation measurements sonic crystals for different measurement positions are available in⁷³. The sound insulation increases with the number of rows of the sample, even though with 4 and 5 rows of cylinders the measure saturates. This may be due to the limited size of the time window; if on one hand it allows to cancel unwanted sound components, on the other hand when the depth of the sample increases, the useful signal is widened in time as n -th order reflections are shifted in time. Indeed, for this kind of measurements the width of the time window depends on the dimensions (width and height) of the sample. Up to 3 rows of cylinders, all the significant reflections up to the n -th order are included in the time window for all rows of cylinders; for deeper samples, the n -th order reflections coming from the farther cylinders are windowed out from the

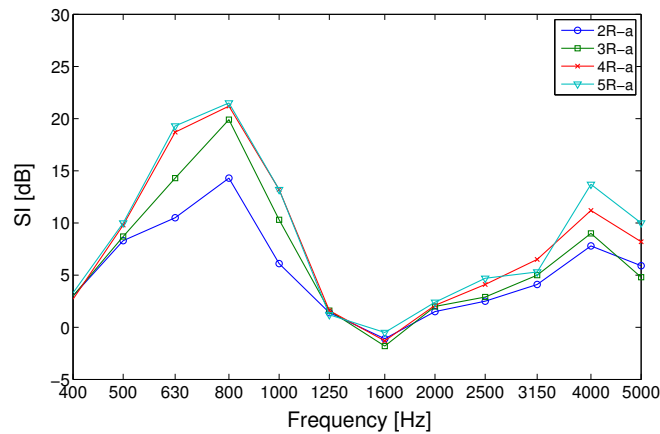
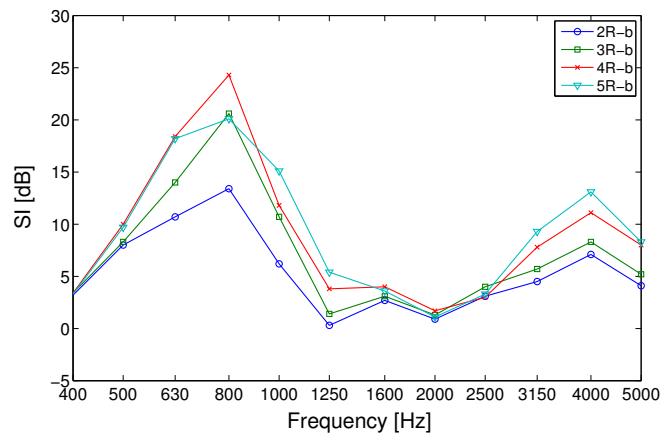
(a) SI - Setting *a*(b) SI - Setting *b*

Figure 3.30: Sound Insulation index measured in settings *a* (the array faces the centre of the cylinders) and *b* (the array faces the space between the cylinders).

impulse response and thus do not contribute to its spectral content. As a result, the SI value saturates returning misleading results.

The windowing procedure adopted according to the cited standards cancels the top diffraction effects, while many other most of the literature includes this contribution in the time window. A question arises: for this kind of periodic structures, can top diffraction be considered negligible? A further set of measurements was conducted on a sonic crystal by shifting the source and the receiver upwards and leaving the time window unchanged. This allowed to exclude ground reflections and side diffraction and to compute the effects of sound transmission and top diffraction combined. The Insertion Loss is presented in Fig. 3.31 in configurations *a* and *b*. A huge difference is found for top diffraction between the two configurations. When the microphone faces the cylinder (config. *a*), the shift of the microphone causes a drop in SI in the Bragg frequency and a peak around 2,000 Hz. A component emerges at 1,600 Hz, the region in which the SI displays negative values. Higher frequency SI values are less affected by the shift, except for the heights at which

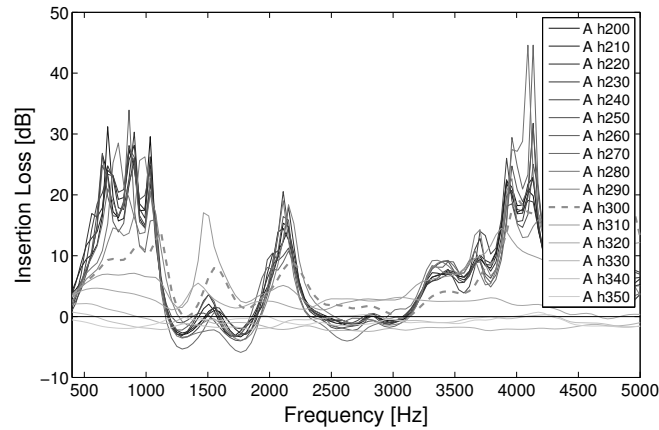
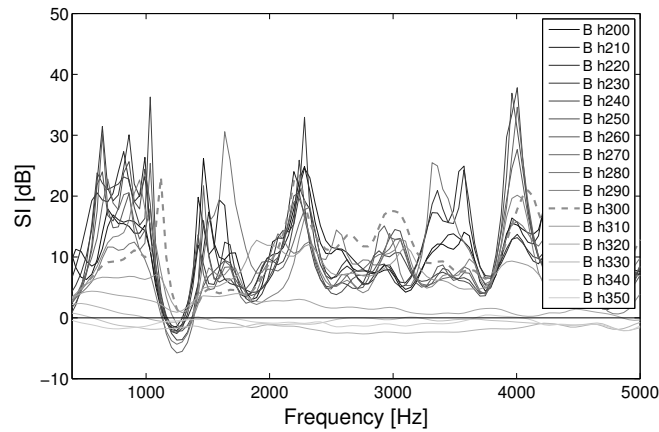
(a) config. *a*(b) config. *b*

Figure 3.31: Insertion Loss measured at different heights from the barrier. The insertion loss measured at a height of 3 m, i.e. the height of the barrier, is represented as a thicker dashed line.

the source and the microphone are sensitively higher than the barrier. In configuration *b* the drop around Bragg frequency occurs as well, and the dip at 1,250 Hz is identified univocally by all measurements, irrespective of the diffraction effect. The behaviour at higher frequency is also more homogeneous than in case *a*, except again for the last configurations.

3.5.2 Comparison with other noise barriers

The main strength of using standardised indices is that they allow comparisons between different samples. In particular, it is possible to test the performance of a sonic crystal noise barrier vs common noise barriers. Fig. 3.32 reports the SI values for lightweight and heavyweight noise barriers existing in the market together with the values calculated for sonic crystals. The barriers used for the comparison are taken from Ref.⁷⁴: a metallic non-flat barrier (MET sample no. 7), a timber barrier (TIM sample no. 9) and a concrete

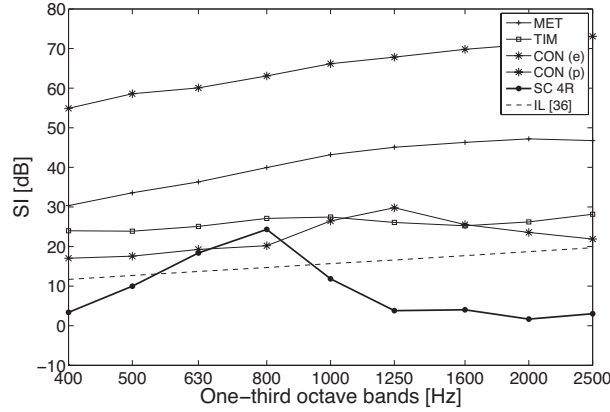


Figure 3.32: Comparison between the Sound Insulation index measured for a 4-rows sonic crystal (SC) and standard noise barriers, after⁷⁴: metallic non-flat barrier (MET), timber barrier (TIM), concrete barrier measuring across the acoustic elements (CON e) and across the posts (CON p). The dashed line (IL) is the insertion loss due to the top edge diffraction over a noise barrier calculated according to⁷⁵.

barrier (CON sample no. 13), measured across the acoustic element and across the posts. The timber barrier displays sound insulation values which are of the same order of magnitude of the maximum SI measured for a sonic crystal, while the metal and the concrete barriers show higher sound insulation values. For the concrete barrier, the SI values are measured both across the elements (solid line) and the posts (dashed line). For the latter case the SI value drops dramatically, suggesting that the actual sound insulation behind a real road barrier may be severely limited by the sound leakage at the panel-post junction. Fig. 3.32 also reports the theoretical Insertion Loss achievable for a given geometry of the barrier due to the top diffraction according to Ref.⁷⁵ Following the analytic expression proposed in this work, the Insertion Loss has been calculated considering a point source placed at a height of 1.5 m and at a distance of 3 m from the barrier, while the receiver is a point located at a height of 1.5 m (approximately a window at the ground floor) and at a distance of 10 m from the barrier. This theoretical value of Insertion Loss shows to be interesting for pointing out the effectiveness of sonic crystal noise barriers. The overall effect of any noise barrier is dominated by the sound diffracted over the top edge and the results show that in fact, all other kinds of barrier are oversized with respect to their insulation properties.

3.5.3 Sound Reflection Index

The Reflection Index (RI) is computed according to EN 1793-5⁶⁶ as follows:

$$RI_j = \frac{1}{n_j} \sum_{k=1}^{n_j} \left[\frac{\int_{\Delta f_j} |F[h_{r,k}(t) \cdot w_{r,k}(t)]|^2 df}{\int_{\Delta f_j} |F[h_{i,k}(t) \cdot w_{i,k}(t)]|^2 df} \cdot C_{geo,k} \cdot C_{dir,k}(\Delta f_j) \cdot C_{gain,k}(\Delta f_j) \right] \quad (3.3)$$

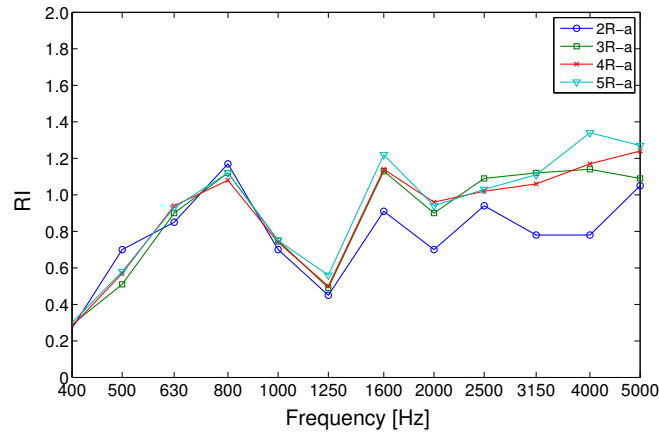
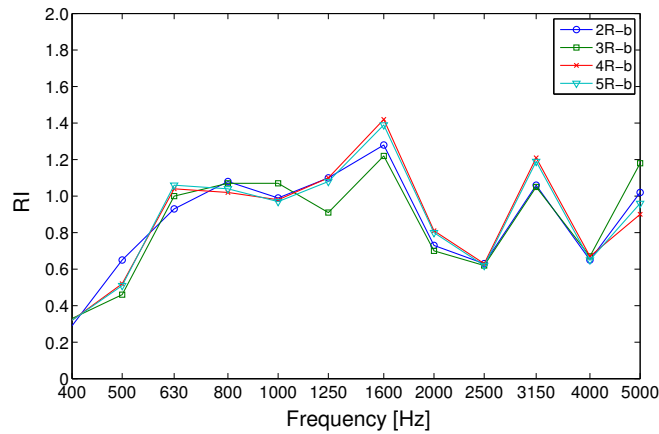
(a) RI - Setting *a*(b) RI - Setting *b*

Figure 3.33: Reflection index measured in settings *a* (the array faces the centre of the cylinders) and *b* (the array faces the space between the cylinders).

where $h_{i,k}(t)$ is the free-field impulse response at the k -th measurement point, $h_{r,k}(t)$ is the reflected component of the impulse response at the k -th measurement point, $w_{i,k}(t)$ and $w_{r,k}(t)$ are the time windows (Adrienne temporal windows) for the free-field and the reflected components respectively, F is the symbol of the Fourier transform, j is the index of the j -th one-third octave frequency band (between 100 and 5,000 Hz), Δf_j is the width of the j -th one-third octave frequency band, n is the number of microphone positions on which to average. With reference to the k -th measurement point, $C_{geo,k}$ is the correction factor for the geometrical divergence, $C_{dir,k}(\Delta f_j)$ is the correction factor for sound source directivity, $C_{gain,k}(\Delta f_g)$ is the correction factor relative to the loudspeaker amplification and the microphones sensitivity and Δf_g is the frequency range encompassing the one-third octave frequency bands between 500 and 2,000 Hz.

Figure 3.33 shows the RI measured in configurations *a* and *b*. There is a remarkable difference between these two configurations, especially concerning the general trend of RI in frequency. Configuration *a* displays a local maximum in the one-third of octave

band centred at 800 Hz, low values at 1,250 Hz and increases at higher frequencies. In configuration *b* the RI displays a regular trend in the Bragg frequency range, settling to 1.

While SI values do not change dramatically shifting between configurations *a* and *b*, RI measurements are strongly affected by the position of the microphone relative to the sample. While the impulse response in insulation is representative of a multiple scattering process, the impulse response measured in reflection is strongly affected by the first reflections. The energy related to the very first reflections determines significantly the spectral content of the signal, while subsequent reflections have smaller relative weight. This might explain both the dependence on the position and the independence from the number of rows. The spacing between the microphones is a multiple of the lattice constant, i.e. when the central microphone of the array faces the centre of a cylinder, all microphones face the centre of the cylinders, under different incidence angles: that might have amplified this effect.

The Reflection Index seems not to be closely dependent on the number of rows of the sonic crystal. Also this issue might be related to the windowing procedure. For the Reflection Index, the application of the time window is even more critical than in the calculation of SI; here the time window is centred on the arrival of the direct sound, thus multiple scattering components coming from the farthest cylinders might be easily windowed out.

Chapter 4

Concluding remarks

The work presented in this PhD thesis is concerned with the sound propagation through sonic crystals. Starting from the application of the Bloch-Floquet theorem to the wave equation, theoretical models have been implemented and analysed to investigate the characteristics of the sound field generated by sonic crystals. The Plane Wave Expansion method was used to calculate the band structures; the Multiple Scattering Theory was used to compute the scattered sound field at any arbitrary point and Finite Element analysis was used for both purposes, to derive band structures and to evaluate the pressure field inside the domain. The comparison of analytical and numerical tools showed that there is a good convergence between the methods and between band structures and attenuated sound field computed under different excitations. In particular, band structures extracted with the PWE and the FE methods showed a very good agreement. FE evaluations of the sound field for plane wave propagation and semi-infinite samples predicted stop bands at multiples of Bragg frequency, so as band structures did. At twice Bragg frequency, the FE calculations spotted an anomaly that is also displayed in the band structures, where a strong localised mode emerged displaying a nearly zero group velocity. For spherical wave propagation Bragg band gap is well identified, while at twice Bragg frequency no insulation properties were found, showing up only for normal incidence of plane waves. MST and FE predictions for plane wave propagation showed a good convergence in insulation, except for some oscillations of the MST values at Bragg frequency, while in reflection there seems to be a phase shift between the theoretical and numerical results.

An extensive set of experimental measurements has been carried out in order to investigate the mechanisms responsible for the generation of band gaps in sonic crystals. The experimental campaigns were hosted at the Acoustic Laboratory of the University of Bologna and in the anechoic chamber at the Open University headquarters in Milton Keynes (UK). Three unit cells were tested, consisting of hollow PVC cylinders immersed in air and arranged in a square lattice. The different setups, the different kinds of measurements and the different quantities searched provided coherent results for the three arrays and with the behaviour predicted by analytical and numerical tools. The results

showed that the sound field transmitted through the sample is attenuated at Bragg frequency by an amount related to the filling fraction of the array and to the number of rows of cylinders. After Bragg frequency, a region occurs where negative Insertion Loss is measured and predicted, probably because an interference phenomenon is triggered. The control of this phenomenon is central for the effective use of sonic crystals and will need further investigation. Sound intensity measurements outside the array proved to be coherent with the interpolation maps of the sound field inside the sonic crystal, showing that sound propagation is allowed in the longitudinal direction of the array in the frequency range where constructive interference occurs. The main achievements are briefly summarised in the following.

Sound insulation and reflection measurements have been carried out by placing the microphone at a fixed distance of one lattice constant from the sample and the relative IL was calculated. The measurements showed that at Bragg frequency the sound insulation is enhanced due to the stop-band properties of the sonic crystals, the attenuation covering a larger frequency spectrum for array II. Negative IL values were expected to occur in reflection as a consequence of Bragg scattering but did not, as around Bragg frequency the IL values tend to zero. The results confirmed that the arrays with higher filling fraction provide highest attenuation. The IL for arrays II and III, with a filling fraction of 0.50, reaches values up to 25 dB at Bragg frequency, vs the 8 dB of attenuation provided by array I, with filling fraction 0.13. While for arrays I and III the sound insulation is uniform amongst points close to each other, for array II the variability is high. This has been related to the contribution of side diffraction component included within the different time windows. At the University of Bologna, the width and height of the sample were the same, thus the cancellation of the ground reflection came together with the cancellation of side and top diffraction. At the Open University, the width of the sample for array II was sensitively smaller than the height. Since the length of the time window depends upon the cancellation of ground reflection, arrays with a smaller lattice constant include the diffracted sound field to a greater extent. This has been clearly pointed out comparing numerical predictions to measurements; in fact MST failed to describe accurately the behaviour of array II, though the truncation order was customised to provide reliable results. For all the three arrays, a region emerged after Bragg frequency which displayed null or slightly negative IL.

Further measurements were conducted on sonic crystals at the University of Bologna increasing the number of rows of cylinders. The results revealed the increase of IL in insulation and the occurrence of negative IL values (i.e. a constructive interference) behind the sample at twice Bragg frequency. This region of negative IL values displayed an important shift in frequency between the measurement position that faces the centre of a cylinder and the one that faces the interstice between two adjacent cylinders. IL measured in reflection did not display significant variation due to the increase in the number of cylinders.

The sound field inside the sonic crystals was analysed by moving the microphone inside

the array with a spacing of $1/4$ of the lattice constant along the two main symmetry directions of the lattice. The interpolation maps of the IL showed that the sound field distributes with the same periodicity of the array, according to the Bloch-Floquet theorem. In the direction parallel to the incident wave vector there is an increase in IL moving away from the source and after Bragg frequency, a region occurs where the field is dominated by constructive interference. The interpolation maps plotted in the direction normal to the incident wave vector also showed a region with diffusely increased IL values which are shifted upwards in frequency with respect to Bragg frequency. In arrays I and II these regions occupy a well-defined frequency range; for array III, as we move away from the source, the differences spot by the periodicity of the lattice are smoothed and the positive IL region shifts towards lower frequencies. This complies with the fact that the periodicity in the oblique direction is decreased and thus sound insulation occurs at lower frequencies. This might have been spot only for array III due to the greater number of cylinders of which it is made of. Again, this frequency region characterised by high IL values is followed in frequency by regions in which constructive interference rules. The sound pressure field inside the sonic crystal was proved to have an exponential decay within the lattice. Evanescent modes have been analysed by computing an exponential fitting of the *rms* pressure values inside the crystal and evaluating the imaginary part of the wave number which is responsible for the attenuation.

Measurements with an intensity probe were done to verify the existence of sound components travelling in the longitudinal direction of sonic crystals. In the transverse direction, sound intensity levels showed a band of slightly lower values centred at Bragg frequency, region corresponding also to low values of the sound pressure level. For points close to the source, i.e. for frontal transmission, at twice Bragg frequency there is a sudden increase in sound pressure and intensity level which reflects the constructive interference phenomenon which was spot from single-point measurements. Measurements on the sides of the sample showed more interesting results. At Bragg frequency, the formation of band gaps clearly emerged from the sound intensity measurements as after the second row of cylinders a negative value of sound intensity level is found. The appearance of negative values of sound intensity levels suggests that the field detected by the intensity probe is severely affected by the out-of-phase noise coming from the surrounding environment, being the front component negligible compared to that; in this case, no sound propagates in the longitudinal direction. There is a zone at around 1,250 Hz which displays high sound pressure levels and high intensity levels; this matches perfectly the pattern of the sound field inside the array displayed in the interpolation maps, providing an additional evidence of sound propagation in the longitudinal direction.

Finally, standardised Sound Insulation and Reflection Index measurements have been performed at the University of Bologna in order to characterise sonic crystals for normal incidence excluding any reflection or diffraction component. The SI values identified Bragg scattering clearly, locating accurately the stop-band as predicted from the band structure. The application of the time window on one side allows to neglect ground

reflection and edge diffraction; on the other hand it limits the possibility to investigate these structures when the number of rows increases. With the lattice constant of 0.2 m, this significance threshold was identified in 3 rows of cylinders; after this number, an increase in depth did not correspond to an increase in insulation. At twice Bragg frequency a null or negative SI settles that is related to a constructive interference which emerges from the measured data even if averaged over the 9 microphone positions. The Reflection Index showed to have a strong dependence on the position of the microphone relative to the sample; in fact its oscillating behaviour settles to regular trends only when averaged over several measurement positions. The reflection coefficients were found to be also quite independent from the number of rows of the crystal. This might be explained considering that in reflection measurements the direct sound is a key component in the spectral content of the impulse response, as well as the early reflections, and subsequent n -th order reflections play a minor role. The application of the time window for reflection impulse responses is also more critical, being the direct sound involved, as all useful multiple scattering components are shifted forward in time.

The standardised indices were used to compare the performance of sonic crystal to that of common noise barriers. Sonic crystals proved to reach a peak SI value comparable to lightweight timber barriers, even though only at Bragg frequency. Standard heavy barriers provide higher SI values with almost flat frequency response, although significant drops occur at the panel-post junction due to sound leakage. Anyway these high values are scarcely representative of the attenuation that is actually achievable as the overall effect of any noise barrier is dominated by the sound diffracted over the top edge. The results in fact showed that all other kinds of barrier are oversized with respect to their insulation properties. With a proper enhancement of the sound insulation properties of such crystals, these might turn out to be an interesting substitute for common noise barriers.

This work has explored the theoretical and experimental basis of the generation mechanisms of stop-bands in sonic crystals and provides a useful starting point for future developments on the topic. In the next future, measurements will be conducted on sonic crystals under diffuse field conditions. Moreover, the transmission properties of a small-scale sample will be tested in a modified impedance tube built according to ASTM E2611⁷⁶ in order to measure the reflected and transmitted sound field for normal incidence. This will start a new measurement campaign on small scale arrays to investigate stop-band properties emerging below the homogenisation limit, paving the way to the enlargement of the research to acoustic metamaterials.

References

- [1] C. Kittel, *Introduction to Solid State Physics* (Wiley, New York, 1968).
- [2] E. Yablonovitch, “Inhibited spontaneous emission in solid state physics and electronics”, *Phys. Rev. Lett.* **58** (20), 2059–2062, 1987.
- [3] J. D. Joannopoulos, S. G. Johnson, J. N. Winn and R. D. Meade, *Photonic Crystals. Molding the Flow of Light* (Princeton University Press, Princeton, 2008).
- [4] J. O. Vasseur, P. A. Deymier, A. Khelif, Ph. Lambin, B. Djafari-Rouhani, A. Akjouj, L. Dobrzynski, N. Fettouhi and J. Zemmouri, “Phononic crystal with low filling fraction and absolute acoustic band gap in the audible frequency range: A theoretical and experimental study”, *Phys. Rev. E* **65**, 056608, 2002.
- [5] M. S. Kushwaha, P. Halevi, G. Martínez, L. Dobrzynski and B. Djafari-Rouhani, “Theory of acoustic band structure of periodic elastic composites”, *Phys. Rev. B.* **49** (4), 2313–2322, 1994.
- [6] M. S. Kushwaha and B. Djafari-Rouhani, “Sonic stop-bands for periodic arrays of metallic rods: honeycomb structure”, *J. Sound Vib.* **218** (4), 697–709, 1998.
- [7] M. Kafesaki and E. N. Economou, “Multiple-scattering theory for three-dimensional periodic acoustic composites”, *Phys. Rev. B.* **60** (17), 11993–12001, 1999.
- [8] V. G. Veselago, “The electrodynamics of substances with simultaneously negative values of ϵ and μ ”, *Sov. Ohys. Usp.* **10**, 509–514, 1968.
- [9] J. B. Pendry, A. J. Holden, D. J. Robbins and W. J. Stewart, “Magnetism from conductors and enhanced nonlinear phenomena”, *IEEE Trans. Microwave Theory Tech.* **47** (11), 2075–2084, 1999.
- [10] D. R. Smith, W. J. Padilla, D. C. Vier, S. C. Nemat-Nasser and S. Schultz, “Composite Medium with Simultaneously Negative Permeability and Permittivity”, *Phys. Rev. Lett.* **84** (18), 4184–4187, 2000.
- [11] Z. Liu, X. Zhang, Y. Mao, Y. Y. Zhu, Z. Yang, C. T. Chan and P. Sheng, “Locally Resonant Sonic Materials”, *Science* **289**, 1734–1736, 2000.

- [12] Z. Yang, H. M. Dai, N. H. Chan, G. C. Ma and P. Sheng, “Acoustic metamaterial panels for sound attenuation in the 500–1000 Hz regime”, *Appl. Phys. Lett* **96**, 041906, 2010.
- [13] J. Mei, G. Ma, M. Yang, Z. Yang, W. Wen and P. Sheng, “Dark acoustic metamaterials as super absorbers for low-frequency sound”, *Nat. Comm.* **3**:756, 1–7, 2012.
- [14] N. Fang, D. Xi, J. Xu, M. Ambati, W. Srituravanich, C. Sun and X. Zhang, “Ultrasonic metamaterials with negative modulus”, *Nat. Mater.* **5** 452–456, 2006.
- [15] C. Ding, L. Hao and X. Zhao, “Two-dimensional acoustic metamaterial with negative modulus”, *J. Appl. Phys.* **108**, 074911, 2010.
- [16] Y. Ding, Z. Liu, C. Qiu and J. Shi, “Metamaterial with simultaneously negative bulk modulus and mass density”, *Phys. Rev. Lett.* **99**, 093904, 2007.
- [17] J. Li and C. T. Chan, “Double-negative acoustic metamaterial”, *Phys. Rev. E* **70**, 055602, 2004.
- [18] Y. Cheng, J. Y. Xu and X. J. Liu, “One-dimensional structured ultrasonic metamaterials with simultaneously negative dynamic density and modulus”, *Phys. Rev. B* **77**, 045134, 2008.
- [19] J. B. Pendry, D. Schurig and D. R. Smith, “Controlling Electromagnetic Fields”, *Science* **312**, 1780–1782, 2006.
- [20] D. Schurig, J. J. Mock, B. J. Justice, S. A. Cummer, J. B. Pendry, A. F. Starr and D. R. Smith, “Metamaterial Electromagnetic Cloak at Microwave Frequencies”, *Science* **314**, 977–979, 2006.
- [21] G. W. Milton, M. Briane and J. R. Willis, “On cloaking for elasticity and physical equations with a transformation invariant form”, *New J. Phys.* **8**, 248, 2006.
- [22] S. A. Cummer and D. Schurig, “One path to acoustic cloaking”, *New J. Phys.* **9**, 45, 2007.
- [23] H. Chen and C. T. Chan, “Acoustic cloaking in three dimensions using acoustic metamaterials”, *Appl. Phys. Lett.* **91**, 183518, 2007.
- [24] Y. Y. Chen and Z. Ye, “Theoretical analysis of acoustic stop bands in two-dimensional periodic scattering arrays”, *Phys. Rev. E* **64**, 036616, 2001.
- [25] V. Twersky, “Multiple Scattering of Radiation by an Arbitrary Configuration of Parallel Cylinders”, *J. Acoust. Soc. Am.* **24** (1), 42–46, 1950.
- [26] R. Martínez-Sala, J. Sancho, J. V. Sánchez, V. Gomez, J. Llinares and F. Meseguer, “Sound attenuation by sculpture”, *Nature* **378** (6554), 241, 1995.

- [27] W. M. Robertson and J. F. Rudy III, “Measurements of acoustic stop band in two-dimensional periodic scattering arrays”, *J. Acoust. Soc. Am.* **104** (2), 1998.
- [28] J. V. Sánchez-Pérez, D. Caballero, R. Martínez-Sala, C. Rubio, J. Sánchez-Dehesa, F. Meseguer, J. Linares and F. Gálvez, “Sound attenuation by a two-dimensional array of rigid cylinders”, *Phys. Rev. Lett.* **80**, 5325–5328, 1998.
- [29] J. V. Sánchez-Pérez, C. Rubio, R. Martínez-Sala, R. Sánchez-Grandia and V. Gomez, “Acoustic barriers based on periodic arrays of scatterers”, *Appl. Phys. Lett.* **81** (27), 5240–5242, 2002.
- [30] L. Sanchis, F. Cervera, J. Sánchez-Dehesa, J. V. Sánchez-Pérez, C. Rubio and R. Martínez-Sala, “Reflectance properties of two-dimensional sonic band-gap crystals”, *J. Acoust. Soc. Am.* **109** (6), 2598–2605, 2001.
- [31] L. Sanchis, A. Hakansson, F. Cervera, J. Sánchez-Dehesa, “Acoustic interferometers based on two-dimensional arrays of rigid cylinders in air”, *Phys. Rev. B* **67**, 035422, 2003.
- [32] H. Pichard, O. Richoux and J. P. Groby, “Experimental demonstrations in audible frequency range of band gap tunability and negative refraction in two-dimensional sonic crystal”, *J. Acoust. Soc. Am.* **132** (4), 2816–2822, 2012.
- [33] V. Romero-García, C. Lagarrigue, J.-P. Groby, O. Richoux and V. Tournat, “Tunable acoustic waveguides in periodic arrays made of rigid square-rod scatterers: theory and experimental realization”, *J. Phys. D: Appl. Phys.* **46** (30), 305108, 2013.
- [34] V. Romero-García, A. Krynkin, L. M. Garcia-Raffi, O. Umnova, and J. V. Sánchez-Pérez, “Multi-resonant scatterers in sonic crystals: Locally multi-resonant acoustic metamaterials”, *J. Sound Vib.* **332** (1), 184–198, 2013.
- [35] D. P. Elford, L. Chalmers, F. V. Kusmartsev and G. M. Swallowe, “Matryoshka locally resonant sonic crystal”, *J. Acoust. Soc. Am.* **130** (5), 2746–2755, 2011.
- [36] A. Krynkin, O. Umnova, A. Chong, S. Taherzadeh and K. Attenborough, “Scattering by coupled resonating elements in air”, *J. Phys. D: Appl. Phys.* **44**, 125501, 2011.
- [37] O. Umnova, K. Attenborough and C. M. Linton, “Effects of porous covering on sound attenuation by periodic arrays of cylinders”, *J. Acoust. Soc. Am.* **119** (1), 278–284, 2006.
- [38] J. Sánchez-Dehesa, V. M. García-Chocano, D. Torrent, F. Cervera, S. Cabrera and F. Simon, “Noise control by sonic crystals barriers made of recycled materials”, *J. Acoust. Soc. Am.* **129** (3), 1173–1183, 2011.
- [39] V. M. García-Chocano and J. Sánchez-Dehesa, “Optimum control of broadband noise by arrays of cylindrical units made of a recycled materials”, *Appl. Acoust.* **74**, 58–62, 2013.

- [40] A. Krynkin, O. Umnova, J. V. Sánchez-Pérez, A. Y. B. Chong, S. Taherzadeh and K. Attenborough, “Acoustic insertion loss due to two dimensional periodic arrays of circular cylinders parallel to a nearby surface”, *J. Acoust. Soc. Am.* **130** (6), 3736–3745, 2011.
- [41] R. Martínez-Sala, C. Rubio, L. M. García-Raffi, J. V. Sánchez-Pérez, E. A. Sánchez-Pérez and J. Llinares, “Control of noise by trees arranged like sonic crystals”, *J. Sound Vib.* **291**, 100–106, 2006.
- [42] C. Lagarrigue, J. P. Groby and V. Tournat, “Sustainable sonic crystal made of resonating bamboo rods”, *J. Acoust. Soc. Am.* **133** (1), 247–254, 2013.
- [43] M. M. Sigalas, “Defect states of acoustic waves in a two-dimensional lattice of solid cylinders”, *J. Appl. Phys.* **84** (6), 3026–3030, 1998.
- [44] L.Y. Wu and L. W. Chen, “Wave propagation in a 2D sonic crystal with a Helmholtz resonant defect”, *J. Phys. D: Appl. Phys.* **43**, 055401, 2010.
- [45] V. Romero-García, J. V. Sánchez-Pérez, L. M. García-Raffi, J. M. Herrero, S. García-Nieto and X. Blasco, “Hole distribution in phononic crystals: Design and optimization”, *J. Acoust. Soc. Am.* **125** (6), 3774–3783, 2009.
- [46] V. Romero-García, J. V. Sánchez-Pérez, S. Castiñeira-Ibáñez, L. M. Garcia-Raffi, “Evidences of evanescent Bloch waves in phononic crystals”, *Appl. Phys. Lett.* **96**, 124102, 2010.
- [47] S. Castiñeira-Ibáñez, C Rubio, V. Romero-García, J. V. Sánchez-Pérez, and L. M. García-Raffi, “Design, manufacture and characterization of an acoustic barrier made of multi-phenomena cylindrical scatterers arranged in a fractal-based geometry”, *Archives of Acoustics* **37** (4), 455–462, 2012.
- [48] EN 1793-2. Road traffic noise reducing devices - Test method for determining the acoustic performance - Part 2: Intrinsic characteristics of airborne sound insulation under diffuse sound field conditions, CEN, Brussels, 2012.
- [49] J. M. Ziman, *Principles of the theory of solids* (Cambridge University Press, Cambridge, 1964).
- [50] J. Mei, Z. Liu, J. Shi and D. Tian, “Theory for elastic wave scattering by a two-dimensional periodical array of cylinders: An ideal approach for band-structure calculations”, *Phys. Rev. B.* **67**, 245107, 2003.
- [51] T. Miyashita, “Sonic crystals and sonic wave-guides”, *Meas. Sci. Technol.* **16** R47–R63, 2005.
- [52] Y. Cao, Z. Hou and Y. Liu, “Convergence problem of plane-wave expansion method for phononic crystals”, *Phys. Lett. A* **327**, 247–253, 2004.

- [53] V. Laude, Y. Achaoui, S. Benchabane, and A. Khelif, “Evanescent bloch waves and the complex band structure of phononic crystals”, *Phys. Rev. B*, **80**, 092301, 2009.
- [54] D. Elford, *Band gap formation in acoustically resonant phononic crystals*. PhD thesis discussed at the Dept. of Physics of the Loughborough University, UK, November 2010.
- [55] P. A. Martin, *Multiple scattering. Interaction of Time-Harmonic Waves with N obstacles* (Cambridge University Press, Cambridge, 2006).
- [56] C. M. Linton and D. V. Evans, “The interaction of waves with arrays of vertical circular cylinders”, *J. Fluid Mech.* **215**, 549–569, 1990.
- [57] I. S. Gradshteyn, and I. M. Ryzhik, *Table of integrals, series and products* (Academic Press, San Diego, 2000).
- [58] J. Korringa, “Early history of multiple scattering theory for ordered systems”, *Physics Reports* **238** 341–360, 1994.
- [59] F. Ihlenburg, *Finite element Analysis of Acoustic Scattering* (Springer-Verlag, New York, 1998).
- [60] S. Falletta and G. Monegato, “An exact NRBC for 2D wave equation problems in unbounded domains, Porto Institutional Repository, 2013.
- [61] J. Berenger, “A perfectly matched layer for the absorption of electromagnetic waves”, *J. Comput. Physics* **114**, 185–200, 1994.
- [62] F. Collino and P. Monk, “The Perfectly Matched Layer in Curvilinear Coordinates”, *SIAM J. Sci. Computing*, **19**, 2061–2090, 1998.
- [63] M. Miniaci, *Behaviour and applications of elastic waves in structures and metamaterials*. PhD thesis discussed at the Dept. of Civil, Chemical, Environmental and Materials Engineering of the University of Bologna, Italy, May 2014.
- [64] M. Miniaci, A. Marzani, N. Testoni and L. De Marchi, “Complete band gaps in a polyvinyl chloride (PVC) phononic plate with cross-like holes: numerical design and experimental verification”, *Ultrasonics* **56**, 251–259, 2015.
- [65] Y. Pennec, J. O. Vasseur, B. Djafari-Rouhani, L. Dobrzyński and P. A. Deymier, “Two-dimensional phononic crystals: Examples and applications”, *Surf. Sci. Rep.* **65** (8), 229–291, 2010.
- [66] EN 1793-5:2014. Road traffic noise reducing devices - Test method for determining the acoustic performance - Part 5: Intrinsic characteristics - In situ values of sound reflection under direct sound field conditions, CEN, Brussels, 2014.

- [67] EN 1793-6:2012. Road traffic noise reducing devices - Test method for determining the acoustic performance - Part 6: Intrinsic characteristics - In situ values of airborne sound insulation under direct sound field conditions, CEN, Brussels, 2012.
- [68] T. D. Rossing (Ed.), *The Springer Handbook of Acoustics* (Springer, New York, 2007).
- [69] U. Sandberg, “The multi-coincidence peak around 1000 Hz in tyre/road noise spectra”, Proc. of 5th European Conference on Noise Control, 2003.
- [70] EN 14388:2015. Road traffic noise reducing devices - Specifications. CEN, Brussels, 2015.
- [71] M. Garai and P. Guidorzi, “European methodology for testing the airborne sound insulation characteristics of noise barriers in situ: Experimental verification and comparison with laboratory data”, *J. Acoust. Soc. Am.* **108** (3), 1054–1067, 2000.
- [72] M. Garai and P. Guidorzi, “Sound reflection measurements on noise barriers in critical conditions”, *Building and Environment* **94** (2), 752–763, 2015.
- [73] F. Morandi, P. Guidorzi, M. Miniaci, A. Marzani and M. Garai, “Acoustic measurements on sonic crystal barriers”, *Energy Procedia* **78**, 134–139, 2015.
- [74] M. Garai, E. Schoen, G. Behler, B. Bragado, M. Chudalla, M. Conter, J. Defrance, P. Demizieux, C. Glorieux and P. Guidorzi, “Repeatability and reproducibility of measurements of sound reflection and airborne sound insulation index of noise barriers”, *Acta Acustica united with Acustica* **100** (6), 1186–1201, 2014.
- [75] U. J. Kurze and G. S. Anderson, “Sound attenuation by barriers”, *Appl. Acoust.* **4**, 35–53, 1971.
- [76] ASTM Standard E2611, 2009, “Standard Test Method for Measurement of Normal Incidence Sound Transmission of Acoustical Materials Based on the Transfer Matrix Method”, ASTM International, West Conshohocken, PA, 2003.

Appendix A

Publications

A.1 Journal papers

F. Morandi, M. Miniaci, A. Marzani and M. Garai, “Sound insulation properties of a 2-D sonic crystal barrier: numerical design and experimental measurements”, **submitted to Applied Acoustics*.

F. Morandi, P. Guidorzi, M. Miniaci, A. Marzani and M. Garai, “Acoustic measurements on sonic crystal barriers”, *Energy Procedia* **78**, 134–139, November 2015.

S. De Cesaris, D. D’Orazio, F. Morandi and M. Garai, “Extraction of the envelope from impulse responses using pre-processed energy detection for early decay estimation”, *J. Acoust. Soc. Am.* **138** (4), 2513–2523, October 2015.

M. Garai, F. Morandi, D. D’Orazio, S. De Cesaris and L. Loreti, “Acoustic measurements in eleven Italian opera houses: correlations between room criteria and considerations on the local evolution of a typology”, *Building and Environment* **94P2**, 900–912, 2015.

A.2 International Conference papers

L. Barbaresi, F. Morandi, M. Garai and A. Speranza, “Experimental measurements of flanking transmission in CLT structures”, *Proc. of ICA 2016*, Buenos Aires, September 2016.

M. Garai, S. De Cesaris, D. D’Orazio, F. Morandi, “Sound energy distribution in Italian historical theatres”, *Proc. of ICA 2016*, Buenos Aires, September 2016.

A. Speranza, L. Barbaresi and F. Morandi, “Experimental analysis of flanking transmission of different connection systems for CLT panels”, *Proc. of WCTE 2016*, Vienna,

August 2016.

M. Garai, D. D’Orazio, S. De Cesaris and F. Morandi, “An attempt to rank Italian historical opera houses; considerations about measurement in eleven theatres”, Proc. of ISTD-07, Tokyo, November 2015.

F. Morandi, S. De Cesaris, D. D’Orazio and M. Garai, “Energy criteria in Italian historical opera houses: a survey over 11 theatres”, Proc. Auditorium Acoustics, Paris, October 2015.

M. Garai, P. Guidorzi and F. Morandi, “Sound reflection and sound insulation measurement on a sonic crystal noise barrier according to the new European methodology”, Proc. of Internoise15, San Francisco, August 2015 (invited paper).

M. Garai, D. D’Orazio, S. De Cesaris, F. Morandi and K. Ito, “The acoustics of Bayreuth Festspielhaus”, Proc. of ICSV22, Firenze, July 2015.

S. De Cesaris, F. Morandi, L. Loreti, D. D’Orazio and M. Garai. “Notes about the early to late transition in Italian theatres”, Proc. of ICSV22, Florence, July 2015.

F. Morandi, P. Guidorzi, M. Miniaci, A. Marzani and M. Garai, “Acoustic measurements on sonic crystal barriers”, Proc. of 6th IBPC, Turin, June 2015. * *best paper award*

F. Morandi, S. De Cesaris, M. Miniaci, A. Marzani and M. Garai, “Experimental evidence of band gaps in periodic structures”, Proc. of Euronoise 2015, Maastricht, June 2015 (invited paper).

F. Morandi, D. D’Orazio, S. De Cesaris, L. Barbaresi and M. Garai, “Sound radiation from stages in the theatres of Cesenatico and Longiano”, Proc. of AIA-DAGA International Conference, Meran, March 2013.

A.3 National Conference papers

F. Morandi, S. De Cesaris, D. D’Orazio, P. Guidorzi and L. Barbaresi, “Caratterizzazione sperimentale della trasmissione laterale di diversi sistemi di connessione per pannelli in CLT.” Proc. of AIA National Conference, Alghero, May 2016.

L. Barbaresi, F. Morandi and A. Speranza, “La misura della trasmissione laterale nelle strutture in legno: problematiche e metodologie a confronto.” Proc. of AIA National Conference, Alghero, May 2016.

S. De Cesaris, F. Morandi and L. Loreti, “Architettura e acustica del cinema Jolly di Vinicio Vecchi in Bologna”, Proc. of AIA National Conference, Pisa, June 2014.

F. Morandi, V. Sartini, D. D’Orazio, S. De Cesaris and M. Garai, “Confronto fra descrittori acustici delle sale misurati e simulati: il caso del Teatro Comunale di Cervia”, Proc. of AIA National Conference, Rome, July 2012.